The University Of Sheffield.

Department of Electronic and Electrical Engineering

Thesis submitted to obtain the Degree of Doctor of Philosophy

Influence of the p-type layer on the performance and stability of thin film silicon solar cells

Asiel Neftalí Corpus Mendoza

March 2017

Supervisor: Prof. M. M. De Souza

Abstract

The poor lateral conductance of amorphous silicon necessitates the use of a contact covering the entire surface of thin film silicon solar cells to minimise the resistance. This contact must be highly conductive, as well as transparent to allow absorption of light in the inner layers. In recent years this has paved way for transparent conducting oxides (TCOs) to be used in solar technology. However, the absence of a p-type TCO complicates the fabrication of an Ohmic contact to a-Si:H(p). Moreover, the difference in bandgap between the two materials results in a Schottky interface which has not been investigated comprehensively in terms of on-state/optical performance and stability before.

This thesis describes the physics of thin film silicon solar cells and their Schottky interface with zinc oxide (ZnO). Here, current-voltage-temperature (*I*-*V*-*T*) measurements and computer simulations are used in order to evaluate the Schottky barrier height of ZnO/a-Si:H(p) and ZnO/µc-Si:H(p) heterojunctions. It is observed that a high doping concentration of the p-layer can reduce the effective Schottky barrier height by increasing the tunnelling transport mechanism at the interface. The same heterojunctions are also tested in ZnO/p-layer/a-Si:H(i)/a-Si:H(n)/ZnO/Ag solar cells. It is found that despite the superior electrical properties of the ZnO/µc-Si:H(p) contact compared to the ZnO/a-Si:H contact, an improved performance is observed in cells using the latter. This contradictory result is explained by a misalignment of the energy bands at the µc-Si:H(p)/a-Si:H(i) interface. This reduces the open

circuit voltage (V_{OC}) of the cell in comparison to the a-Si:H(p)/a-Si:H(i) structure. These results lead to the theory behind optimization of a mixed µc-Si:H(p)/a-Si:H(p) window layer that can overcome the Schottky interface without compromising the p-layer/a-Si:H(i) interface.

Further, the conventional equivalent electronic circuit of a solar cell is expanded with a Schottky diode in series that represents the non-ideal contact. The analysis of this equivalent circuit shows that non-ideal metal/semiconductor contacts for solar cells can be approximated as Ohmic when they show a Schottky barrier lower than 0.5 eV. Also, the same model allows to distinguish the sections of the cell that degrade during light exposure and current injection. It is observed that all of the solar cells analysed here show a reduction of their V_{OC}, short circuit current (J_{SC}) and fill factor (*FF*) as a function of time when soaked with 1 Sun light, whereas the fully a-Si:H solar cells show a simultaneous increase of V_{OC}, a decrease of *FF,* and a minimal decrease of J_{SC} as a function of time when injected with a constant current of 10 mA in the dark. Increase in recombination in the absorption layer of the cell during light exposure can be detected by an increase of the ideality factor (*m*) of the main junction. On the other hand, the ideality factor (*n*) of the Schottky junction decreases after current injection. This indicates a detrimental effect on the tunnelling transport mechanism at the contact. Computer simulations reveal that the decrease of *n* is the result of a change in the a-Si:H(p) hole concentration and doping profile due to the excess of electrons injected during stress. This degradation of the Schottky interface is not observed when µc-Si:H(p) is used as the p-layer.

This thesis demonstrates that a complete understanding of degradation of the *I-V* characteristics of an a-Si:H solar cell can only be achieved when all transport mechanisms of a Schottky contact are considered.

Table of contents

List of acronyms and abbreviations

µc-Si:H: Microcrystalline silicon hydrogenated.

a-Si:H(i): Intrinsic amorphous silicon hydrogenated.

a-Si:H(n): N-type amorphous silicon hydrogenated.

a-Si:H(p): P-type amorphous silicon hydrogenated.

a-Si:H: Amorphous silicon hydrogenated.

CID: Current induced degradation.

***FF*: Fill factor.**

***I* - *V*: Current – voltage.**

***J* – *V*: Current density – voltage.**

J_{SC}**: Short circuit current density.**

LID: Light induced degradation.

***m*: Ideality factor of the diode at the main junction.**

***n*: Ideality factor of the Schottky diode.**

pc-Si: Polycrystalline silicon.

P_{MAX}**: Maximum power point.**

PV: Photovoltaic.

SWE: Staebler-Wronski effect.

TCO: Transparent conductive oxide.

V_{OC}**: Open circuit voltage.**

ZnO: Zinc oxide.

CHAPTER 1.

INTRODUCTION

This chapter presents the motivation and objectives of this thesis. This is followed by a description of the basic semiconductor theory required to understand the working principle of a conventional solar cell. The discussion is then followed with a description of different solar cell technologies that have contributed to expand the production of electricity from sunlight. The focus is on thin film silicon solar cells and how they compare with crystalline silicon, the most common material used for photovoltaic applications. The advantages and drawbacks of each type of cell are also presented.

At the present time, the average power demand worldwide is 10 terawatts (TW), and this quantity is estimated to increase to 30 TW by 2050 [1.1]. This high demand for energy casts doubts in the development of a sustainable future. Furthermore, an increase of pollution can be expected if unclean energy sources such as coal or gas continue to be used. For example, the power industry alone emitted 10.9 Gigatonnes of carbon dioxide equivalents ($GtCO_2e$) in 2005, and this quantity is expected to increase to an approximate of 18.7 $GtCO_2e$ per year by 2030 [1.2]. Therefore, there is significant interest in the use of renewable energy sources in order to address the energy requirements.

Among different renewable energy sources, solar energy represents the most abundant, inexhaustible and cleanest option to date. Earth intercepts $1.8x10^{11}$ MW of power from the Sun, a quantity that is many times larger than the actual power consumption [1.3] however, the challenge of delivering solar electricity exists in collecting the available solar energy at a reasonable cost.

One of the most useful renewable energy technologies is photovoltaic (PV), which directly converts sunlight into electricity by exciting electrons when light reaches a semiconductor material [1.4]. Light absorbed by a material promotes excited electrons to higher energy states however, these electrons eventually lose their energy and return to their ground state. On the other hand, a photovoltaic device separates the excited electrons before they relax and forces them to flow through an external circuit [1.5]. This phenomenon known as the photovoltaic effect was demonstrated for the first time in a completely solid-state system by Adams and Day in 1877, who managed to obtain an electric current in selenium exposed to light [1.6]. However, the first practical solar photovoltaic cell was created in 1954 by Chapin, Fuller and Pearson at Bell Labs. This solar cell was based on a p-n silicon junction and had an efficiency of 6% [1.7].

Significant interest was put into research and commercialization of solar cells during the 1970s after the first oil shock in 1973, and the second oil shock in 1979. However, the effort and interest in solar cells was short lived due to a lack of supporting policies and a fall in oil prices. Due to current volatility of fossil fuel prices, global warming, and an increasing

power demand, solar cells are an attractive technology to invest and investigate. In fact, more than 40 GW of solar based electricity have been installed by the end of 2010 (shortly before the beginning of this research) from an almost inexistent capacity during the early nineties, and it has accumulated to 227 GW by the end of 2015 (at the end of this research) [1.8].

1.1 Objectives and structure of this thesis

1.1.1 Motivation

The motivation of this thesis is to advance knowledge related to the characterization and design of contacts for thin film silicon solar cells in order to quantify their effects on the performance and stability.

1.1.2 Topics addressed in this thesis

1) ZnO/p-type thin film silicon interface: One of the most critical points to design a thin film solar cell is a transparent, highly conductive Ohmic contact. Unfortunately, some common interfaces such as ZnO/a-Si:H(p) present misalignments of their energy bands, which can create Schottky contacts that affect the performance of the cell. This undesired effect is often ignored in computer simulations and electronic circuit modelling of solar cells. This issue is addressed by conducting electrical characterization of specially fabricated ZnO/a-Si:H(p) and ZnO/µc-Si:H(p) diode structures.

2) Effect of the ZnO/p-type thin film silicon window layer on the performance of the cell: Electrical characterization, computer simulations, and electronic circuit modelling reveal that the ZnO/µc-Si:H(p) structure shows the best contact properties but compromises the subsequent µc-Si:H(p)/a-Si:H(i) interface, which causes a drop in performance in comparison to a cell with a ZnO/a-Si:H(p) interface. This makes the cell with ZnO/µc-Si:H(p) interface overall less efficient than the fully amorphous cell.

3) Effect of the ZnO/p-type thin film silicon window layer on the stability of the cell: The performance of the cells is measured as a function of time of exposure to light and current injection. The combination of these two degradation techniques along with the complete electronic circuit model presented in this thesis allows to identify different rates of degradation of the solar cell parameters, related to the intrinsic and window layers.

1.1.3 Chapters of this thesis

Following the introduction, chapter 2 describes common parameters used to evaluate the performance of solar cells and their conventional electronic circuit model. Also, the characterization techniques used in this thesis, as well as a methodology to improve the accuracy of experimental measurements are described in this chapter.

In chapter 3 the semiconductor theory required to understand the formation of a Schottky contact and the techniques used to experimentally evaluate the Schottky barrier height are presented. Non idealities of the current-voltage curve of a Schottky contact are analysed by discussing different transport mechanisms at a metal-semiconductor interface.

In Chapter 4 the results of computer simulations and experimental current-voltage-temperature measurements of special ZnO/a-Si:H(p) and ZnO/µc-Si:H(p) diode structures are shown. The purpose of this study is to identify the best contact for a cell.

A discussion on the design of a window layer for thin film silicon solar cells is introduced in Chapter 5. It is demonstrated here that band misalignment between the window layer and the intrinsic region needs to be considered as well as the interface with ZnO. Computer simulations are used here to optimize the p-layer. This chapter also presents with more detail the complete electronic circuit and the effect of its different elements on the performance of the cell.

The experimental part of this thesis is finalised in Chapter 6 via a study of the stability of the solar cells with different types of p-layers. Different forms of degradation are observed

when the cells are degraded with light exposure or with current injection. The effect of each degradation technique is observed with the change of magnitude of the different elements of the corresponding electronic circuit.

1.2 Doping of semiconductors

The formation of a p-n junction and basic concepts of semiconductors are first described in order to understand the working principle of a conventional solar cell. These are explained here for a semiconductor made of silicon, since this thesis is about thin film silicon solar cells. However, p-n junctions can be fabricated with other elements too. Fig. 1.1 shows a 2-D representation of a crystalline silicon, where each silicon atom shares a bond with four other silicon atoms around it. At this point, the semiconductor is known as an intrinsic semiconductor. However, if atoms of different elements (impurities) than the crystal are introduced into the structure, then the material becomes an extrinsic semiconductor. This process of introduction of impurities is known as doping, and its purpose is to change the electrical properties of a semiconductor. If the doping concentration becomes significantly high, the material starts behaving more like a conductor and it becomes a degenerate semiconductor.

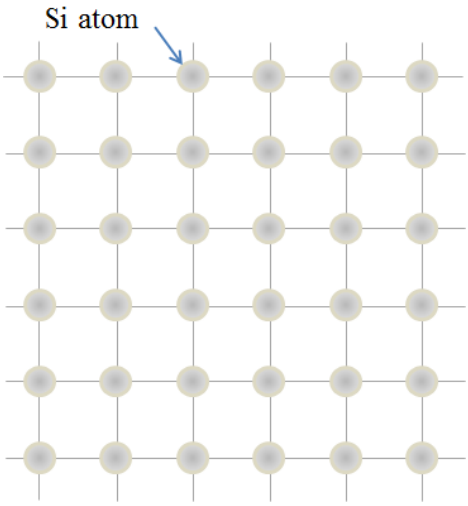

Figure 1.1. 2-D representation of a crystalline silicon structure. Each silicon atom shares a bond with four other silicon atoms.

Fig. 1.2 shows two different types of extrinsic semiconductors based on the structure shown in Fig. 1.1. Since silicon is an atom with four electrons at its highest energy level (valence electrons), an excess of electrons in the structure is achieved by doping with elements with more than four valence electrons such as phosphorus, as shown in Fig. 1.2a. This results in an n-type semiconductor. On the other hand, an excess of holes is achieved when the silicon crystal is doped with atoms with less than four valence band electrons such as boron, as shown in Fig. 1.2b. This results in a p-type semiconductor. For the n-type case, electrons become the majority carriers and holes the minority carriers, whereas the opposite is true for the p-type semiconductor. In both cases, majority carriers are mainly responsible for the transport of current.

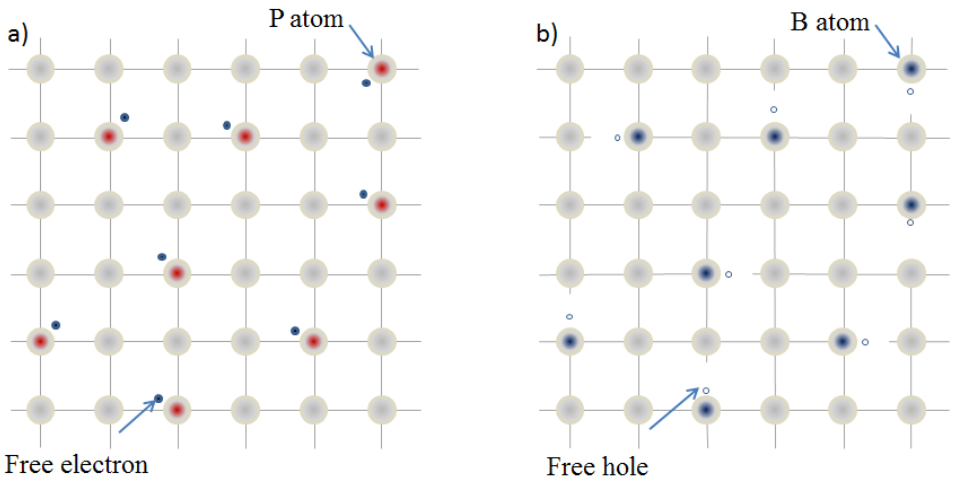

Figure 1.2. 2-D representations of crystalline silicon structures doped with different elements. a) An excess of electrons is achieved when phosphorus atoms with 5 valence electrons are introduced into the silicon crystal. This produces an n-type semiconductor. b) An excess of holes is achieved when boron atoms with only 3 valence electrons are introduced. This produces a p-type semiconductor.

1.3 Fermi level

The probability $F(E)$ of an energy state being occupied is represented by Fermi-Dirac statistics in Eq. 1.1, where k is the Boltzmann constant, and E_f is the Fermi level, which represents the value of energy where all states below are occupied and all states above are

empty at a temperature of 0 K. Alternatively, the Fermi level for an undoped semiconductor can be defined as the value of energy where the probability of a state being occupied is 0.5 at any temperature, as shown in Fig. 1.3 [1.9].

$$F(E) = \frac{1}{\frac{E-E_f}{e^{kT}}+1} \tag{1.1}$$

Since each electron that jumps to the conduction band leaves a hole in the valence band, the number of electrons and holes at the conduction and valence bands respectively, is the same. This means that $F(E)$ represents the probability of an energy state being occupied for an electron while 1-$F(E)$ means the probability of a state being unoccupied by an electron or in other words, occupied by a hole. Because of the symmetry that exists around the Fermi level, then E_f must be approximately in the middle of the band gap for intrinsic materials, if represented as energy bands, as shown in Fig. 1.4.

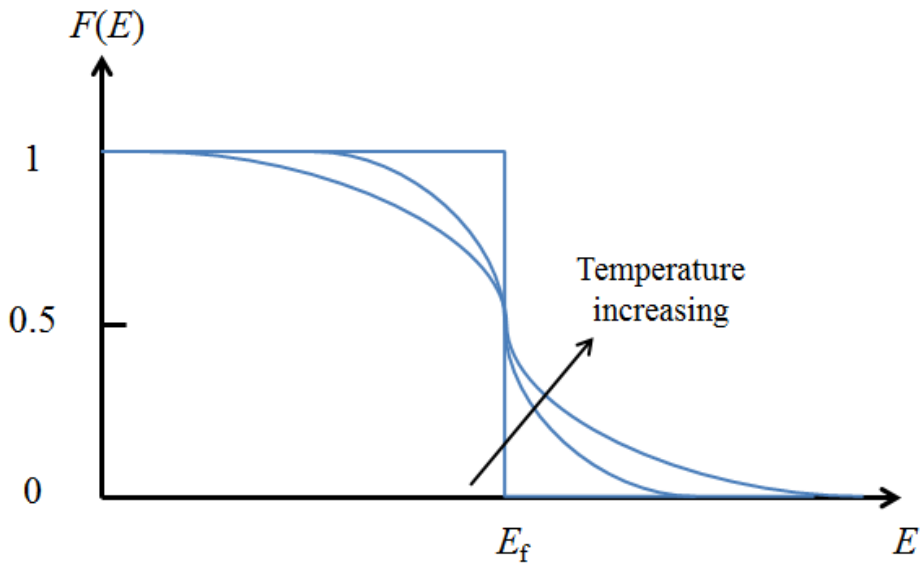

Figure 1.3 Plot of probability of a state being occupied $F(E)$ vs energy (E) for an intrinsic material. The value of energy independent of temperature at which $F(E)$=0.5 is known as Fermi level (E_f).

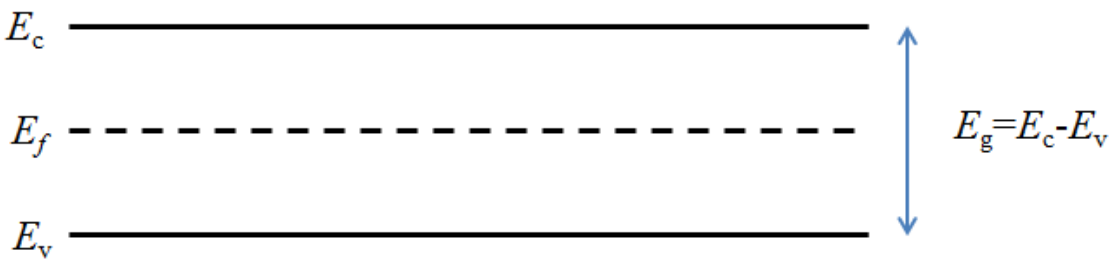

Figure 1.4. Energy bands for an intrinsic material. The Fermi level is in the middle of the gap.

Additional states of energy are created within the bandgap of extrinsic materials due to the introduction of different doping elements. For example, an n-type doping element such as phosphorus in silicon introduces new energy levels near the conduction band, which are filled by electrons at absolute zero and thus, a low energy is required for electrons to jump to the conduction band. This energy level is known as donor level. If p-type impurities are used to dope an intrinsic material, then the energy states are introduced near the valence band, which are empty of electrons at absolute zero. This new energy level is able to accept electrons from the valence band as the temperature increases. As a consequence, the valence band is filled with holes therefore, this level is known as the acceptor level [1.10]. Both of these situations are represented in Fig. 1.5.

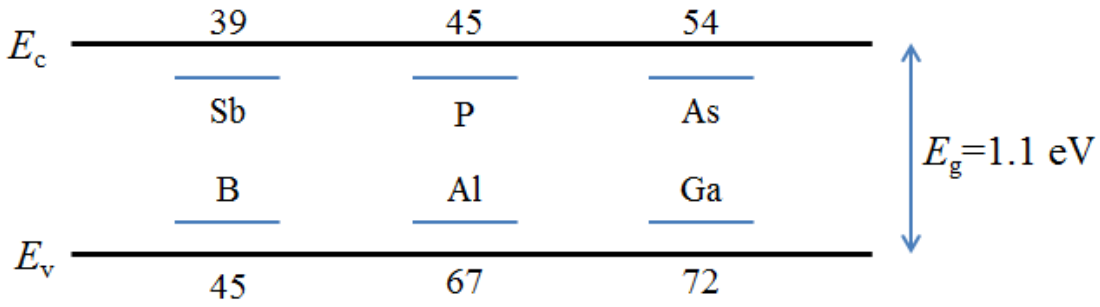

Figure 1.5. Additional states introduced by doping with different materials in a crystalline silicon structure. States introduced near the valence band in p-type semiconductors are known as acceptor levels, whereas states introduced near the conduction band in n-type semiconductors are known as donor levels. Values are in meV.

It is possible to calculate the concentration of electrons n_0 from the conduction band minimum by integrating the probability of occupancy of a state over an energy range, as shown in Eq. 1.2.

$$n_0 = \int_{E_c}^{\infty} F(E)N(E)dE \tag{1.2}$$

The concentration of electrons n_0 is calculated by integrating the product of the density of states $N(E)$ and the probability of a state being occupied $F(E)$ over the range E_c to infinity. $N(E)$ increases with electron energy in the conduction band but $F(E)$ decreases as energy increases. Finally, the product of $N(E)F(E)$ decreases steeply above the conduction band, which means that only a few electrons are able to keep higher than the bottom of the conduction band. The probability 1-$F(E)$ is used in order to find a hole, which decreases below the valence band and most holes are found at the top of the valence band.

The exponential term in Eq. 1.1 is normally large due to the product kT being small for the most common temperatures, thus it is possible to approximate it to Eq. 1.3.

$$F(E) = \frac{1}{\frac{E-E_f}{e^{kT}}+1} \approx e^{\frac{-(E-E_f)}{kT}} \tag{1.3}$$

The concentration of holes p_0 and electrons n_0 are shown in Eq. 1.4 and Eq. 1.5. These are obtained by substituting Eq. 1.3 into Eq. 1.2 and knowing that the probability of a hole occupying a state is 1-$F(E)$. Here, N_V and N_C represent the density of states at the valence and conduction bands respectively.

$$p_0 = N_V e^{\frac{(E_f-E_V)}{kT}} \tag{1.4}$$

$$n_0 = N_C e^{\frac{-(E_c-E_f)}{kT}} \tag{1.5}$$

Assuming the case of an intrinsic material, the product of concentration of holes and concentration of electrons would be given by Eq. 1.6.

$$n_0 p_0 = N_c N_v e^{\frac{-(E_c - E_v)}{kT}} = N_c N_v e^{\frac{-E_g}{kT}} = n_i p_i \tag{1.6}$$

where n_i and p_i represent the intrinsic concentration, and since $n_i = p_i$, then

$$n_i = \sqrt{N_c N_v} e^{\frac{-E_g}{2kT}} \tag{1.7}$$

$$n_0 p_0 = n_i^2 \tag{1.8}$$

The Fermi level for an intrinsic semiconductor (E_i) lies at the middle of the bandgap. This allows Eq. 1.4 and Eq. 1.5 to be rewritten in terms of the intrinsic concentration and the Fermi level.

$$n_0 = n_i e^{\frac{(E_f - E_i)}{kT}} \tag{1.9}$$

$$p_0 = n_i e^{\frac{(E_i - E_f)}{kT}} \tag{1.10}$$

Eq. 1.9 and Eq. 1.10 allow to calculate the Fermi level for an extrinsic semiconductor when the density of impurities are known. It can be understood that there will be a shift in the Fermi level of an intrinsic material as the doping concentration is increased. This shift will be to the conduction band for an n-type semiconductor and to the valence band for a p-type semiconductor (see Fig. 1.6).

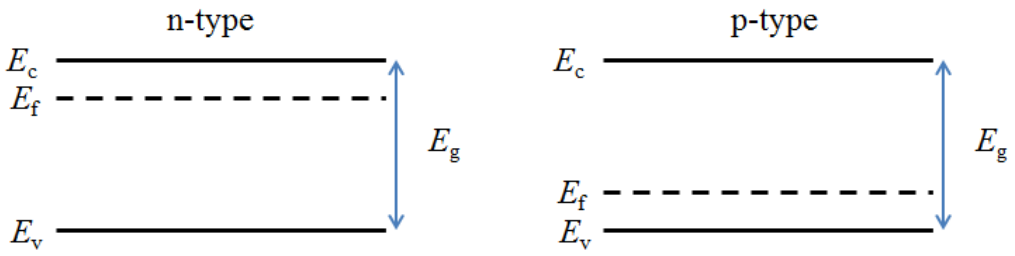

Figure 1.6. Shift in the Fermi level for different types of dopants. The n-type impurities push the Fermi level up towards E_c, whereas p-type impurities lower it down towards E_V.

Finally, if the doping concentration is increased even further, the shift of the Fermi level can overlap or even surpass the energy bands. As an example, Fig. 1.7 shows the band diagram of a degenerate n-type semiconductor, where the Fermi level is above the conduction band. As a consequence, the conductivity of the semiconductor increases significantly. In this thesis, ZnO is used as a degenerate semiconductor that acts as the contact of the solar cell, as will be further explained.

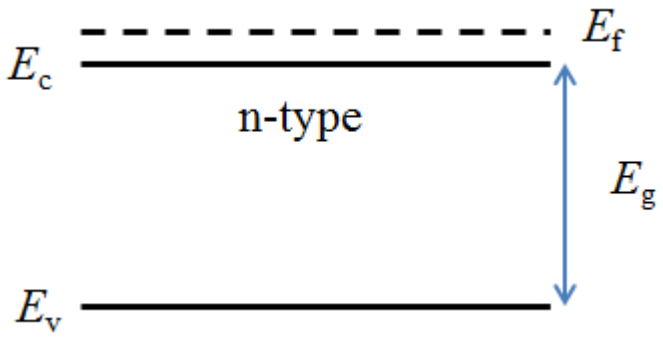

Figure 1.7. Energy bands and Fermi level for a degenerately doped n-type semiconductor.

1.4 Formation of a p-n junction

A p-n junction represents the basic working principle of the majority of solar cells. This junction is created at the point where an n-type material and a p-type material contact each other. This is done by introducing dopants of opposite polarity into an already doped semiconductor. Fig. 1.8 describes the different steps of the process to produce a p-n junction.

Fig. 1.8a) starts with an extrinsic n-type semiconductor such as silicon doped with phosphorus. Here, the phosphorus atoms are fixed to the crystal, whereas the extra electrons introduced are free to move. Phosphorus atoms become donors and are represented as P^+ ions, since their net charge is positive when they done electrons. Fig. 1.8 b) shows a p-type semiconductor such as silicon doped with boron that is grown next to the n-type semiconductor previously described. For the case of the p-type semiconductor, the fixed atoms become acceptors and are represented as B^- ions, since they become negatively charged when they accept electrons (or emit free holes). Once both materials are in contact, the free electrons flow from the zones with higher electron concentration to those of lower electron concentration. This process is called diffusion, and it is also experienced by free holes, which also flow from the zones with higher hole concentration to those of lower hole concentration. The diffusion of electrons and holes is shown in Fig. 1.8c). On the other hand, the P^+ ions remain fixed to the n-type side, whereas the B^- ions remain fixed to the p-type side. This produces an electric field *E* between the positive and negative ions that accelerates the holes in the direction of *E*, whereas the electrons are accelerated in the direction opposite to *E*. This movement due to the presence of an electric field is called drift, and is shown in Fig. 1.8d). The electric field also produces a region that is depleted of free carriers, hence called a "depletion region", shown in Fig. 1.8e). However, despite the electric field, some free carriers still have sufficient energy to cross the depletion region, even at equilibrium. Finally, a built-in potential V_{bi} is produced at the junction due to the electric field.

Once isolated n-type and p-type materials are brought into contact, the Fermi levels (shown in Fig 1.6), must align at the same level therefore, the bands have to bend in order to reach this condition. Fig. 1.9 shows the band diagram of a p-n junction of semiconductors with the same bandgap, which receives the name of homojunction. Additionally, Fig. 1.10 shows a junction where the depletion region has been extended with the introduction of an intrinsic layer in between the extrinsic layers. This results in a p-i-n junction, which is preferred as the standard structure for thin film silicon solar cells, as will be expanded further.

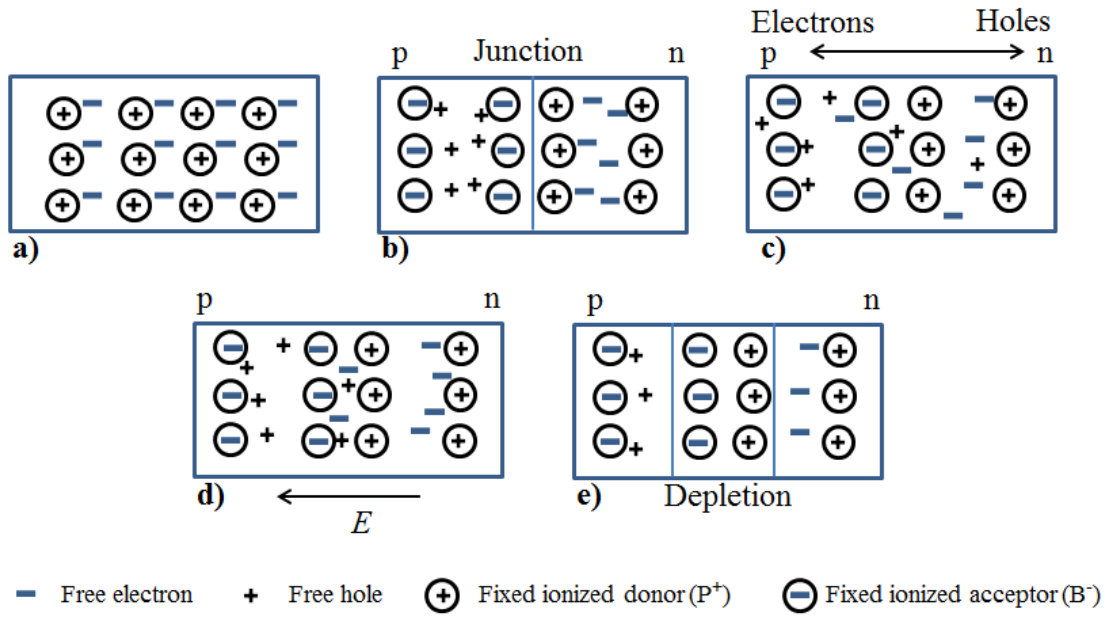

Figure 1.8. Formation of a p-n junction. a) N-type doped material. b) P-type semiconductor grown next to the n-type semiconductor. c) Diffusion of free carriers. d) Electric field is created and balances the diffusion current. e) Equilibrium.

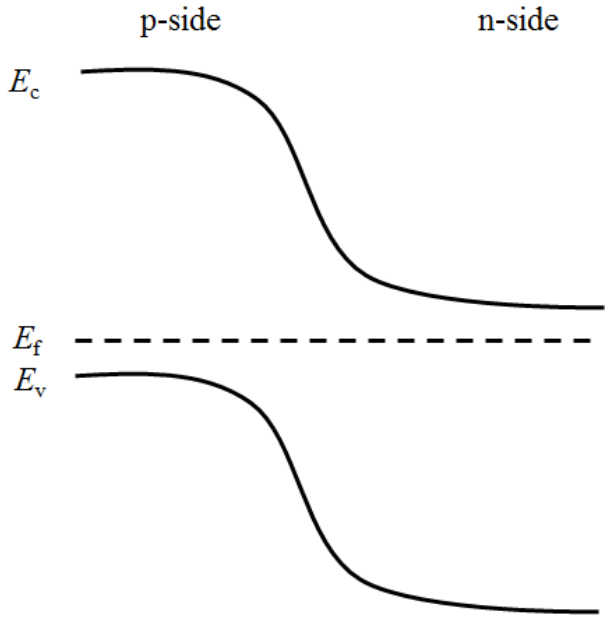

Figure 1.9. Energy band diagram of the p-n homojunction. Fermi levels must align at the same level.

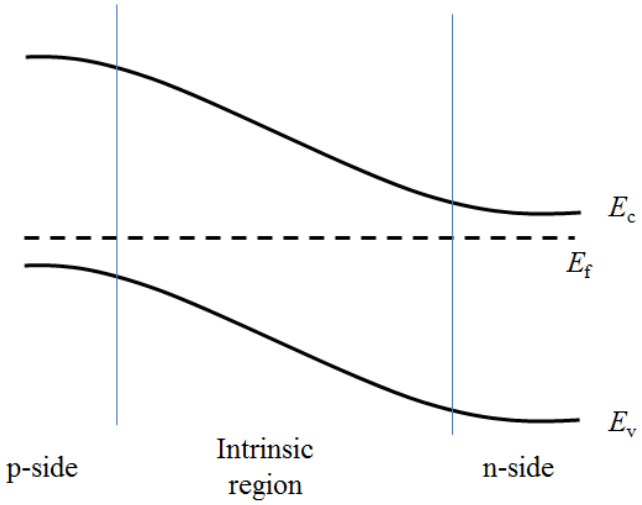

Figure 1.10. Energy bands diagram of a p-i-n homojunction. Fermi levels must align at the same level.

It is also possible to fabricate p-n or p-i-n junctions using materials with different bandgaps. This type of junction receives the name of heterojunction. The use of materials with different bandgaps produces a discontinuity in the valence and conduction bands once both materials are in contact. This difference in the energy bands modifies the electric field, in a way that it can either assist or oppose the transport of free carriers. As an example, Fig.

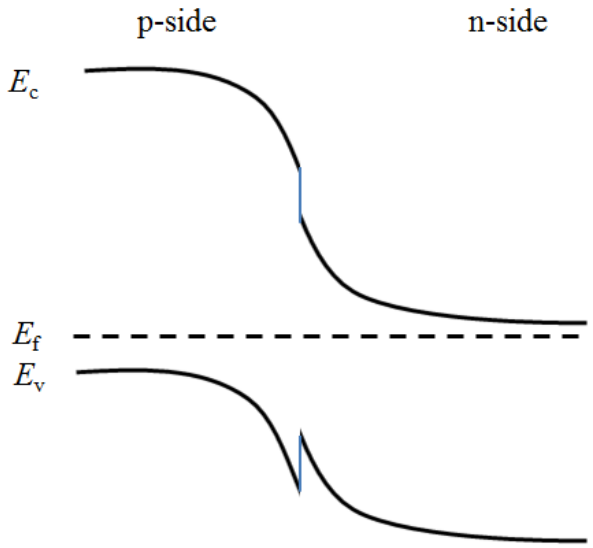

Figure 1.11. Example of the energy band diagram for a p-n heterojunction.

1.11 shows the band diagram of a p-n heterojunction, where the bandgap of the n-type semiconductor is narrower than the bandgap of the p-type semiconductor. In this case, the discontinuity of the energy bands does not present an opposition to the electrons that are driven by the field downhill towards the n-side, whereas the holes find opposition at the discontinuity on their way towards the p-side.

1.5 Principles of a conventional solar cell

When light with energy $E=h\nu$ where h is the Planck's constant and ν the frequency of the radiation, shines on a semiconductor, one of the following situations may occur:

1) If the energy of the photons is smaller than the band gap of the semiconductor, then the material acts transparent to light.

2) If the energy of the photons is equal to or higher than the band gap of the semiconductor, their energy is absorbed by the material, which allows the electrons to jump to the conduction band, leaving a hole in the valence band. Energy from the photons that exceeds the band gap is transformed into heat.

For every electron that is able to jump to the conduction band, a corresponding hole is left behind in the valence band. It is this separation of charge which causes the photovoltaic effect. If these charges are kept separated from each other and moved into opposite directions, a photocurrent (under short circuit conditions) or a photovoltage (under open circuit conditions) are produced. The electric field introduced by the p-n junction is responsible to move the charges in opposite direction through an external circuit, where electrons lose energy by doing work such as producing heat, light or movement, to finally return to the semiconductor, where they can repeat the cycle, as shown in Fig. 1.12. It is observed that the contacts are attached to each side of the p-n junction. Their purpose is to collect the separated carriers and allow them to move through the external circuit. For a crystalline silicon solar cell, these contacts are usually made of aluminium or silver, whereas the preferred contact for thin film silicon solar cells is indium tin oxide (ITO).

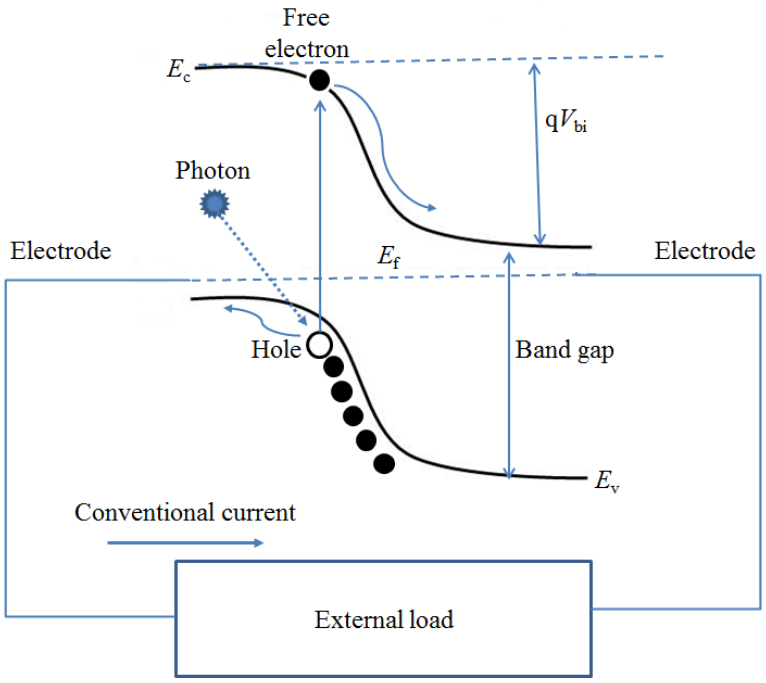

Figure 1.12 Photovoltaic effect. Light is absorbed by the semiconductor and makes electrons to gain enough energy to jump from the valence band to the conduction band. Charges are circulated through and external circuit by the use of contacts.

1.6 Types of solar cells

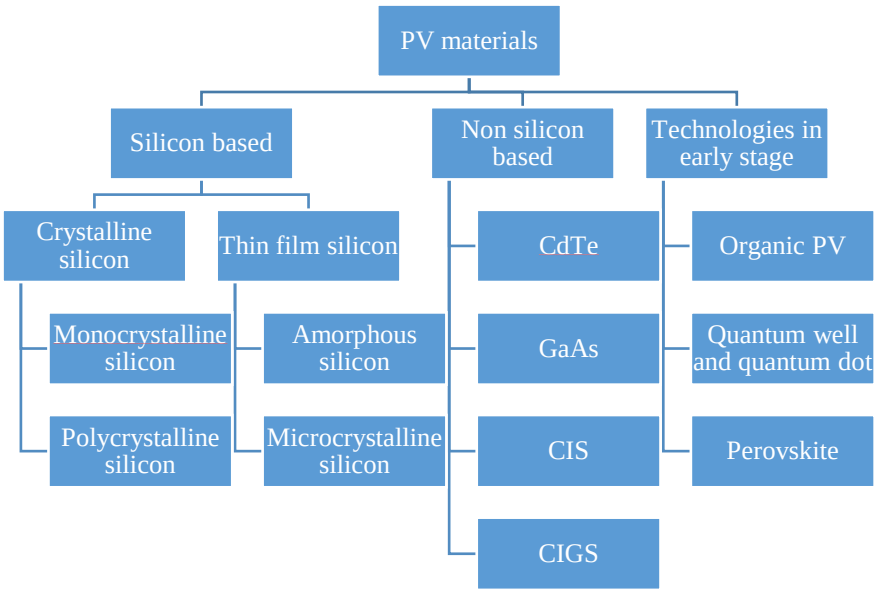

Figure 1.13. The diagram shows different materials and concepts used to fabricate solar cells. The content of this thesis focuses mainly on thin film silicon materials.

A solar cell requires a light absorbing material in its structure in order to transform the radiant energy of the Sun to electricity via the photovoltaic effect. Fig. 1.13 presents different materials used to fabricate solar cells, which are mainly classified as silicon and non-silicon based materials. The reason for this broad classification is because silicon, in its different forms, represents approximately 90% of the PV industry [1.1], whereas materials such as CdTe, $CuInSe_2$ (CIS) and $CuInGaSe_2$ (CIGS) represent the remaining part of the market. Organic PV, perovskites, quantum well and quantum dot solar cells are still under development. The performance of all these technologies is compared by evaluating the ratio of maximum power output supplied by the cell and input power received. The result is the most basic parameter of the cell known as the solar cell conversion efficiency (η). Values of efficiency for different PV materials have been recorded to monitor the development of PV technologies, to summarize the latest achievements, and to encourage standardization of the reported results [1.11]. A plot of efficiency versus time can be seen in Fig. 1.14 for the different technologies.

According to the Shockley-Queisser limit, also known as the detailed balance limit of efficiency, the theoretical maximum efficiency of a single junction solar cell at a temperature T_C=300 K is approximately 30% for an energy gap of 1.1 eV [1.12]. This calculation assumes a solar cell is treated as a black body at a temperature T_C in thermal equilibrium which receives radiation from an external body at a temperature T_S as shown in Fig. 1.15. Here, the rate of radiation absorbed by the cell is equal to the rate of radiation emitted by the cell, which is calculated with Eq. 1.11.

$$R_{Rabsorbed} = R_{Remitted} = 2AQ_C \tag{1.11}$$

Here, A is the area of the solar cell, and Q_C represents the rate of incident photons with frequencies high enough to excite the electrons from the valence band to the conduction band (v), per unit of area per unit of time. This rate is calculated by integrating Planck's Law according to Eq. 1.12 to Eq. 1.14, where h is Planck's constant, c is the speed of light in vacuum, k is Boltzmann's constant, E_g is the bandgap of the junction, and T_S=6000 K is the temperature of the Sun.

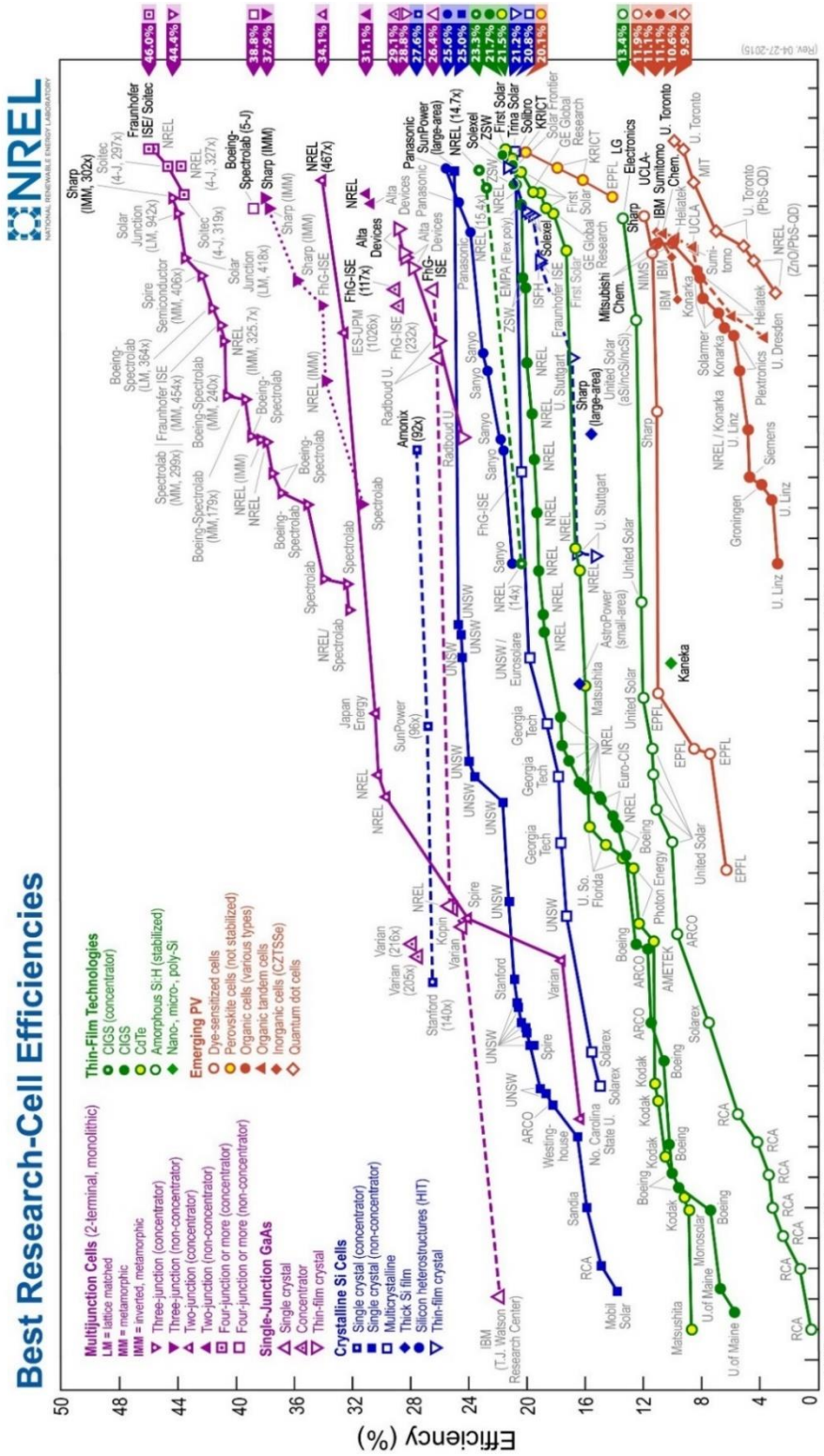

Figure 1.14. Improvement of efficiency over the years for solar cell technologies. [From http://www.nrel.gov/ncpv/images/efficiency_chart.jpg] Last time accessed on July, 2016. Used with permission of NREL. Disclaimer notice can be read on page 54.

$$Q_C = \frac{2\pi(kT_C)^3}{h^3c^2}\int_{x_g/x_c}^{\infty}\frac{x^2dx}{e^x-1} \quad (1.12)$$

$$x_g = {E_g}/{kT_S} \quad (1.13)$$

$$x_c = {T_C}/{T_S} \quad (1.14)$$

The theoretical efficiency of a cell is then calculated according to Eq. 1.15, where P_{MAX} is the maximum product of I and V evaluated from the current-voltage relationship shown in Eq. 1.16, and P_{IN} is the power emitted by the light source. Here, Q_S represents the rate of incident photons with frequencies high enough to excite the electrons from the valence band to the conduction band (v), per unit of area per unit of time, that are emitted by a black body of temperature T_S.

$$\eta = \frac{P_{MAX}}{P_{IN}} \quad (1.15)$$

$$I = \frac{Q_S}{Q_C} - 2AQ_Ce^{\frac{qV}{kT_C}} \quad (1.16)$$

$$Q_S = \frac{2\pi(kT_S)^3}{h^3c^2}\int_{x_g}^{\infty}\frac{x^2dx}{e^x-1} \quad (1.17)$$

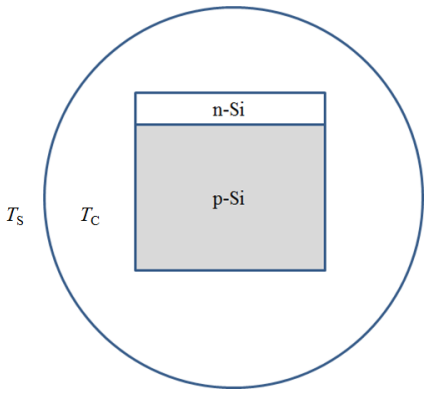

Figure 1.15. Solar cell at a temperature T_C that receives radiation from a black body at a temperature T_S.

1.6.1 Non silicon based PV materials

1.6.1.1 Cadmium telluride (CdTe)

CdTe technology has the advantage of a great diversity of simple and low cost methods of fabrication such as thermal evaporation, electro-deposition, chemical vapor deposition, screen printing, sputtering and many more, from which efficiencies higher than 10% have been obtained, whereas the world record is approximately 21%, achieved by First Solar [1.13]. Furthermore, the energy bandgap of CdTe E_g=1.45 eV fits the ideal range to convert solar energy. These two qualities make CdTe a promising material for mass production of solar cells. However, a disadvantage of CdTe solar cells is the variation in performance of practically identical devices which show a relative change up to 10% even for cells that are deposited on the same substrate [1.14]. These variations in performance are not completely understood, but are commonly attributed to poor contacting, sensitivity to humidity and quality of the materials [1.15]. The availability of Te is also a concern due to the shortage of this material, which could be a problem for mass production of panels. Finally, the biggest concern is the toxicity of cadmium and the impact it could have on the environment, something that had led First Solar to introduce a recycling program for panels.

1.6.1.2 Copper indium diselenide (CIS) and copper indium galium diselenide (CIGS)

CIS is an attractive material for thin film solar cells due to its high optical absorption coefficient, which allows for very thin layers. Although the bandgap of CIS is only 1 eV, replacement of indium with an indium-gallium alloy in CIGS allows a bandgap up to 1.68 eV thus, enhancing the output voltage under open circuit conditions. This is done by controlling the ratio of Ga/(In+Ga).

Development of CIS solar cells started in 1974 with Wagner [1.16]. At that time, single crystalline cells used to have a conversion efficiency of 12%. Two years later, the first thin film CIS cell was fabricated by Kazmerski, although its efficiency was only 4% [1.17].

An efficiency of 19.9% for a CIGS solar cell was reported in publication by Repins from the National Renewable Energy Lab (NREL) [1.18], and currently improved to 20.5% by Solibro [1.19]

Some of the concerns faced by CIS and CIGS are the complex process of production and the difficulties to produce uniform CIS absorber layers over large areas. This non-uniformity along with the scarce availability of materials such as indium, represent significant obstacles for mass production.

1.6.2 Crystalline silicon

1.6.2.1 Monocrystalline silicon

Crystalline silicon is the leading market technology. These are fabricated by the Czochralski method, which produces a single crystal almost free of defects.

Through the years, the improvements in efficiency of silicon solar cells have been attributed to multiple reasons. In 1948, the first silicon solar cell produced, achieved an efficiency of 15%. By 1970, the advances of microelectronics fabrication procedures such as photolithography allowed a further increase up to 17%. Later, improvements in contacts, light trapping mechanism and standardisation of the measurement process contributed to reach the current efficiency values of 25% reported by Green from the University of New South Wales (UNSW) [1.20].

A schematic diagram of the basic structure of a p-n crystalline silicon solar cell is shown in Fig. 1.16, where p-Si represents silicon doped with boron and n-Si stands for silicon doped with phosphorus. A front contact and antireflective coating layer is used to prevent reflection of light at the top surface and at the same time, prevent light reflected from the back contact (a highly reflective and conductive metal) to escape from the solar cell. The front contact also includes a metallic grid. This grid includes bus-bars, which are connected to the external leads, and fingers, which are finer conductors that collect the current of the

cell and deliver it to the bus-bars. The dimensions of the grid must be optimized to collect the current of the cell, without compromising the absorption of light by the inner layers.

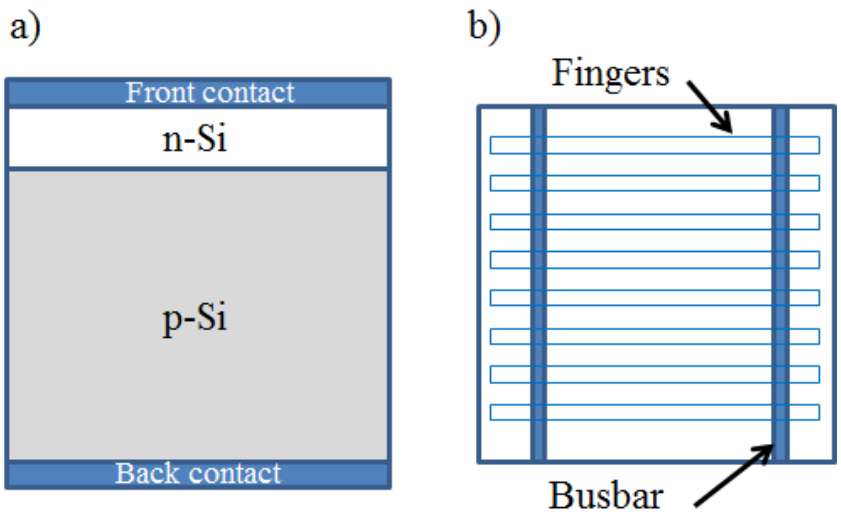

Figure 1.16. a) Structure of a conventional silicon solar cell using p-type and n-type doped materials. b) Top view of a crystalline silicon solar cell, which shows bus bars and fingers used as top contacts.

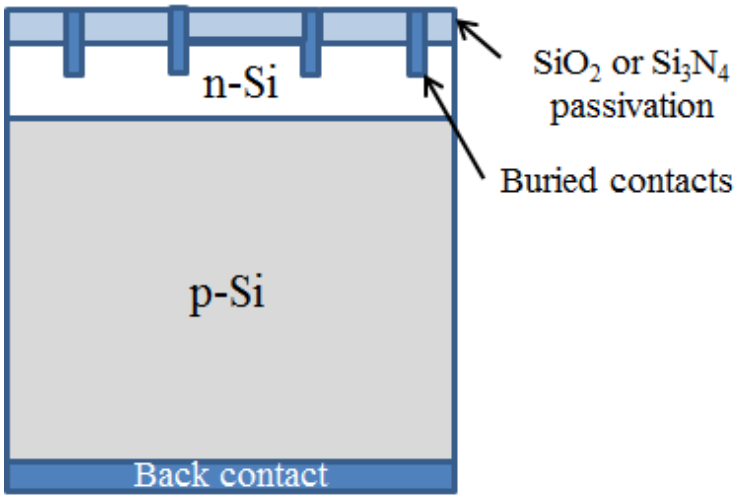

Figure 1.17. Conventional solar cell using the buried contact approach in order to minimize shadowing at the surface

A modification of the front contact that allowed an increase in performance of the cell and at the same time, reduction of costs, was the introduction of buried contacts as shown in Fig. 1.17 [1.21]. In this approach, a laser is used to create cavities at the top surface where metal layers are inserted. This reduces the area of contact of the metal grids, and allows more light to reach the inner layers.

1.6.2.2 Polycrystalline silicon

Chemical vapour deposition (CVD) allowed the growth of multiple crystals of silicon oriented in fixed positions by chemical decomposition of trichlorosilane ($HSiCl_3$) on top of pre-existing pure silicon seed rods. This process is simpler and more economic than production of monocrystalline material. However, the existence of multiple crystals introduces grain boundaries between them, which results in a higher concentration of vacancies, interstitial defects and dislocations. Also, pc-Si often contains a higher density of impurities such as oxygen, since less pure material can be tolerated by the fabrication equipment. Schultz from the Fraunhofer Institute for Solar Energy Systems applied wet oxidation for rear surface passivation and reported pc-silicon cells with efficiency higher than 20% in 2004 [1.22]. Since then, the efficiency of polycrystalline solar cells has stagnated and Verlinden from Trina Solar holds the current record of 20.8% [1.23]. Typical values of efficiency for commercial solar panels are approximately 12% to 15% [1.1].

The crystalline silicon on glass (CSG) approach developed by Green and Basore reduces the quantity of material required for a solar cell [1.24]. Here, silicon is deposited directly on glass and then crystallised, which allows a reduction in thickness of silicon. This reduces the fabrication cost however, the efficiency is also reduced to 8-9%.

1.6.3 Thin film silicon

Since the Shockley-Queisser limit for a single junction solar cell is approximately 30%, there are minor opportunities to improve a crystalline cell in terms of performance, since the world record efficiency of a monocrystalline solar cell is already 25% [1.20].

Therefore the primary objective of the PV industry has become the reduction of cost in order to be competitive with conventional energy sources.

An attempt to reduce the cost of solar electricity is by the use of thin film technologies, the second generation of PV devices, which in contrast to crystalline silicon, can be deposited on cheap substrates with a total thickness of 50 μm approximately, thus requiring less material. Another advantage is that the efficiencies of thin film technologies are still far from their theoretical values, which allows great opportunities of improvement in terms of performance as well.

Currently, thin film technologies represent 10% of the solar PV market share. These technologies include amorphous silicon (a-Si), microcrystalline silicon (μc-Si) and thin polycrystalline. Also, CdTe and CIGS solar cells are considered as thin film solar cells, although non-silicon based. Common aspects of these cells are:

1. Fabrication on foreign substrates such as glass or stainless steel (silicon wafers are not needed).

2. Transparent conductive oxides (TCOs) are used as front contacts, and sometimes as a back contact along a highly reflective material such as silver in order to trap the light inside the solar cell. Furthermore, the use of TCOs allows to extract the current from the solar cell without impeding the light to reach the absorbing layer. More details about TCOs are presented in section 1.2.5.2.

3. Two different options of fabrication are possible depending on the application. These are the substrate and superstrate configuration as shown in Fig. 1.18. For the substrate approach, deposition of the layers occurs from back to top, starting with the back reflector and finishing with the TCO. Lightweight, resistant and even flexible substrates are normally used, which can be opaque or transparent, such as stainless steel or polyethylene terephtalate (PET) respectively. When the superstrate configuration is used, deposition of the layers occurs from top to bottom, starting with the TCO in contact with the main junction and

finishing with the back reflector. An important requirement is for the front TCO to be electrically conductive, highly transparent and chemically stable at the moment of deposition, otherwise, if any of these needs are not fulfilled, the performance of the cell can be affected.

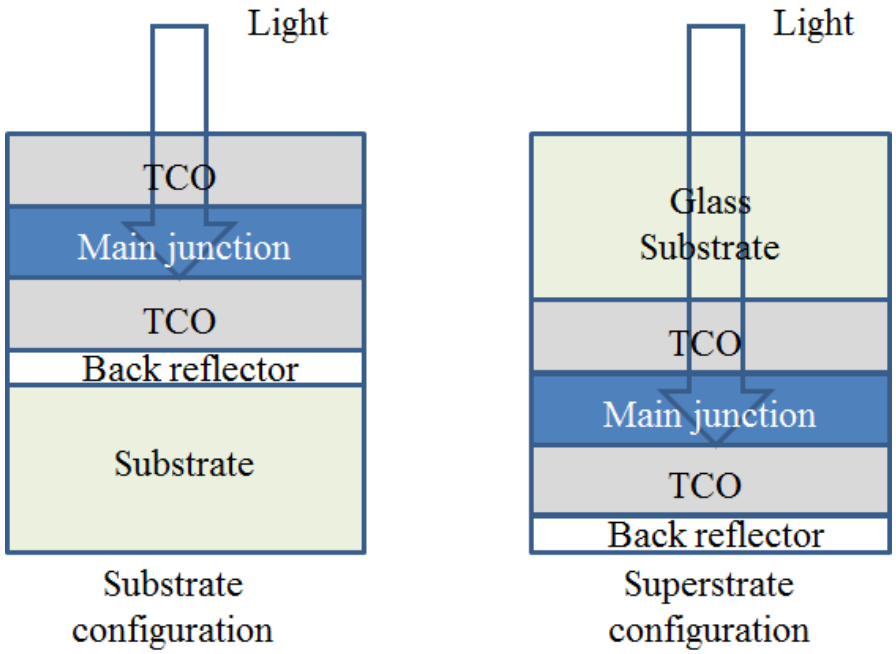

Figure 1.18. Substrate and superstrate configurations used for fabrication of thin film solar cells.

1.6.3.1 Amorphous silicon

Amorphous silicon is the most studied and used material for thin film silicon technologies. It shows a lack of translational periodicity (long range order) in its atoms, whereas crystalline silicon follows a tetrahedral structure where each silicon atom bonds four adjacent silicon atoms, which forms an ordered crystal. It is possible to grow crystals of crystalline silicon with a periodic structure in the range of centimetres. On the other hand, the short translational periodicity of amorphous silicon extends to less than 1 nm (See Fig. 1.19b).

An advantage of the amorphous structure is the increased coefficient of light absorption of approximately two orders of magnitude higher than crystalline material. Due to higher absorption it is possible to use layers with a thickness of only a few micrometres. However, the amorphous structure also brings some drawbacks, such as dangling bonds between silicon atoms, which represent a high density of defects of approximately 10^{19} cm^{-3}. It is possible to reduce the quantity of defects by introducing an element with atoms of small diameter such as hydrogen to pair with the electrons of unsaturated bonds (dangling bonds). The small diameter is required in order for the atoms to enter the atomic structure. This produces hydrogenated amorphous silicon (a-Si:H) and decreases the density of dangling bonds down to 10^{15} cm^{-3}. Another element that has been used in a-Si to reduce the quantity of dangling bonds is fluorine. This element was chosen due to the small diameter of its atoms and also due to its high electron affinity and large ionization energy, which produces a stronger covalent bond with silicon than H. However, hydrogen is preferred over fluorine as a dangling bond terminator in amorphous silicon due to its ease of implementation.

The introduction of hydrogen also increases the bandgap of the material to values around 1.7-1.8 eV. This widening of the bandgap can be explained as the replacement of weak Si-Si bonds at the top of the valence band with hydrogen atoms, which form stable Si-H bonds at deeper levels of energy. This gives the appearance that the valence band shifts downwards, whereas the conduction band stays practically at the same level, as reproduced by the theoretical calculations of Allan and Joannopoulos [1.25].

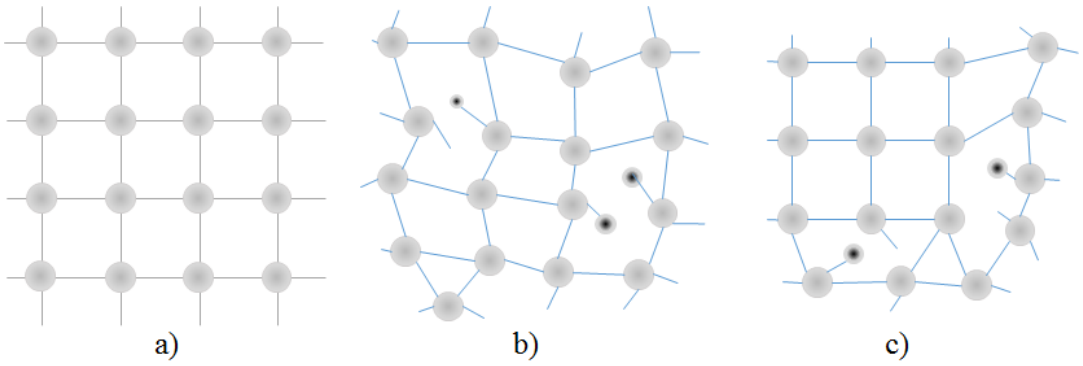

Figure 1.19. 2-D representation of different types of silicon. 1a) shows a crystalline structure, where every silicon atom shares each of their bonds with four other atoms. Ideally, defects are

non-existent for this case. 1b) shows a section of a-Si:H. Dangling bonds are found where atoms have unpaired bonds. In order to reduce these broken bonds, small diameter atoms such as hydrogen, are introduced. 1c) shows a transition phase from amorphous to crystalline. This structure is known as microcrystalline silicon. Dangling bonds also exist for this material.

1.6.3.2 Microcrystalline silicon

Microcrystalline silicon (μc-Si) is obtained as a transition phase from amorphous to crystalline silicon, where small crystals are found in an amorphous structure (Fig. 1.19c). The absorption coefficient of μc-Si is lower than that of a-Si thus, it requires thicker absorbing layers. Similarly to a-Si, μc-Si needs to be alloyed with hydrogen to passivate the dangling bonds of the amorphous region, which results in hydrogenated microcrystalline silicon (μc-Si:H). Since μc-Si:H is more effective at low wavelengths, it is possible to combine it with a-Si:H in a tandem structure to absorb the most useful part of the spectrum. Although the bandgap of μc-Si:H is approximately the same as that for crystalline silicon, its semi-disordered structure increases the absorption coefficient up to one order of magnitude. In1994, Meier from the Université de Neuchâtel produced the first complete μc-Si:H solar cell, showing an efficiency of 4.6% [1.26].

1.6.4 Issues with thin film silicon

Light induced degradation (LID) represents the major disadvantage of a-Si:H as a photovoltaic material. This reduces the output of a solar cell as a function of time when subject to illumination. This phenomenon was observed for the first time in 1977 by Staebler and Wronski, who found that the conductivity in a-Si:H can be reduced significantly by prolonged illumination to light (Fig. 1.20) Therefore, light-induced degradation is also referred as the Staebler-Wronski effect (SWE) [1.27].

As a consequence of LID, the efficiency of a-SI:H solar panels drops by a range of 10% to 30% during the first few months of operation. After this initial drop, a state of equilibrium is reached and minimal degradation is further observed. Although SWE is not fully understood, some experimental observations are [1.28]:

1) Degradation of the cell follows the power law $\Delta I = G^{\frac{n}{2}} t^n$ where n=1/3, *G* represents the flux of photons, and t represents the time of exposure.
2) A recovery of the cell performance is achievable once the light is removed.
3) Degradation of the solar cell increases with the intensity of the light shining on it.
4) Dissociation of Si-H is proposed during light soaking.
5) It is possible to reduce degradation if hydrogen is replaced by deuterium.
6) Crystalline silicon is also affected by LID but not as severely as a-Si:H.
7) LID is reduced by the use of thinner amorphous layers.

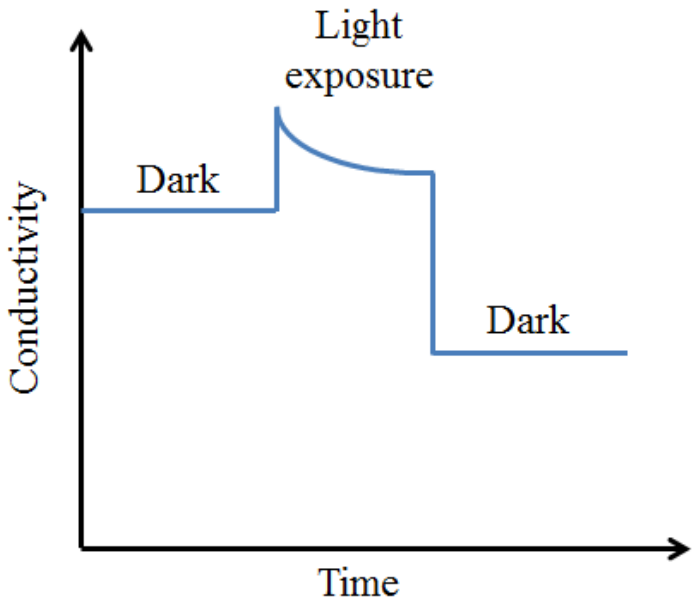

Figure 1.20. Changes in dark conductivity and photoconductivity of a-Si:H observed by Staebler and Wronski before and after some hours of exposure to light.

In the same year that LID was observed, Staebler and Wronski also reported the opposite effect in a-Si by annealing above 150 ºC [1.27]. Similarly, a solar cell that has been degraded can recover its initial characteristics when annealed in the dark, and the recovery rate is dependent on the temperature [1.29]. The changes in the slope of output power versus time are due to regeneration and degradation competing at the same time, resulting in an overall slower rate of degradation [1.30].

According to Stutzmann et al, recombination of electron-hole pairs occurs at the weak Si-Si bonds, which causes the transfer of a hydrogen atom to the weak Si-Si position and thus produces two dangling bonds, as shown in Fig. 1.21. The effect is opposite during thermal annealing. Based on this model, metastability of a-Si:H seems to be a result of the presence of hydrogen or silicon only and not because of impurities such as oxygen or carbon [1.31]. It was later concluded by Liu and Xu, that SWE is self-limiting and the creation rate of new dangling bond decreases with the square of already existing dangling bonds [1.32].

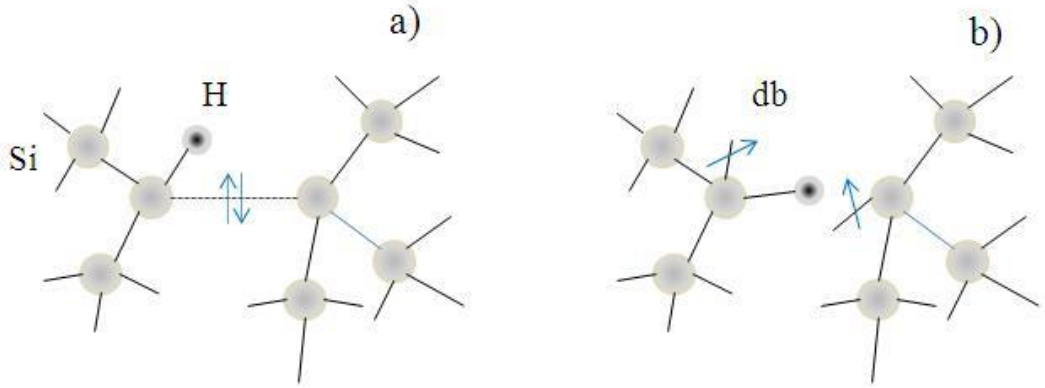

Figure 1.21. Weak Si-Si bond before exposure to light or after annealing (a). Broken Si-Si bond after exposure to light.

In the Stutzmann model, a quantity N_{DB} of dangling bonds is proportional to two thirds power of the incident radiation and one third power of the duration of light soaking ($N_{DB} \alpha I^{2/3} t^{1/3}$) however, instead of a continuous growth of dangling bonds, the rate of creation decreases with the square of the pre-existing density of dangling bonds [1.31]. This process is represented in Eq.1.18 and Eq. 1.19 [1.28], where G represents a flux of photons with sufficient energy to dissociate weak Si-H bonds with initial concentration N_0 at a rate k_F. Broken dangling bonds N_{DB} act as recombination centres and interact with released hydrogen atoms H, which allow an opportunity for repassivation k_R. Furthermore, hydrogen atoms can combine at a rate k_H to create molecular H_2.

$$\frac{dN_{DB}}{dt} = k_F N_0 G - k_R N_{DB} N_H \tag{1.18}$$

$$\frac{dN_{\mathrm{H}}}{dt} = \frac{dN_{\mathrm{DB}}}{dt} - k_{\mathrm{H}} N_{\mathrm{H}}^2 \tag{1.19}$$

An analytical solution of Eq. 1.18 and Eq. 1.19 leads to Eq. 1.20.

$$N_{\mathrm{DB}}(t) = (3K_{\mathrm{H}})^{1/3} \left(\frac{K_{\mathrm{F}} N_0 G}{K_{\mathrm{R}}}\right)^{2/3} t^{1/3} \tag{1.20}$$

Eq. 1.20 is comparable to the Stutzmann equation. Besides light photons, high energy particles, applied bias and current injection are some sources believed to cause instability by the same degradation mechanism. This degradation can be reversed by thermal annealing or even when light is not applied anymore. Ultimately, due to the power law followed by the creation of dangling bonds, an effective way to study degradation with respect to time is by a logarithmic equation (Eq. 1.21), where α is the slope of the line indicating the rate of degradation, and C is a constant. Due to this degradation, values of efficiency are reported after a test for light exposure of approximately 1000 hours. The current world records for a-Si:H and µc-Si:H solar cells are 10.2% by Matsui [1.33] and 11.4% by Sai [1.34] from the National Institute of Advanced Industrial Science and Technology, in Japan.

$$\frac{\eta}{\eta_0} = \mathrm{C} - \alpha \log(t) \tag{1.21}$$

1.6.5 Design of a thin film solar cell

1.6.5.1 P-I-N structure

Fig. 1.22 shows the structure of p-i-n solar cell on a glass substrate illuminated from the bottom. The same layers are used for a-Si:H and µc-Si:H solar cells. Boron atoms are used to dope silicon and produce an excess of holes in a-Si:H(p), while phosphorus atoms are introduced to produce an excess of free electrons in a-Si:H(n). The intrinsic section of undoped material a-Si:H(i), is the main photovoltaic layer, where the light is absorbed and carriers are separated to be collected by the p and n-type layers.

The main difference between a thin film solar cell structure and that of a conventional solar cell (p-n junction) is the introduction of an intrinsic layer between the p and n layers to create a p-i-n structure, which was used for the first time by Carlson at RCA Laboratories in 1976 [1.35] soon after Spear proved that it was possible to dope a-Si [1.36]. In a p-i-n structure, light that is absorbed in the n or p layers does not contribute to the photocurrent of the cell, instead these layers represent optical losses, but they are necessary to produce the electric field needed to drive the free carriers in opposite directions. For this reason, extreme care is needed to optimize the thickness (approximately 10 to 30 nm) and doping concentration of these layers in order to not interfere with light that is to be absorbed by the i-layer. Care is also needed in the intrinsic layer thickness which is not free of defects, as these defects reduce the electric field, producing non-uniformities of $E(x)$ along the p-i-n junction that complicates the collection of carriers (Fig. 1.23). Three characteristics that are desired in the intrinsic region are [1.37]:

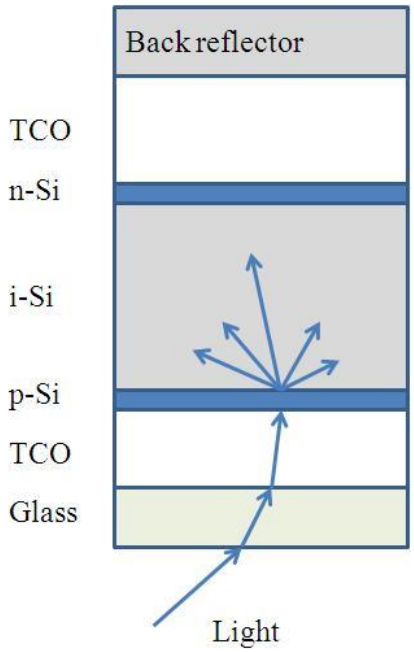

Figure 1.22. Structure of a p-i-n thin film silicon solar cell illuminated from the bottom. The intrinsic silicon layer is where light is absorbed generating electron-hole pairs that are separated to be collected by the p and n layers.

1) Optical absorption coefficient α (hν) needs to be high enough to absorb the useful spectral range of the solar radiation. Values of α for crystalline and thin film silicon are plotted in Fig. 1.24 as a function of energy.

2) A high product of mobility and lifetime ($\mu\tau$) for electrons and holes.

3) The electric field $E(x)$ must be high enough so that the drift length at the i-layer ($L_{drift}=\mu\tau E$) is greater than the thickness of the same i layer (d_i).

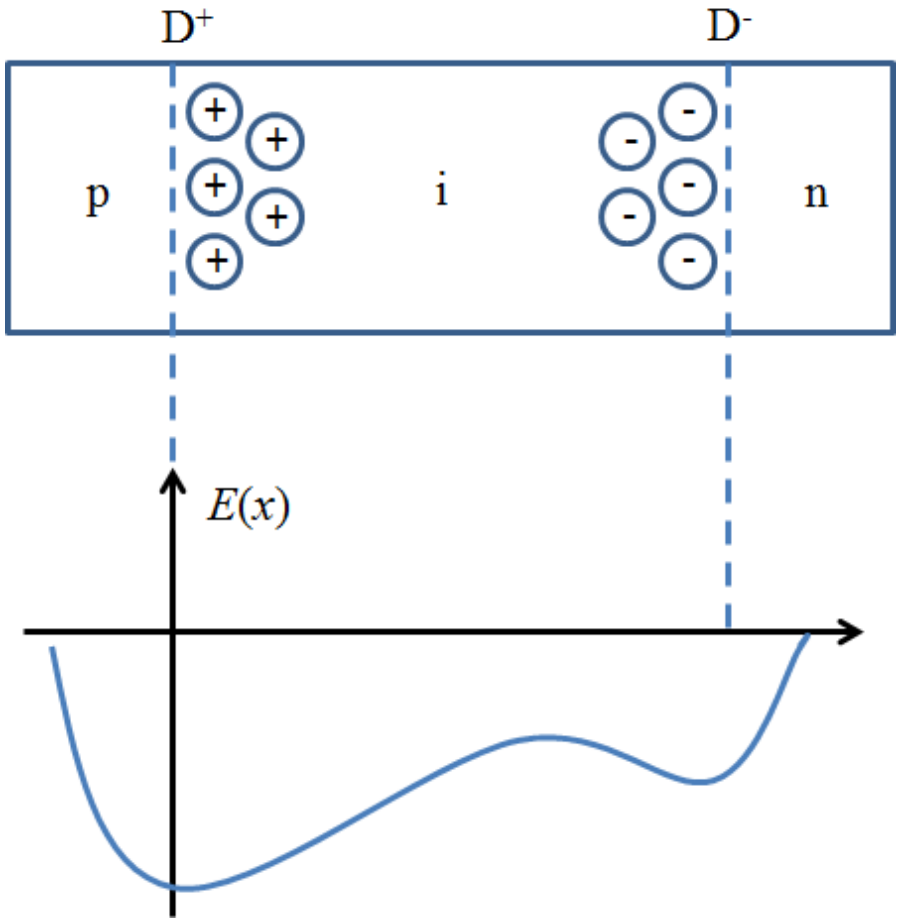

Figure 1.23. Representation of the electrical field $E(x)$ in the p-i-n layers of a thin film solar cell. The deformations of $E(x)$ are because of positively charged defects (mainly dangling bonds D^+) that exist between the p-i interface and negatively charged defects

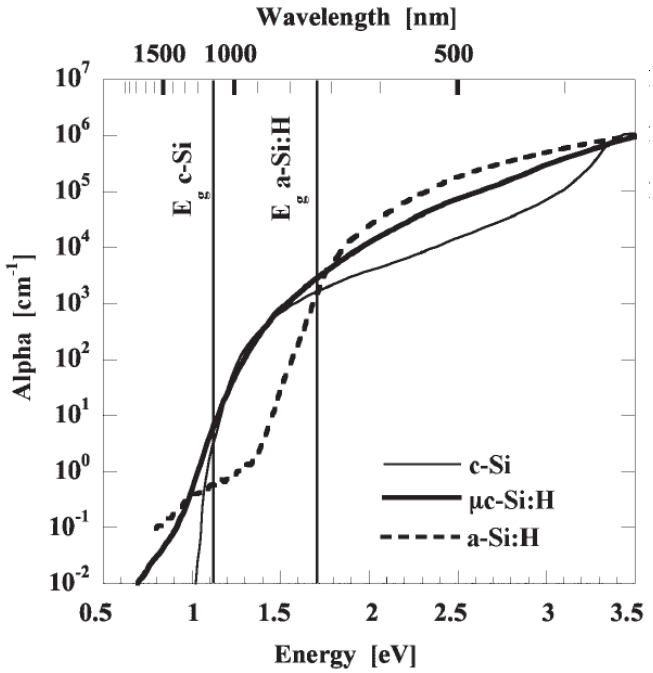

Figure 1.24. Absorption coefficient for c-Si, a-Si:H and µc-Si:H as a function of energy. Reproduced from [1.37] with permission of John Wiley and Sons and Copyright Clearance Center.

1.6.5.2 Transparent conductive oxide

Lateral conduction in the p and n-type layers of crystalline silicon solar cells does not represent an issue therefore, it is possible to collect carriers by using a thin grid of silver or aluminium to collect charges. In thin films, a small grid of metal contacts may be unable to collect carriers due to the high density of defects in amorphous silicon. Therefore, a contact covering the entire layer is required. This contact cannot be a metal because light would be reflected instead of reaching the intrinsic layer, thus a different approach is needed.

Transparent conductive oxides are used to avoid the high series resistances of amorphous silicon which do not offer a good lateral conductance for distances over 1 cm [1.38]. The most common TCO materials are tin oxide (SnO_2) and zinc oxide (ZnO) because they are economic to produce, abundant in nature and environmentally friendly. Indium-tin oxide is the traditional option however, it is the most expensive of the three because it requires indium which is scarce on Earth. The requirements for a good TCO are the next:

1) High conductivity, carrier mobility and transparency in the range of the solar spectrum.
2) Coupling of light with the absorber layer.
3) Texturized surface on both ends of the cell to scatter light.
4) Chemical stability when in contact to silicon.
5) Low cost and environmentally friendly.

In order to produce TCO layers with high conductivity, ZnO and SnO_2 are normally doped with aluminium and fluorine respectively, but gallium and boron can also be used. These dopants produce n-type materials with conductivities between 10^3 and $5x10^3$ $(\Omega cm)^{-1}$ and mobilities from 30 cm^2/Vs to 60 cm^2/Vs [1.39]. Unfortunately, a p-type TCO has not been successfully adapted to contact the a-Si:H p-layer and produce a good Ohmic contact yet.

It is compulsory for the band gap of a TCO to be wide because most of the spectrum needs to be able to get through it. For non-doped ZnO and SnO_2 the bandgaps are approximately 3.4 eV and 3.6 eV respectively [1.40].

1.6.5.3 Light management

Light management is an effective and promising approach to increase the efficiency of a solar cell. The objective is to produce trapping mechanisms to improve the absorption of light in the inner layers to have an effective use of the solar spectrum in the broadest range possible. A correct use of light management would result in an enhancement of the optical path length, which means that the distance a photon travels inside a solar cell before escaping would be increased, therefore thinner layers of silicon can be used to minimize costs, reduce degradation to light and reduce the time required for deposition of the cell. Some techniques used in light management are scattering at rough interfaces, as well as reflection at back contacts implemented by Morris [1.41]

Surface textured substrates are used in order to introduce rough interfaces. This is normally done by patterning structures on TCOs such as boron doped zinc oxide (BZO), aluminium doped zinc oxide (AZO) and fluorine doped tin oxide (FTO). Scattering at nano-particles relies on free electrons at the surface of metal nano-particles resonating when light of certain wavelength reaches them. For this purpose, silver is ideal due to its high surface plasmon resonance and low absorption. This concept has been applied by Santbergen with the introduction of silver nano-particles at different interfaces of a single junction a-Si:H solar cell [1.42]. The introduction of these nano-particles between the n-type silicon and AZO results in an increase by 5% in current when compared to a cell with non-textured interfaces, however this concept is still far from being optimized. Not only conductive nano-particles have been used for scattering purposes, also dielectric materials have attracted attention lately. An example of dielectric nano-particles used is white paint based on titanium dioxide (TiO_2) pigments dispersed in oil, which has been inserted in the TCO to function as a back reflector as an alternative to silver or aluminium as reported by Berger [1.43] and Lipovšek [1.44], further reducing the cost of the cells and achieving comparable scattering properties of a silver back reflector.

Additionally, a TCO can provide the solar cell with light trapping by scattering the light at the TCO-silicon interface. The refractive index n_s of a material is related to its dielectric constant ε_s as shown in Eq. 1.22, where the imaginary term k_s is related to the absorption coefficient of the material as shown in Eq. 1.23.

$$\sqrt{\varepsilon_s} = n_s - ik_s \tag{1.22}$$

$$\alpha = \frac{4\pi k_s}{\lambda} \tag{1.23}$$

Reflection and transmission of light at the interface of both materials are determined by the difference of their refractive indices. When light travels through two materials whose refractive index match each other, it can pass from one material to the other without reflection nor refraction. In order to have a better use of the light resource in the solar cell, the refractive index of each layer should increase in the same order as light goes through the layers until it

reaches its maximum value at the i-layer. This gradual variation of the refractive index is known as refractive index grading, and it allows to scatter the light and trap it inside the solar cell in order to increase absorption and produce more electron-hole pairs. Refraction of light through the layers can be seen in Fig. 1.22 and Fig. 1.25, whereas light trapping is shown in Fig. 1.25.

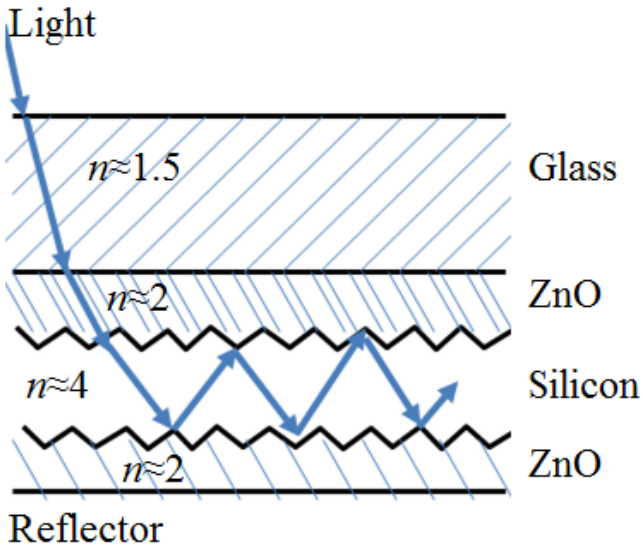

Figure 1.25. Effects of refractive index grading at the layers of the cell. Texturized TCO is used for the purpose of light trapping, preventing the reflected light to escape from the cell and increase its possibility to be absorbed by the i-layer.

To minimize losses caused by absorption or reflection at layers other than the absorber layers, it has been suggested to use wide bandgap semiconductors specially at the p-layer, this means, replacing the a-Si:H p-layer with bandgap of 1.72 eV with a material with more transmittance, such as a-SiC:H, whose bandgap can be varied from 1.8 eV to 3 eV depending on the carbon concentration. Finally, an effective use of the solar spectrum is achieved by optimization of bandgap of the different layers in the cell or by the fabrication of multiple junction solar cells designed to absorb different regions of the spectrum.

1.6.5.4 Multiple junction solar cells

The effect of LID can be reduced when thinner layers are used, however, as layer thickness is reduced, light absorbed by the cell also decreases. An approach to minimize SWE without sacrificing performance is by the use of multiple junction solar cells. Four different structures of thin film solar cells are shown in Fig. 1.26. Light absorption of the single junction cell can be improved by increasing the thickness of the intrinsic region however, there is a limit where the electric field implemented by the p-type and n-type silicon layers becomes weak due to the separation between them, complicating the separation of carriers. Furthermore, SWE is more evident in thicker layers. An improvement of the single junction cell is the double junction cell (same gap). For this case, two single junction devices with reduced intrinsic regions are connected in series. By doing this current obtained from the cell is slightly reduced however, the main advantage comes from a reduced SWE and a nearly double voltage under open circuit conditions. Finally, the stabilized efficiency is greater than for the single junction case.

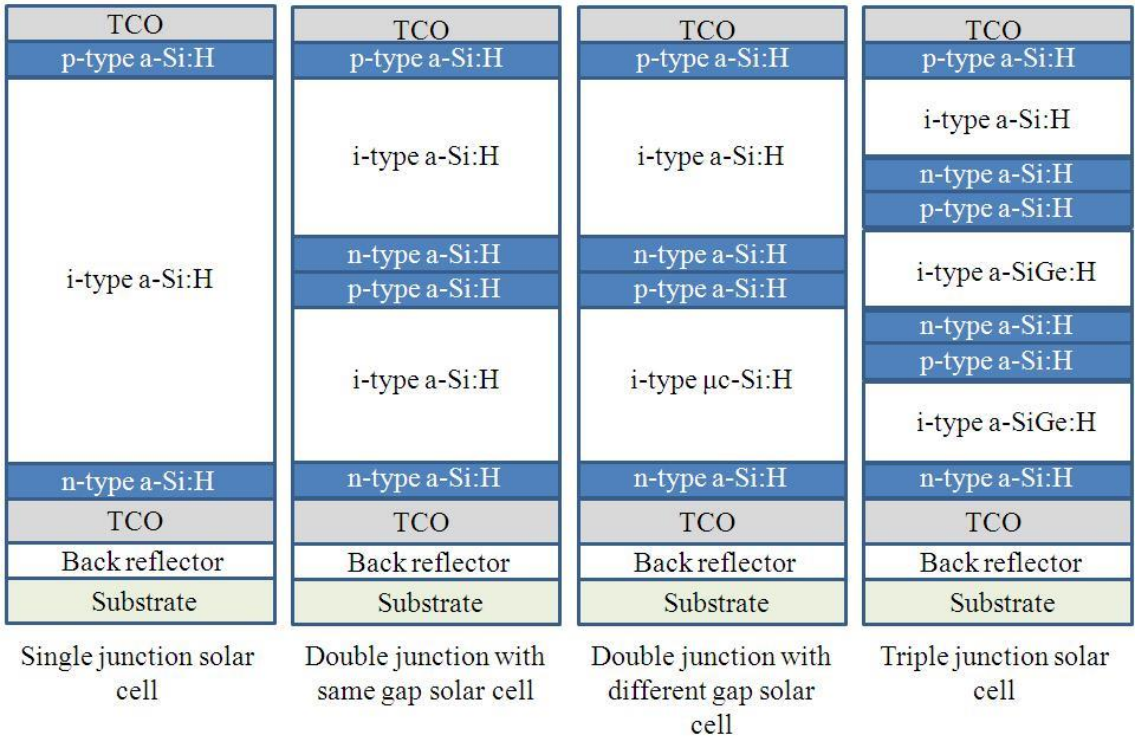

Figure 1.26. Diagram for multiple approaches used in thin film technologies. The introduction of multiple solar cells allows reduction in thickness of the layers to prevent LID while increasing the voltage output. The solar spectrum can be used more effectively when materials with different bandgaps are used to fabricate the structure.

The double junction solar cell can be further improved when different regions of the solar spectrum are utilised by the absorber layer, resulting in a more effective use of the many wavelengths. This can be done by building a tandem structure with absorber layers of different bandgaps. This is the case of the micromorph structure developed by Meier from the University of Neuchâtel, which is composed by a top cell made of a-Si:H and a bottom cell made of μc-Si:H [1.45]. This follows the principle pioneered by Okuda and Hamakawa, who used an a-Si:H cell stacked on a polycrystalline solar cell [1.46]. Another option for a bottom absorber layer is a-SiGe:H, since the introduction of germanium allows a reduction in bandgap of a-Si:H. Also, the use of a graded germanium profile facilitates charge transport by avoiding discontinuities in the energy bands [1.47]. In both cases, the bottom layer made of similar thickness as the top layer presents a reduced voltage but current through the cell is increased, allowing for an increase in efficiency. The top cell made of a-Si:H produces more power, but in order to keep the current at the level of the bottom cell, the a-Si:H section needs to be thicker. This causes light induced degradation in the amorphous section hence, the efficiency of the entire structure is reduced. A different concentration of Ge can be used in a third cell connected in series with the structure, this allows for an even better use of the solar spectrum. With the use of multiple junction solar cells, the efficiency of the complete structure can be increased beyond the theoretical limits of a single junction solar cell.

When multiple junction structures are fabricated, the first parameters to be considered are thickness and bandgap of the cells. The design process starts with the evaluation of the bottom cell and continues with the design of the top cell to produce approximately half the current of the bottom cell. A similar process can be used to design a triple junction cell. This time, the bottom cell is evaluated first and then the middle cell is designed to produce 2/3 the current of the bottom cell, whereas the top cell is designed to produce 1/3the current of the bottom cell [1.48].

The world record efficiency for micromorph solar cells is attributed to Matsui from AIST with a stabilized efficiency of 12.7% for an area of 1 cm^2 [1.49], whereas a stabilized efficiency of 12.2% has been achieved for a large area module of 1.1x1.3 m^2 [1.50]. The highest initial cell efficiency for a triple junction thin film silicon structure is 16.3%

demonstrated by United Solar Ovonic and NREL with an a-Si:H/a-SiGe:H/µc-Si:H structure [1.51], whereas the highest stabilized value of 13.4% corresponds to Ahn from LG Electronics with an a-Si:H/µc-Si:H/µc-Si:H structure [1.52].

Another technique used to improve efficiency of the cell is the introduction of a transparent interlayer between the top and bottom cells of a double junction structure in order to partially reflect some light back to the top layer. This is referred as internal light trapping (Fig. 1.27b). By reflecting light to the top cell it is possible to increase the current produced by it without the need to increase its thickness. This approach was developed by Yamamoto from Kaneka Corporation [1.53] and has been employed by Kaneka in the mass production of a-Si/µc-Si modules since 2008 [1.54]. Thin transparent layers of silicon oxide have also been used as interlayers for cases when excessively rough substrates are used, which can compromise the performance of the cell. This detrimental effect is attributed to an increase in shunts and weak diodes created when silicon gets in contact with the rough substrate [1.55, 1.56]. This resistive interlayer would act then, as an opposition to leakage currents.

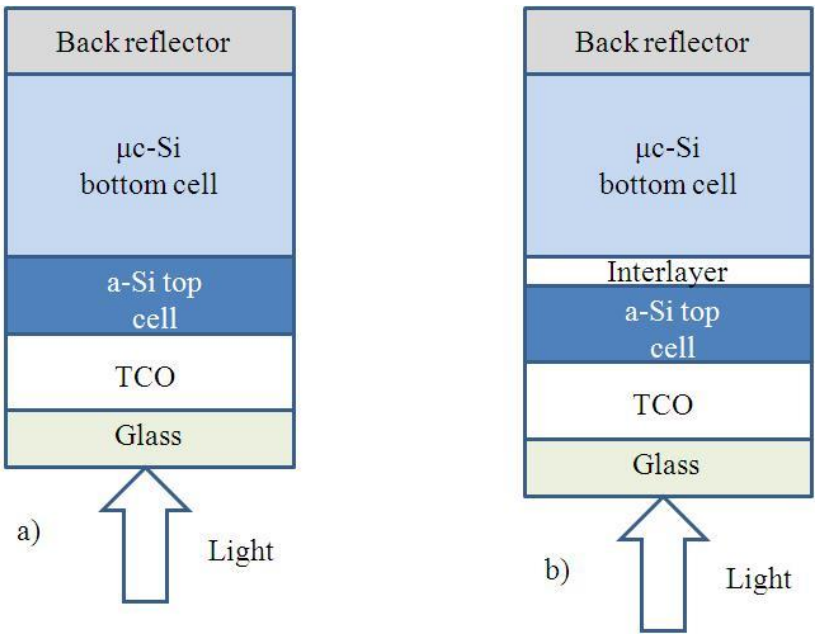

Figure 1.27. a) Normal approach for an a-SI:H/µc-Si:H tandem solar cell for an efficient use of solar spectrum. b) Introduction of an interlayer to produce internal light trapping, partially reflecting light back to the a-Si:H cell in order to increase the current of the top cell without increasing its thickness.

Recently, Isabella from Delft University has shown via optical simulations that a quadruple junction with structure a-SiO_X:H/a-SiGe:H/µc-Si:H/µc-SiGe:H has a potential to reach an efficiency of 19.8% [1.57]. Schüttauf from Neuchâtel argued that multiple challenging and optimistic assumptions were made by Isabella, and suggested the use of an a-Si:H/a-SiGe:H/µc-Si:H/µc-Si:H quadruple junction [1.53]. Although the experimental results of Schüttauf show only a stabilized efficiency of 10.1%, he and Meillaud from the same research group consider the potential of the quadruple structure and foresee stabilized efficiencies of 15% or even 16% in the future [1.59]. A quintuple junction thin film solar cell with a theoretical efficiency of 35% is also mentioned in the literature by Konagai [1.60]

1.6.6 HIT solar cell

A recent approach to a high efficiency solar cell is the heterojunction with intrinsic layer (HIT) cell developed by Sanyo [1.61]. This cell uses a mixture of crystalline and thin film materials shown in Fig. 1.28. The goals pursued by Sanyo with the use of the HIT structure are the improvements of efficiency and temperature coefficient, the reduction of material by the use of thinner layers and production of a bifacial module with a symmetrical structure (see Fig. 1.28) [1.62]. The use of this structure allows the cell to absorb light reaching from both faces of the cell, such as the direct sunlight, and the light reflected at the back from surfaces around module.

Layers of intrinsic a-Si:H are deposited on top and bottom of an n-type c-Si layer, which allows passivation of dangling bonds that may exist on the edges of crystalline materials. Then, a-Si:H(i) is followed by a-Si:H(p) and a-Si:H(n) layers. Both sides of the cell are contacted with a TCO to fulfil the light trapping function and to overcome the issue of the low mobility of carriers in a-Si:H [1.63].

The drawbacks of HIT cells come from the non-ideal contact with the TCO layers, which is the same issue that occurs in a-Si:H solar cells, as will be addressed in the rest of this thesis. Therefore, any improvement achieved in thin film solar cells contacts directly benefits HIT solar cells. This is of significant importance, since HIT solar cells are a

promising technology that has managed to achieve 25.6% efficiency on samples with an area of 143.7 cm^2 as demonstrated by Panasonic [1.64].

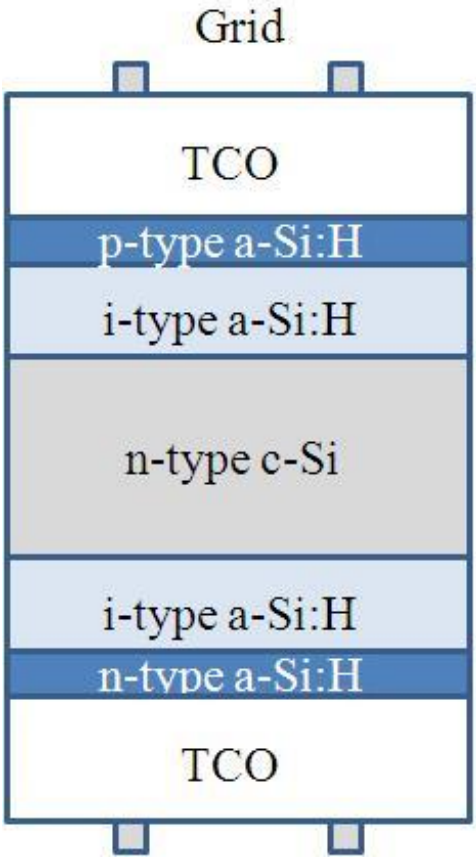

Figure 1.28. Bifacial structure of a HIT solar cell. The structure allows the absorption of light from both sides of the cell. A combination of crystalline and amorphous materials are used in this approach.

1.7 References in Chapter 1

[1.1] T. M. Razykov, C. S. Ferekides, D. Morel, E. Stefanakos, H. S. Ullal and H. M. Upadhyaya, "Solar photovoltaic electricity: Current status and future prospects," *Solar Energy*, vol. 85, no. 8, pp. 1580-1608, Aug. 2011.

[1.2] McKinsey & Company, "Pathways to a Low-Carbon Economy. Version 2 of the Global Greenhouse Gas Abatement Cost Curve," McKinsey & Company, 2009.

[1.3] B. Parida, S. Iniyan and R. Goic, "A review of solar photovoltaic technologies," *Renewable and Sustainable Energy Reviews*, vol. 15, no. 3, pp. 1625-1636, Apr. 2011.

[1.4] G. R. Timilsina, L. Kurdgelashvili and P. A. Narbel, "Solar energy: Markets, economics and policies," *Renewable and Sustainable Energy Reviews*, vol. 16, no. 1, pp. 449-465, Jan. 2012.

[1.5] J. Nelson, "The physics of solar cells," *Imperial College Press*, pp. 1, 2003.

[1.6] W. G. Adams, and R. E. Day, "The action of light on selenium", *Proceedings of the Royal Society (London)*, vol. A25, pp.113, 1877.

[1.7] D. M. Chapin, C. S. Fuller, and G. L. Pearson, "A new silicon p-n junction photocell for converting solar radiation into electrical power," *Journal of Applied* Physics, vol. 25, pp. 676, 1954.

[1.8] International Energy Agency, "2015 Snapshot of global photovoltaic markets," pp. 5, 2016.

[1.9] David Wood, "Optoelectronic semiconductor devices," Prentice Hall, International series in optoelectronics, pp. 33-59, 1994.

[1.10] Ben G, Streetman and Sanjay Banerjee. "Solid state electronic devices" Prentice Hall. Fifth edition. 61-62

[1.11] M. A. Green, K. Emery, Y. Hishikawa, W. Warta and E. D. Dunlop, "Solar cell efficiency tables (version 45)," *Progress in Photovoltaics: Research and Applications*, no. 23, pp. 1-9, 2014.

[1.12] W. Shockley, and H. J. Queisser, "Detailed balance limit of efficiency of p-n junction solar cells," *Journal of Applied Physics*, vol 32, no. 3, pp. 510-518, 1961

[1.13] First Solar Press Release, "First Solar builds the highest efficiency thin film PV cell on record," August 5, 2014. Available at http://investor.firstsolar.com/releasedetail.cfm?ReleaseID=864426. Accessed on 31/12/2016

[1.14] Shvydka, D., Gupta, A., Karpov, V.G., Compaan, A.D. "Mostly non-uniformity issues in thin-film PV," In: Proceedings of NCPV and Solar Program Review Meeting, Denver, USA, NREL/CD-520-33586, pp. 397–400, 2003

[1.15] S. K. Deb, "Thin-film solar cells: an overview," *National Renewable Energy Laboratory*, p. 375-379, 1996

[1.16] S. Wagner, "$CuInSe_2$/CdS heterojunction photovoltaic detectors," *Applied Physics Letters*, vol. 25, no. 8, p. 434, 1974.

[1.17] L. L. Kazmerski, F. R. White and G. K. Morgan, "Thin-film $CuInSe_2$/CdS heterojunction solar cells," *Applied Physics Letters*, vol. 29, no. 4, pp. 268, 1976.

[1.18] I. Repins, M. A. Contreras, B. Egaas, C. Dehart, J. Scharf and C. L. Perkins, "19.9 % efficient ZnO / CdS / $CuInGaSe_2$ Solar Cell with 81.2 % Fill Factor," *Progress in Photovoltaics: Research and Applications*, no 16, pp. 235-239, 2008.

[1.19] M. Osborne, "Hanergy's Solibro has 20.5% CIGS solar cell verified by NREL. http://www.pvtech.org/news/hanergys_solibro_has_20.5_cigs_solar_cell_verified_by_nrel Accessed on 31 August 2015.

[1.20] M. A. Green, "The Path to 25 % Silicon Solar Cell Efficiency: History of Silicon Cell Evolution," *Progress in Photovoltaics: Research and Applications*, pp. 183-189, 2009.

[1.21] M. A. Green. "Silicon solar cells: advanced principles and practice," Bridge Printery, Sydney (1995)

[1.22] O. Schultz, S. W. Glunz and G. P. Willeke, "Multicrystalline silicon solar cells exceeding 20% efficiency," *Progress in Photovoltaics: Research and Applications*, vol. 12, no. 7, pp. 553-558, Nov. 2004.

[1.23] W. Deng, D. Chen, Z. Xiong, P. J. Verlinden, J. Dong, F. Ye, H. Li, H. Zhu, M. Zhong, Y. Yang, Y. Chen, Z. Feng, and P. Altermatt, "20.8% PERC solar cell on 156 mm × 156 mm p-type multicrystalline silicon substrate," *Applied Physics Letters* ,vol. 6, no. 1, pp. 3-9, 2015.

[1.24] P. A. Basore, Simplified processing and improved efficiency of crystalline silicon on glass modules. In: 19th European Photovoltaic Solar Energy Conference, Paris, June, pp. 455–458, 2004

[1.25] D. C. Allan, and J. D. Joannopoulos, "Electronic structure of hydrogenated amorphous silicon," *Physical Review Letters*, vol. 44, no. 43, pp. 43, 1980.

[1.26] J. Meier, R. Flücкiger, H. Keppner, and A. Shah, "Complete microcrystalline p-i-n solar cell—Crystalline or amorphous cell behavior?," *Applied Physics Letters*, vol. 65, no. 7, p. 860, 1994.

[1.27] D. L. Staebler and C. R. Wronski, "Reversible conductivity changes in discharge-produced amorphous Si," *Applied Physics Letters*, vol. 31, no. 4, p. 292, 1977.

[1.28] M. A. Alam, S. Don, Y. Karthik, S. Mahapatra, D. Wang, and M. Frei, "Intrinsic reliability of amorphous silicon thin thin solar cells," *Solar Cells*, pp. 312-317, 2010.

[1.29] T. Yanagisawa, "Temperature dependence of light-induced degradation in a-Si solar cells," *Solar Cells, 22*. pp. 125-132, 1987.

[1.30] C. Radue and E. E. van Dyk, "Degradation analysis of thin film photovoltaic modules," *Physica B: Condensed Matter*, vol. 404, no. 22, pp. 4449-4451, Dec. 2009.

[1.31] W. Jackson, M. Stutzmann, and C. Tsai, "Effects of dopant and impurity incorporation on metastable light-induced defect formation," *Solar Cells*, vol. 21, no. 1-4, pp. 431-438, Jun. 1987.

[1.32] H. Liu and M. Xu, "The Staebler-Wronski effect in microcrystalline silicon films," *Solid State Physics*, vol. 58, no. 9, pp. 601-603, 1986.

[1.33] T. Matsui, H. Sai, T. Suezaki, M. Matsumoto, K. Saito, I. Yoshida, and M. Kondo, "Development of highly stable and efficient amorphous silicon based solar cells," Proc. 28th European Photovoltaic Solar Energy Conference, pp. 2213–2217, 2013.

[1.34] H. Sai, T. Matsui, K. Matsubara, M. Kondo, I. Yoshida, "11.0% Efficient Thin-Film Microcrystalline Silicon Solar Cells with Honeycomb Textured Substrates," *IEEE Journal of Photovoltaics*, vol. 4, no. 6, pp 1349-1353, 2014.

[1.35] D. E. Carlson, and C. R. Wronski, "Amorphous silicon solar cell," *Applied Physics Letters*, vol. 28, no. 11, pp. 671-673, 1976.

[1.36] W. E. Spear, and P. G. L. Comber, "Substitutional doping of amorphous silicon," *Solid State Communications*, vol. 17, pp 1193–1196, 1975.

[1.37] A. V. Shah et al., "Thin-film silicon solar cell technology," *Progress in Photovoltaics: Research and Applications*, vol. 12, no. 23, pp. 113-142, Mar. 2004.

[1.38] D.E. Carlson, C.R.Wronski, Amorphous Silicon, Topics in applied physics, vol. 36, Springer, Berlin, 1979, p. 287.

[1.39] W. Beyer, J. Hupkes, and H. Stiebig, "Transparent conducting oxide films for thin film silicon photovoltaics," *Thin Solid Films*, vol. 516, no. 2-4, pp. 147-154, Dec. 2007.

[1.40] K. Ellmer, "Resistivity of polycrystalline zinc oxide films: current status and physical limit," *Journal of Physics D: Applied Physics*, vol. 3097, pp. 3097-3108, 2001.

[1.41] J. Morris, R. R. Arya, J. G. O'Dowd, and S. Wiedeman, "Absorption enhancement in hydrogenated amorphous silicon (a-Si:H) based solar cells," *Journal of Applied Physics*, vol. 67, pp. 1079–1087, 1990.

[1.42] R. Santbergen, R. Liang and M. Zeman, "A-Si:H solar cells with embedded silver nanoparticles," *Science*, pp. 748-753, 2010.

[1.43] O. Berger, D. Inns, and A. G. Aberle, "Commercial white paint as back surface reflector for thin-film solar cells," *Solar Energy Materials and Solar Cells*, vol. 91, no. 13, pp. 1215-1221, Aug. 2007.

[1.44] B. Lipovšek, J. Krč, O. Isabella, M. Zeman, and M. Topič, "Analysis of thin-film silicon solar cells with white paint back reflectors," *Physica Status Solidi C*, vol. 7, no. 3-4, pp. 1041-1044, Jan. 2010.

[1.45] J. Meier, S. Dubail, R. Flückiger, D. Fischer, H. Keppner, and A. Shah, Proc. of the 1st World Conference on Photovoltaic Energy Conversion, Waikoloa, HI, pp. 409, 1994.

[1.46] K. Okuda, H. Okamoto and Y. Hamakawa, "Amorphous Si/Polycrystalline Si Stacked Solar Cell Having More Than 12% Conversion Efficiency," *Japanese Journal of Applied Physics*, vol. 22, part 2, no. 11, 1983.

[1.47] S. Guha, J. Yang, A. Pawlikiewicz, T. Glatfelter, R. Ross, S. R. Ovshinsky, "Band-gap profiling for improving the efficiency of amorphous silicon alloy solar cells," *Applied Physics Letters*, vol. 54, pp. 2330, 1989.

[1.48] D. Fischer, S. Dubail, J. A. Anna Selvan, N. P. Vaucher, R. Platz, Ch. Hof, U. Kroll, J. Meier, P. Torres, H. Keppner, N. Wyrsch, M. Goetz, A. Shah and K. Ufert, "The "micromorph" solar cell: extending a-Si:H technology towards thin film crystalline silicon,"

Conference Record of the 25th IEEE Photovoltaic Specialists Conference, Washington DC, pp. 1053 – 1056, May 1996.

[1.49] T. Matsui, H. Sai, K. Saito, M. Kondo, "High-efficiency thin-film silicon solar cells with improved light soaking stability," *Progress in Photovoltaics: Research and Applications*, vol. 21, pp. 1363, 2013.

[1.50] TEL Solar Press Release, July 9, 2014.

[1.51] B. Yan, G. Yue, L. Sivec, J. Yang, S. Guha, and C. S. Jiang, "Innovative dual function nc-SiO_X:H layer leading to a >16% efficient multi-junction thin-film silicon solar cell," *Applied Physics Letters*, vol. 99, pp. 113512, 2011.

[1.52] S. W. Ahn, S. E. Lee, and H. M. Lee, "Toward commercialization of triple-junction thin- film silicon solar panel with >12% efficiency," Proc. of 27th European Photovoltaic Solar Energy Conference, Frankfurt, September 2012.

[1.53] K. Yamamoto, A. Nakajima, M. Yoshimi, T. Sawada, S. Fukuda, T. Suezaki, M. Ichikawa, Y. Koi, M. Goto, H. Tanaka, T. Sasaki and Y. Tawada, Proc. of 3rd World Conf. Photovoltaic Solar Energy Conversion, paper S2OB903 (2003)

[1.54] T. Sasaki, N. Kadota, M. Gotoh, K. Shimizu, and T. Takahashi, "Fabrication technology for thin film silicon hybrid solar cells and modules," Proc. of the *35th IEEE Photovoltaic Specialists Conference*, pp. 1134-1140, Honolulu, HI, 2010.

[1.55] J. Yang, A. Banerjee and S. Guha, "Amorphous silicon based photovoltaics—from earth to the 'final frontier'," *Solar Energy Materials and Solar Cells*, vol. 78, no. 1-4, pp. 597-612, Jul. 2003.

[1.56] P. Buehlmann et al., "In situ silicon oxide based intermediate reflector for thin-film silicon micromorph solar cells," *Applied Physics Letters*, vol. 91, no. 14, p. 143505, 2007.

[1.57] O. Isabella, A. Smets, and M. Zeman, "Thin-film silicon-based quadruple junction solar cells approaching 20% conversion efficiency," *Solar Energy Materials and Solar Cells*, vol. 129, pp. 82-89, 2014.

[1.58] J. W. Schüttauf, B. Niesen, L. Löfgren, M. Bonnet-Eymard, M. Stuckelberger, S. Hänni, M. Boccard, G. Bugnon, M. Despeisse, F. J. Haug, F. Meillaud, and C. Ballif, "Amorphous silicon–germanium for triple and quadruple junction thin-film silicon based solar cells," *Solar Energy Materials and Solar Cells*, vol. 133, pp. 163-169, 2014.

[1.59] F. Meillaud, M. Boccard, G. Bugnon, M. Despeisse, S. Hänni, F.J. Haug, J. Persoz, J.W. Schüttauf, M. Stuckelberger, and C. Ballif, "Recent advances and remaining challenges in thin-film silicon photovoltaic technology," *Materials Today*, vol. 18, issue 7, pp. 378-384, 2015.

[1.60] M. Konagai, "Present status and future prospects of silicon thin-film solar cells," *Japanese Journal of Applied Physics*, vol. 50, pp. 030001, 2011.

[1.61] M. Taguchi, M. Tanaka, T. Matsuyama, T. Matsuoka, S. Tsuda, S. Nakano, Y. Kishi, and Y. Kuwano, "Improvement of the conversion efficiency of polycrystalline silicon thin film solar cell," *Tech. Digest 5th International Photovoltaic Science and Engineering Conference*, pp. 689-692, Kyoto, Japan, 1990.

[1.62] T. Mishima, M. Taguchi, H. Sakata, and E. Maruyama, "Development status of high-efficiency HIT solar cells," *Solar Energy Materials and Solar Cells*, vol. 95, no. 1, pp. 18-21, Jan. 2011.

[1.63] M. A. Green, "Crystalline and thin-film silicon solar cells: state of the art and future potential," *Solar Energy*, vol. 74, pp. 181-192, 2003.

[1.64] Panasonic Press Release, 10 April 2014. Panasonic HIT® Solar Cell Achieves World's Highest Energy Conversion Efficiency of 25.6% at Research Level Available at http://news.panasonic.com/global/stories/2014/26881.html. Accessed on September 1st, 2015.

Disclaimer notice for Fig. 1.14 [Available at http://www.nrel.gov/disclaimer.html, accessed on July 2016]

DEMAND, INCLUDING REASONABLE ATTORNEYS' FEES, RELATED TO USER'S USE OF THE DATA. THE DATA ARE PROVIDED BY DOE/NREL/ALLIANCE "AS IS," AND ANY EXPRESS OR IMPLIED WARRANTIES, INCLUDING BUT NOT LIMITED TO THE IMPLIED WARRANTIES OF MERCHANTABILITY AND FITNESS FOR A PARTICULAR PURPOSE ARE DISCLAIMED. IN NO EVENT SHALL DOE/NREL/ALLIANCE BE LIABLE FOR ANY SPECIAL, INDIRECT OR CONSEQUENTIAL DAMAGES OR ANY DAMAGES WHATSOEVER, INCLUDING BUT NOT LIMITED TO CLAIMS ASSOCIATED WITH THE LOSS OF DATA OR PROFITS, THAT MAY RESULT FROM AN ACTION IN CONTRACT, NEGLIGENCE OR OTHER TORTIOUS CLAIM THAT ARISES OUT OF OR IN CONNECTION WITH THE ACCESS, USE OR PERFORMANCE OF THE DATA.

Chapter 2:
Electrical and optical characterization of solar cells

Methods of electrical and optical characterization of solar cells are described in this chapter. The limitations of conventional solar cell circuit models are discussed for the case of a-Si:H technologies. Also, a more accurate and precise methodology for the extraction of modelling parameters from experimental measurements is presented.

This chapter presents the conventional parameters and measurement standards used to evaluate the performance of a solar cell, along with their techniques of extraction. Many characterization techniques are used at present for research and manufacturing purposes. Measurements such as current density of the cell as a function of applied voltage (*J*-*V*) for different light intensities, or capacitance as a function of frequency or voltage can be used to evaluate solar cells. Other tests examine the impact of wavelength on the efficiency. The common problems faced during the extraction procedure are analysed and a methodology to improve the accuracy of the parameters is presented.

2.1 Standard spectra for characterization of solar cells

The photovoltaic industry in cooperation with the American Society for Testing and Materials (ASTM) have developed the ASTM-G173-03 standard which defines two different solar spectral irradiance distributions for terrestrial applications [2.1]. The purpose of their creation is to allow the evaluation and comparison of photovoltaic devices from different manufacturers.

One standard is the AM1.5 (air mass) Global, which has been designed specifically for the characterization of flat cells and modules. It has an integrated power of 1000 W/m^2. It includes the spectral radiation from the Sun, the light that is diffused by the sky, and the diffuse light reflected from the ground, that reaches a surface in the northern hemisphere facing the south with an inclination of 37º from the horizontal., when the angle of the sunbeams with respect to the normal of the surface (zenith) is approximately θ=48º. The other standard is the AM1.5 Direct, which has an integrated power of 900 W/m^2 and has been designed for devices that include a solar concentrator and tracking system. This standard represents the direct component of the light that reaches the illuminated surface and excludes the light scattered by the sky and reflected by the ground. All of the solar cells mentioned in this thesis are characterized using the AM1.5 Global Standard.

For both standards, the term AM indicates the mass of air that the light needs to travel in order to reach the surface of the device to be characterized. The term AM can take different

values depending on the geographical position and time of measurement, and it is a function of the zenith angle as expressed in Eq. 2.1. Additionally, the standard ASTME E490, with a value of AM0 and an integrated power of 1366 W/m^2 represents extra-terrestrial radiation (ETR) or solar spectrum at the top of the atmosphere, used to characterize photovoltaic devices for space applications such as satellites [2.2]. Fig. 2.1 shows the points of measurement for the different standards, and Fig. 2.2 shows the spectral irradiance as a function of wavelength for the ETR and AM1.5 standards. The data required to plot Fig. 2.2 is freely obtained from the NREL internet site [2.3].

$$\mathrm{AM} = \frac{1}{cos(\theta)} \tag{2.1}$$

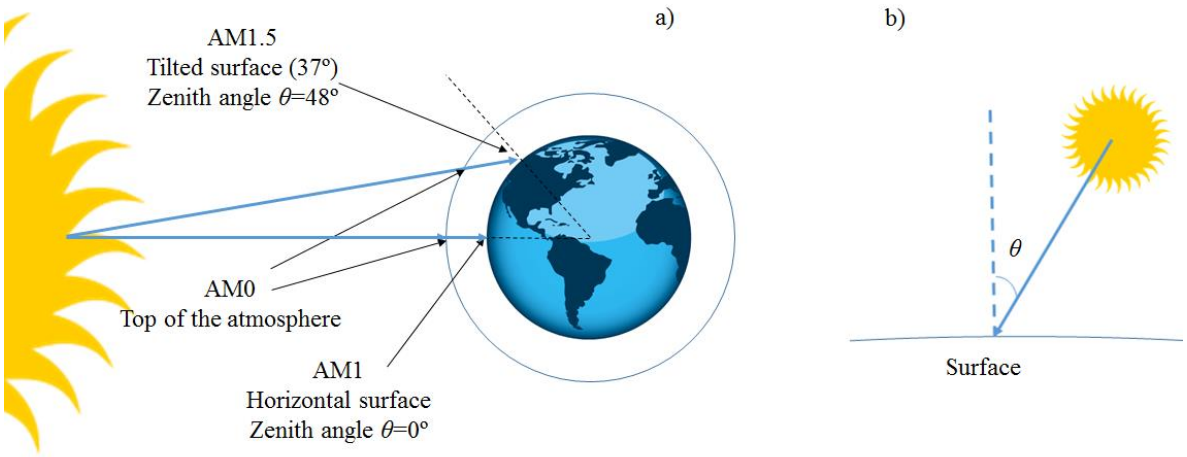

Figure 2.1. a) The diagram shows the positions where each standard is characterized. b) Definition of the zenith angle.

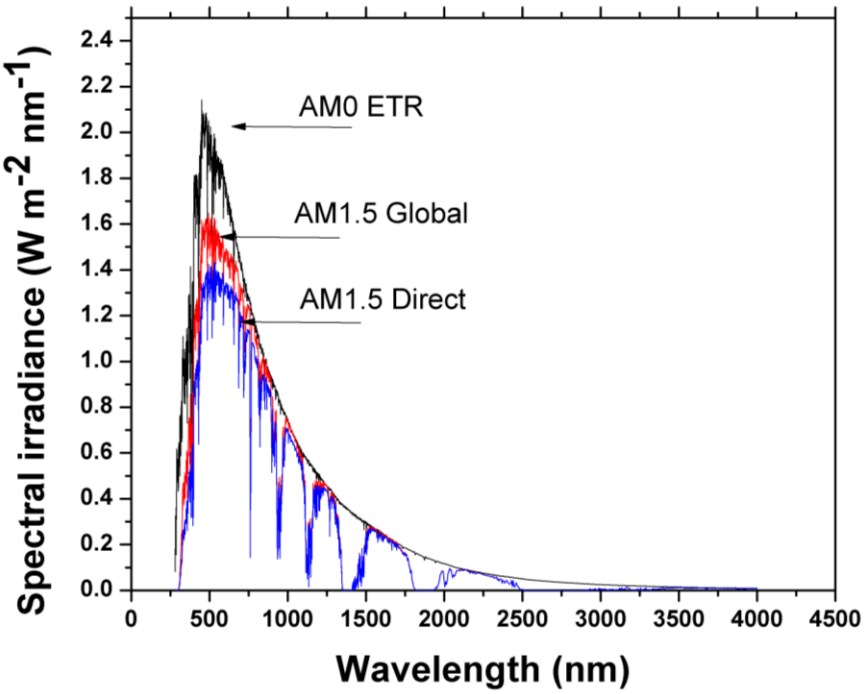

Figure 2.2. Typical illumination standards for the characterization of photovoltaic devices. Data freely at http://rredc.nrel.gov/solar/spectra/am1.5/ASTMG173/ASTMG173.html. Last time accessed on July 2016. Disclaimer notice can be read on page 75.

2.2 *J-V* measurements

The most common electrical test performed in solar cells is the measurement of current density under illumination as a function of an applied voltage. Fig. 2.3 shows some of the electrical parameters that can be obtained from the *J-V* curve of an illuminated solar cell. These include short circuit current density (J_{SC}), which represents the current measured when V=0, and open circuit voltage (V_{OC}), which represent the value of voltage when I=0. The maximum power point (P_{MAX}) is the maximum product of current (J_{MAX}) and voltage (V_{MAX}), and is located at the knee of the curve.

The fill factor (*FF*) indicates how much the characteristics of a solar cell differ from ideality. It is calculated via Eq. 2.2.

$$FF = \frac{I_{MAX}V_{MAX}}{I_{sc}V_{oc}} \quad (2.2)$$

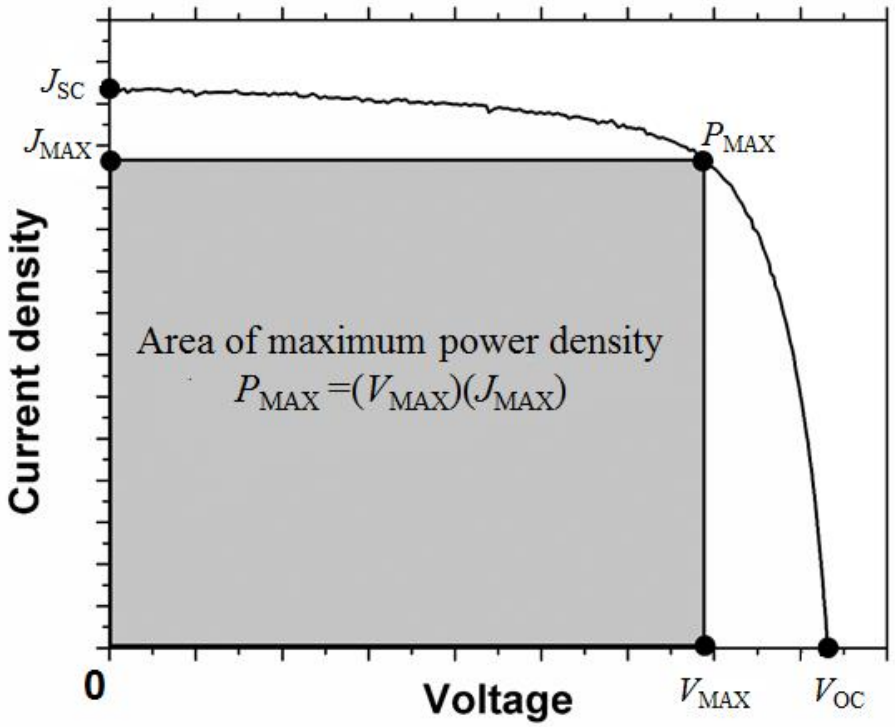

Figure 2.3. Current as a function of voltage for an illuminated solar cell indicating the most common parameters to describe the performance of a device.

An ideal solar cell should have a *FF*=1 (100%), however the effects of parasitic series and shunt resistances and other non idealities can reduce this quantity. Finally, the efficiency (η), is calculated as the ratio of the maximum power output of the cell by the input power received, as represented in Eq. 2.3.

$$\eta = \frac{P_{MAX}}{P_{in}} \tag{2.3}$$

2.3 Equivalent electronic circuit of a solar cell

Equivalent circuit modelling is a useful procedure to understand the working principles of any device by separating it into simpler electronic components such as resistors, capacitors, diodes or others. A model can also be used as a feedback tool in order to identify the elements that require further optimization or those that suffer degradation after prolonged use.

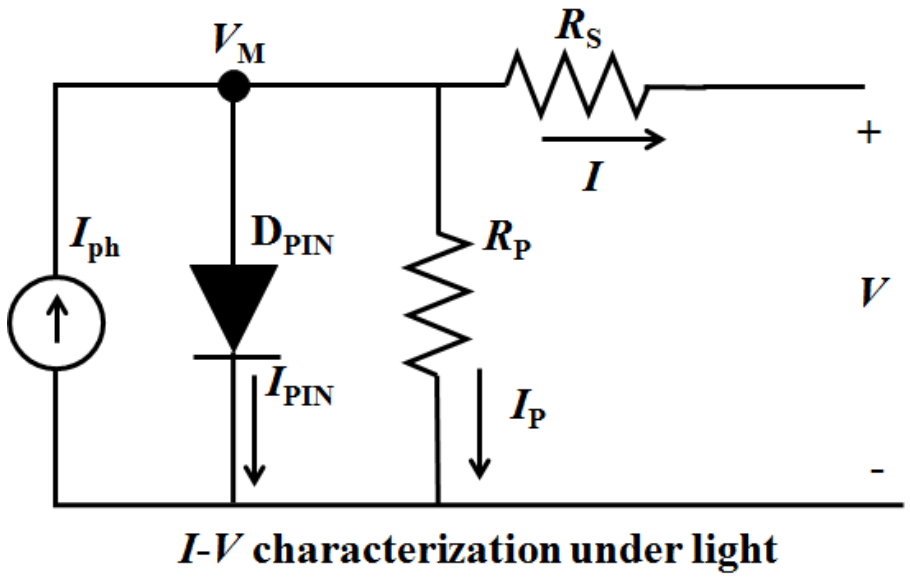

Figure 2.4. Simplest equivalent circuit for a solar cell where I_{ph} is the photocurrent produced when the device is illuminated, I_{PIN} and I_P represent currents that are deviated from the load through a diode and shunt resistance respectively, and I is the current received by the load.

For a thin film solar cell, absorption of photons in the intrinsic region causes the release of electron–hole pairs, then the electric field introduced by the p-type and n-type-doped layers causes these charges to separate from each other and flow into opposite directions through an external circuit. This behaviour can be represented as a current source connected in parallel with a diode, whose parameters such as saturation current I_O, ideality factor m of the main junction, and temperature T are the most relevant to define the J–V characteristic of the solar cell. A simple-circuit can be further improved by considering the series resistance R_S and the shunt resistance R_P as shown in Fig. 2.4. Here, R_S represents, the resistance of the semiconductor, the contact resistance between the semiconductor and conductor, and the resistance of the contacts such as cell metallization, interconnection bus-bars or TCO layers, whereas R_P represents parallel high conductivity paths that exist through the solar cell or at the edges, [2.4]. These shunts can be a consequence of damage to the crystal and impurities existent near the junction, allowing for shunt current I_P. The shunt resistance deviates the total photocurrent from the load with detrimental effect on the performance [2.5].

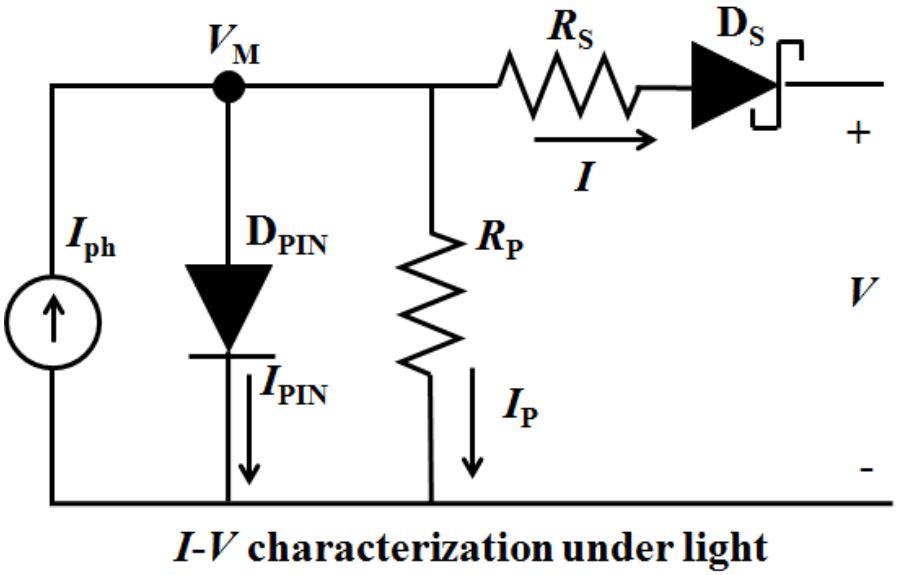

Figure 2.5. Model for a thin film silicon solar cell considering a non-ideal Schottky contact.

Ideally, R_S should be equal to zero whereas R_P should tend to infinity in order to maximize the current delivered to the external load. Similarly, the current I_{PIN} flowing through the diode is meant to be as low as possible. This could sound contradictory for such an essential element of the solar cell however, at a circuit level, the diode D_{PIN} represents a deviation of current to the load, which is caused due to recombination in the main junction. Details of the recombination models used in this research are presented in section 4.1.2. The effects of photocurrent, diode recombination and parasitic resistances are expressed in Eq. 2.4.

$$I = I_{ph} - I_0 \left[e^{\left(\frac{q(V+IR_S)}{mkT}\right)} - 1 \right] - \frac{V+IR_S}{R_P} \qquad (2.4)$$

I_0 in Eq. 2.4 is an indication of the junction quality, and as its value increases, there is an expected decrease in the quality of the junction associated with a degradation of cell performance, due to an increased recombination current. An increase of saturation current is attributed to an increase in the defect state density [2.6, 2.7]. The ideality factor *m*, indicates the quality of the main diode, the higher the value of *m*, the poorer the performance that can be expected due to higher recombination. The value of *m* is evaluated from the *J-V* curve of

the solar cell measured in the dark and is expected to exist in the range $1<m<2$. However, values of $m>2$ are commonly observed, especially in amorphous materials due to the tunnelling effects at the main junction, or due to low values of R_P that cause an abnormal increase of current in the low bias region [2.8, 2.9], which modifies the *J-V* curve and therefore compromises the evaluation of *m*, as will be explained in section 2.3. Similarly, a large value of R_S decreases the current measured in the dark at a high bias, which can also lead to values of *m* larger than 2.

An improperly fabricated contact to the doped layers represents a Schottky diode D_S in series with the common solar cell model as shown in Fig. 2.5. As a consequence, there is a drop of voltage V_{DS} across the Schottky diode that affects mainly the *FF* and the V_{OC}. The non-ideal existence of a Schottky contact needs to be considered in the equivalent circuit model therefore, Eq. 2.4 is extended to give Eq. 2.5.

$$I = I_{ph} - I_0\left[e^{\left(\frac{q(V+IR_S+V_{DS})}{mkT}\right)} - 1\right] - \frac{V+IR_S+V_{DS}}{R_P} \tag{2.5}$$

Fig. 2.5 shows that the current flowing to the load is the same as the current flowing through the Schottky diode, which can be expressed by Eq. 2.6, where q is the elementary charge, k the Boltzmann constant and I_{SS} and *n* represent the saturation current and ideality factor of the Schottky diode respectively. I_{SS} is expressed by Eq. 2.7 with *A* being the area of the device, A* the Richardson constant which equals 32 $Acm^{-2}K^{-2}$ for p-type silicon and 112 $Acm^{-2}K^{-2}$ for n-type silicon and Φ_{bp} the Schottky barrier height at the TCO/p-type silicon interface.

$$I = I_{DS} = I_{SS}\left[\exp\left(\frac{qV_{DS}}{nkT}\right) - 1\right] \tag{2.6}$$

$$I_{SS} = AA^*T^2\exp\left(\frac{-q\Phi_{bp}}{nkT}\right) \tag{2.7}$$

Although the saturation current I_0 of the main junction diode should be as small as possible to avoid deviation of photocurrent to the load, the saturation current I_{SS} of the Schottky diode should be high to reduce V_{DS}. A similar situation occurs with the ideality factors of the diodes, where the main junction requires a small value of m, whereas an interface with a Schottky barrier such as ZnO/a-Si:H(p) should be designed to present an ideality factor as high as possible in order to reduce V_{DS}. More details about the Schottky barrier are explained in chapter 4, 5 and 6.

2.4 Methodology for extraction of equivalent circuit parameters

There is no standard procedure to extract the parameters of the equivalent electronic circuit, given the influence of temperature and level of illumination. Furthermore, there is the possibility of an element affecting the performance of the solar cell in such way that it hides the effects of other elements. Here, evaluation of R_S is considered to be the most critical step for extraction of the subsequent parameters, since R_S can affect the performance of the cell in terms of P_{MAX} and FF, and also complicate the extraction of the cell intrinsic parameters such as m and I_O. Only the properly extracted value of R_S should be used to correct the dark I-V curve in order to continue the extraction of other parameters. However, a question that arises when extracting a value for R_S is, what are the values of bias, temperature or illumination intensity that should be used for the extraction?

A possible technique to evaluate R_S is to measure an I-V curve at two or more light intensities [2.6]. Then, a slope of R_S should be obtained by connecting multiple points near the knee of the different curves as shown in Fig. 2.6. The intensity of the light can be adjusted using a lamp with variable intensity, with the adaptation of neutral filters or by modifying the distance between the sample and the lamp. However, a problem with this technique is that the points selected from each I-V can lead to misleading values of R_S if they are not chosen carefully. Also, since the evaluated points are close to the knee of the curve, it assumes that the FF of the cell does not vary as a function of light intensity, which complicates the implementation of this particular technique to a-Si:H solar cells, since their FF can be modified by other effects, such as interface recombination. As an example, Fig.

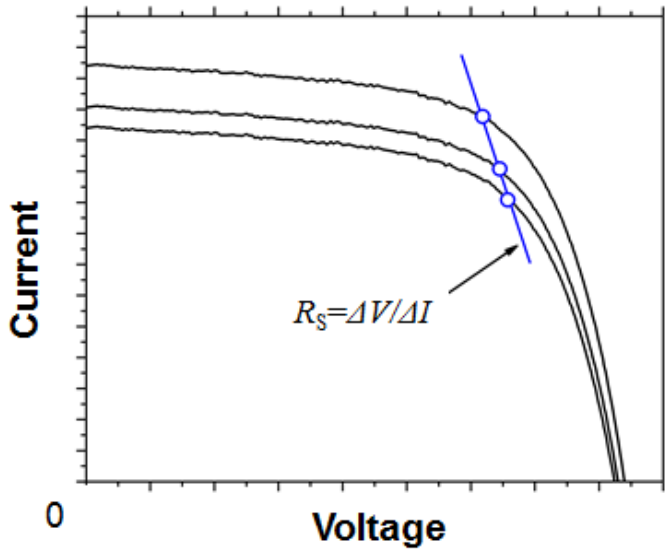

Figure 2.6. Common method employed to calculate the series resistance of a solar cell using *I-V* curves at illuminations of different intensity.

2.7 shows an illuminated solar cell *I-V* curve that has been shifted to start at the same current level (*I*=0) as its respective dark *I-V* curve. It is seen that the illuminated *I-V* is not obtained just by adding the photocurrent term to the dark *I-V*. Instead, a change in exponential shape is observed, which leads to changes in *FF* depending on the illumination level and hence, to a miscalculation of R_S.

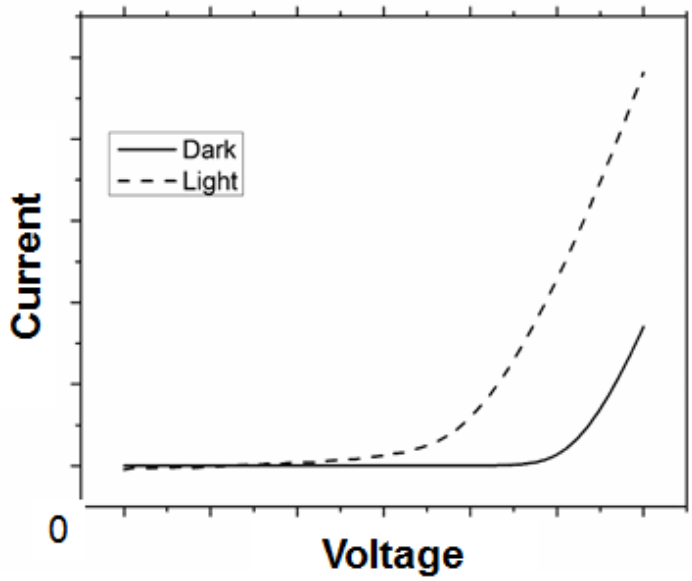

Figure 2.7. A comparison of dark and shifted illuminated *I-V* curves.

In this thesis, a novel method is used to evaluate R_S in order to calculate the rest of the parameters of the solar cell. Since R_S is an intrinsic parameter of the solar cell, it should be evaluated via electrical characterization of the cell without the intervention of external influences such as light or heat, which can have an impact on the measurements. The initial step of the process is to calculate an initial approximation of R_S. This is obtained from the slope of the high voltage region of the dark *I-V* curve (Eq. 2.8), where recombination at the main diode element saturates and the current measured becomes linear in a logarithmic plot with respect to the applied voltage. Then, the calculated value of R_S is used to build a plot of $\ln|I|$ vs V_M as shown in Fig. 2.8, where $V_M=V-IR_S$. Ideally, this should produce a plot where $\ln|I|$ grows linearly as a function of V_M. If $\ln|I|$ shows a bending in the high voltage region, the value of R_S needs to be increased or decreased until the $\ln|I|$-V_M is reconstructed in a way that the bending of the curve disappears. The process to find the final value of R_S can be done empirically or by an automated fitting procedure such as linear regression. Here, the $\ln|I|$-V_M curve was plotted using LabVIEW while the value of R_S was varied in real time until the $\ln|I|$-V_M curve was visually linear in the high voltage region.

$$\frac{1}{R_i} = \frac{dI}{dV} \tag{2.8}$$

Similarly, the value of R_P can also be estimated from the *I-V* in the dark using Eq. 2.8 however, it should be evaluated for values of $V \leq 0$ V. The effect of R_P on the illuminated *I-V* curve is barely relevant when $R_P > 500\ \Omega$. Usually, low values of R_P are attributed to a low quality manufacturing process rather than design issues. In this work, all of the solar cells showed values of $R_P > 800\ \Omega$ therefore, a detailed study of R_P is not as relevant as a correct evaluation of R_S.

As an example, Fig. 2.8 shows a dark $\ln|I|$-*V* curve corrected with three different values of R_S. If the extracted value of R_S is too low or not extracted at all, the corrected $\ln|I|$-*V* curve bends downwards in the high voltage regime. In the opposite case of an overestimated value of R_S, the dark $\ln|I|$-*V* curve bends upwards. Only the correct value of R_S is able to correct the dark $\ln|I|$-*V* in a way that $\ln|I|$ increases linearly with V_M (no bending), which means that the effect of R_S is separated from the main junction diode. The equivalent

circuit of the solar cell characterized in the dark is also shown in Fig. 2.8. It is observed that the element D_S is not included in the equivalent circuit shown. This is because the Schottky junction affects the *I-V* curve only at high intensities of light, as demonstrated by Bivour and Ritzau [2.10, 2.11]. They measured the V_{OC} of HIT solar cells as a function of light intensity and found that V_{OC} increases with light, and then decreases as the light intensity keeps increasing, which they attributed to an increased photocurrent of the Schottky diode at high illumination. More details are provided in chapter 5.

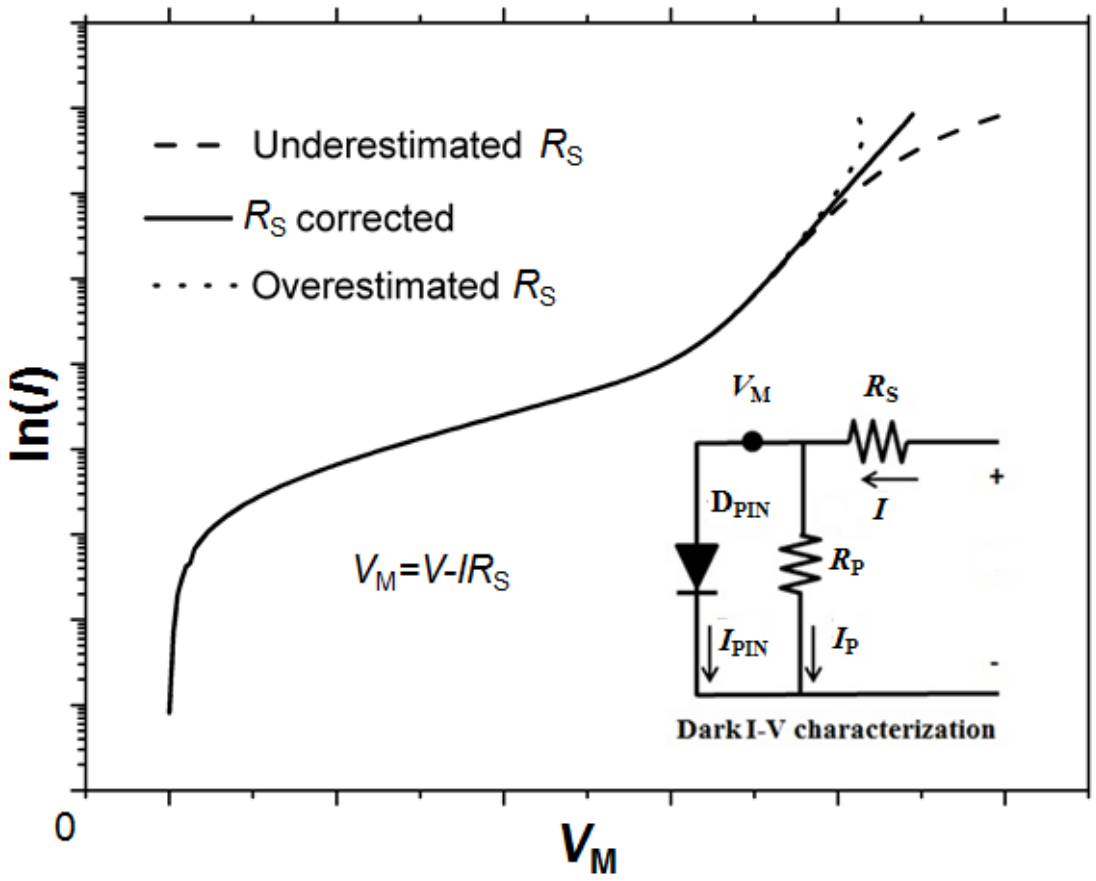

Figure 2.8. Correction of R_S in the dark *I-V* curve and equivalent circuit of the solar cell when characterized in the dark. The corrected value of R_S should not produce a bending of ln|*I*| for high values of V_M.

The main diode parameters *m* and I_0 can be evaluated once the ln|*I*|-V_M curve is corrected with a value of R_S that does not produce a bending of the curve in the high voltage

region. This is done by extrapolating the linear region of the $\ln|I|$-V_M curve, and calculating m according to Eq. 2.9, where q is the elementary charge, k the Boltzmann constant and T the temperature in Kelvin. Finally, I_O is evaluated from the intercept of the extrapolated region when V=0. The extraction of the main diode parameters is shown in Fig. 2.9. An inaccurate correction of R_S can lead to the inaccurate values of the main diode. Also, at this moment is possible to ignore the effects of the Schottky diode, since in reverse bias it behaves as a leaky diode.

$$m = \frac{\mathrm{q}}{\mathrm{k}T}\frac{dV}{dln(I)} \tag{2.9}$$

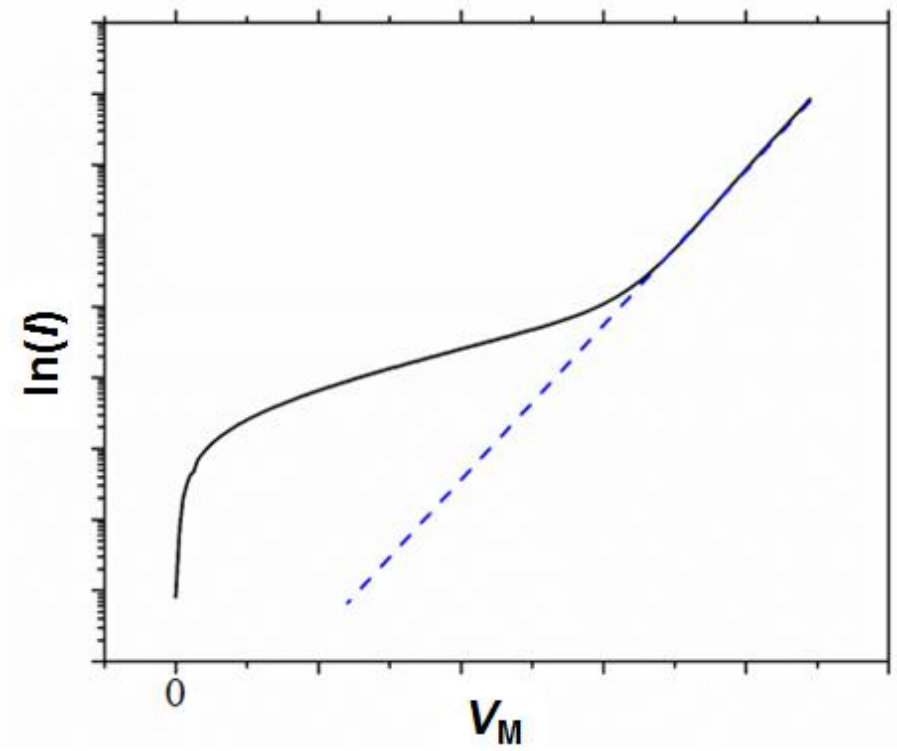

Figure 2.9. Evaluation of the main diode parameters of a solar cell after correction *of* R_S.

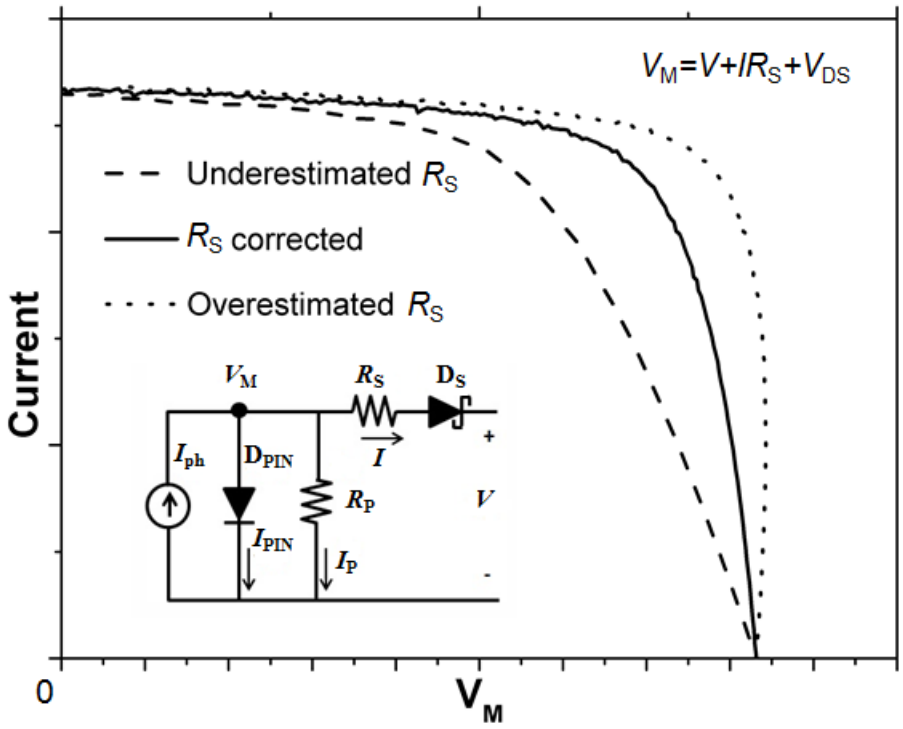

Figure 2.10. Correction of R_S applied to the illuminated *I-V* curve and equivalent circuit of the solar cell when characterized in the dark

In the same way that the dark *I-V* curve is corrected using the extracted value of series resistance, the light *I-V* curve must be corrected too. This is done by adding the drop of voltage across R_S from the applied voltage. The value of R_S used in the correction will have a deep impact on the *FF* and P_{MAX} as highlighted in Fig. 2.10. Figures 2.8 and 2.10 are general examples only, and numeric values of the parameters evaluated from the curves are discussed in chapters 4, 5, and 6. The intention of this correction is to separate the effect that each element of the equivalent circuit introduces on the behaviour of the *I-V* curve. In this case, correcting for R_S allows to identify the role that D_{PIN} and D_S play on the performance and stability of the solar cell, as will be presented in chapter 6.

2.5 Optical characterization: Quantum efficiency

The quantum efficiency (*QE*) is the ratio of carriers collected by a solar cell to the number of photons of a given energy that impact the cell, and it can be expressed as a function

of wavelength or energy. *QE* is an indicator of how good a solar cell is at the conversion of light to electricity [2.8]. Two types of *QE* measurements for solar cells can be considered:

1) External Quantum Efficiency (EQE), which includes the effects of optical losses such as transmission through the cell or reflection of light.

2) Internal Quantum Efficiency (IQE), which considers only the portion of light that is able to generate carriers.

If the reflection and transmission of a device are known, the EQE curve can be calculated from the IQE curve.

Quantum efficiency in most solar cells is reduced due to recombination, impeding charge carriers to move to the external circuit. Also, any mechanism that affects the probability of collection of carriers also affects the *QE*. *QE* as function of wavelength for different materials used in solar cells are shown in Fig. 2.11. For wavelengths longer than the band gap, the *QE* is reduced to zero.

In order to calculate the *QE* of a device, the value of power reaching the cell and the current produced at each wavelength are needed. The ratio of the current of the cell, I_C to the beam power can be expressed as a percentage of *QE* given by Eq. 2.10, where h is the Planck constant, c the speed of light in vacuum, e the elementary charge, λ the wavelength, and I_{ref} represents the current of a calibrated reference and $R(\lambda)$ is the value of response of the reference detector in A/W.

$$QE = \frac{100\mathrm{hc}I_c(\lambda)}{\mathrm{e}\lambda I_{\mathrm{ref}}\mathrm{R}(\lambda)} \tag{2.10}$$

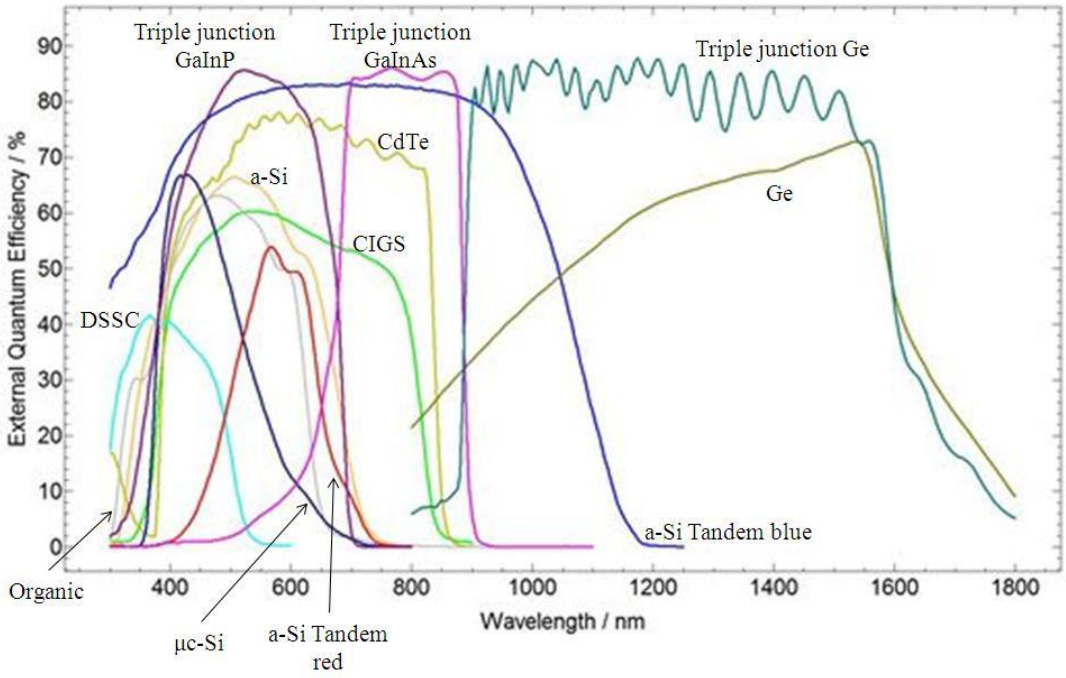

Figure 2.11. EQE graph for different materials used in solar cells. [Picture taken from Bentham, Spectral and Spatial Characterization of PV Devices and Materials. Available online at http://www.bentham.co.uk/images/Systems/PV/spectra%20eqe33pc.jpg. Used with permission of Bentham Technical Support. Accessed on June 2016.

2.6 Experimental details and methodology

All the samples used in the experiments conducted within this thesis were supplied by the University of Bielefeld in Germany. The experimental details for each stage are described below.

1) ZnO/p-type thin film silicon interface: ZnO/a-Si:H(p) and ZnO/µc-Si:H(p) diode structures (Fig. 2.12a) were deposited on soda lime glass in order to examine the electrical properties of different contacts for solar cells. The hydrogen/silane (H_2/SiH_4) ratio was kept constant at 600 for all µc-Si:H(p) layers and at 10 for the a-Si:H(p) layers. The doping concentration of the p-layers was varied by controlling the trimethyl borane (TMB) / silane ratio $B(CH_3)_3/SiH_4$, which was set to 0.4 for both types of samples. The gas flow for the a-Si:H(p) layer was 200 sccm, whereas the gas flow for the µc-Si:H(p) layer was set to

50 sccm. These were referred as the standard samples with a flow of 100%. More samples were prepared with 66% and 33% of the flow for each type of diode structure. Here, the TMB/silane ratio decreased as the TMB flow decreased. Other details of the deposition process remain confidential. The area of all the diode samples was 0.008435 cm^2 with a ZnO layer thickness of 1.8 µm deposited on a thin film of a-Si:H(p) or µc-Si:H(p) of 15 nm of thickness. Silver was used to contact both materials, since the electrical characterization of the diode structures do not require to be done in the presence of light. The electrical characterization consisted of current density – voltage – temperature (*J-V-T*) measurements in a cryogenic probe station, in the temperature range 208-318 K. The outcome of this experiment was the quantification of the rectifying properties for the different contacts by evaluation of their Schottky barriers and ideality factors, *n*.

2) Effect of the ZnO/p-type thin film silicon window layer on the performance and stability of the cell: The best diode structures fabricated during the previous stage were implemented as in solar cells of area 1 cm^2 (Fig 2.12b). A third p-type layer made of µc-Si:H(p)/a-Si:H(p) was also tested. The thickness of the ZnO/p-layer/a-Si:H(i)/a-Si:H(n)/ZnO layers are 1800 nm, 15 nm, 220 nm, 25 nm, and 1500 nm respectively, with a tolerance of +/-20%. These were measured at the University of Bielefeld using a contact profilometer. The deposition parameters are the same as those mentioned in 1). Here, the electrical characterization was performed under 1 sun, AM1.5 and in dark conditions too. The effects of the different window layers on the performance of the cell were studied in the annealed conditions, whereas the stability was studied by measuring at different time intervals during light exposure and current injection. The outcome of this stage was the production of a computer model and an equivalent electronic circuit model of the solar cell that takes into account non-ideal contacts.

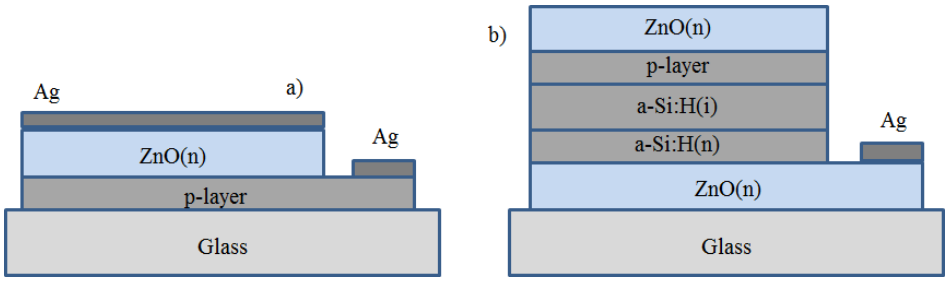

Figure 2.12. Structures fabricated by the University of Bielefeld in order to study the a) Schottky barrier height at the contact interface, and b) the effect of the window layer and its Schottky interface with ZnO on the performance and stability of the solar cell.

2.7 Summary of Chapter 2

The evaluation of the performance of a solar cell using *J-V* measurements is described. The *J-V* curves are modelled with a simple electronic circuit in order to improve the different parameters of the cell. However, the conventional model used has some issues such as: 1) there is no standard procedure to extract the values of the different elements that compose the electronic circuit model, often leading to the wrong extracted values, especially when there is a high dependence of one parameter on another; and 2) the conventional model assumes that contacts are 100% Ohmic, which is not the case for different solar cell technologies. The focus of this chapter is on the methodology used to extract the elements of the equivalent circuit with better accuracy. It was mentioned that the typical reason of an inaccurate extraction is a wrong extraction of R_S. It was shown that only the correct evaluation of R_S allows to distinguish the effects of contact resistance from those of the main junction diode of the solar cell. This a critical step to identify the elements of the equivalent circuit model that degrade during a reliability test.

2.8 References in Chapter 2

[2.1] ASTM G173-03(2012), "Standard tables for reference solar spectral irradiances: direct normal and hemispherical on 37° tilted surface," ASTM International, developed by subcommittee G03.09, Book of Standards vol. 14.04, 2012.

[2.2] ASTM E490-00a(2014), "Standard solar constant and zero air mass solar spectral irradiance tables," ASTM International, developed by subcommittee E21.04, Book of standards vol. 15.03, 2014.

[2.3] Reference solar spectral irradiance: ASTM G-173. Available at http://rredc.nrel.gov/solar/spectra/am1.5/ASTMG173/ASTMG173.html. Accessed on 8/02/2016.

[2.4] S. R. Rummel and T. J. McMahon, "Effect of cell shunt resistance on module performance at reduced light levels," in 13th NREL Photovoltaics Program Review, Lakewood, CO, 1995.

[2.5] E. L. Meyer and E. E. van Dyk, "Assessing the reliability and degradation of photovoltaic module performance parameters," *IEEE Transactions on Reliability*, vol. 53, no. 1, pp. 83-92, Mar. 2004.

[2.6] E. L. Meyer and E. E. van Dyk, "Characterization of degradation in thin-film photovoltaic module performance parameters," *Renewable Energy*, vol. 28, no. 9, pp. 1455-1469, Jul. 2003.

[2.7] C. Radue and E. E. van Dyk, "Pre-deployment evaluation of amorphous silicon photovoltaic modules," *Solar Energy Materials and Solar Cells*, vol. 91, no. 2-3, pp. 129-136, Jan. 2007.

[2.8] O. Breitenstein, J. Bauer, A. Lotnyk, and J.-M. Wagner, "Defect induced non-ideal dark II–VV characteristics of solar cells," *Superlattices and Microstructures*, vol. 45, no. 4-5, pp. 182-189, Apr. 2009.

[2.9] O. Breitenstein, P. Altermatt, K. Ramspeck, M. A. Green, J. Zhao, and A. Schenk, "Interpretation of the commonly observed I-V characteristics of c-Si cells having ideality factor larger than two," *IEEE 4th World Conference on Photovoltaic Energy Conference*, pp. 879-884, 2006.

[2.10] M. Bivour, C. Reichel, M. Hermle, and S. W. Glunz, "Improving the a-Si:H(p) rear emitter contact of n-type silicon solar cells," *Solar Energy Materials and Solar Cells*, vol. 106, pp. 11–16, 2012.

[2.11] K. U. Ritzau, M. Bivour, S. Schröer, H. Steinkemper, P. Reinecke, F. Wagner and M. Hermle, "TCO work function related transport losses at the a-Si:H/TCO-contact in SHJ solar cells," *Solar Energy Materials and Solar Cells*, vol. 131, pp. 9–13, 2014.

Disclaimer notice for Fig. 2.2 [Available at http://www.nrel.gov/disclaimer.html, accessed on July 2016]

Chapter 3.

ZnO / p-type Si interface

This chapter describes the fundamentals about the formation of a Schottky junction. The non-ideal behaviour of a Schottky diode is detailed by studying the different transport mechanisms across a Schottky interface. A technique to extract the Schottky barrier height from J-V measurements of a Schottky diode is also described.

The focus of this chapter is on the basic theory behind the formation of a Schottky barrier. Here, the concept of Fermi level plays a significant role in the formation of semiconductor junctions and metal-semiconductor contacts. The concept of Fermi level is useful to understand the effects of doping concentration on the energy band diagrams of a semiconductor. Also, the ideal case of formation of a Schottky barrier for a metal-semiconductor contact is explained and compared to the practical case. The information and methodology presented in this chapter are key to discuss the experiments conducted on ZnO/a-Si:H and ZnO/µc-Si:H structures, in chapter 4.

3.1 Formation of a Schottky barrier

The difference between the work functions of a metal and a semiconductor, and the misalignment of the energy bands of the semiconductor with the work function of the metal can generate a barrier with rectifying properties on a metal-semiconductor contact. This asymmetry in conduction was originally reported in 1874 by Braun between metal points and crystals such as lead sulphide [3.1]. In 1906, Pickard filed a patent for a point contact rectifier based on silicon [3.2] and one year later, Pierce published rectifying properties of sputtered metals in a variety of semiconductors [3.3]. This phenomenon occurs at the ZnO / p-type silicon interface of a thin film solar cell providing that ZnO is degenerately doped. This allows ZnO to be approximated as a metal since its Fermi level is above or considerably close to E_c, as it was shown in section 1.3, thus filling the top of E_c with electrons.

Fig. 3.1 shows the formation of a barrier height for a metal/p-type semiconductor interface according to ideal Schottky barrier theory. The energy band diagrams for both materials in isolation is shown in Fig. 3.1a). Here, the most important properties such as work function of the metal Φ_M, and electron affinity X_S, ionization potential IP_S, and work function Φ_S of the semiconductor, are all referenced to the vacuum level E_{VAC} [3.4]. Since $\Phi_S > \Phi_M$ in this example, there is an electron charge transfer from the metal to the semiconductor which equalizes the Fermi levels once both materials are brought into contact. This causes a built-in potential V_{bi} and a local vacuum level E_{LVAC} to appear as a consequence of the charge transfer. A Schottky barrier height Φ_{bp} is also created, which represents a

potential barrier that holes in the p-type semiconductor must overcome to transit to the metal side [3.4]. The value of Φ_{bp} for an ideal contact is represented by the Schottky-Mott approximation in Eq. 3.1. This equation needs to be expanded for non-ideal contacts as will be explained further in this section.

$$\Phi_{bp} = IP_S - \Phi_M = (X_S + E_g) - \Phi_M \tag{3.1}$$

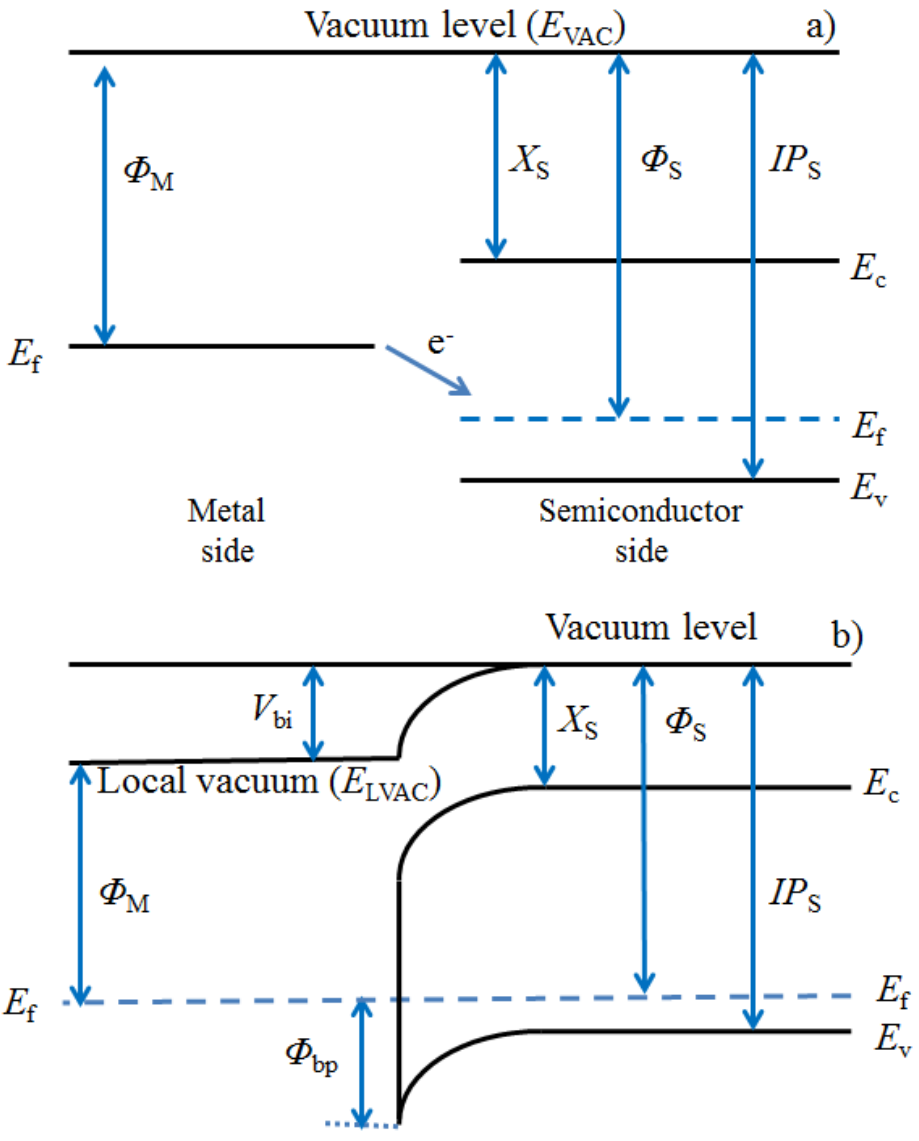

Figure 3.1. Energy band diagrams for a metal-p-type semiconductor contact when $\Phi_M<\Phi_S$. Materials are shown in isolation (a) and after contact (b). All parameters are referenced to the vacuum level under the basis of ideal Schottky barrier theory.

Once the process of formation of a Schottky barrier has been explained, it is now possible to describe the effects of different values of work function and extrinsic type of semiconductor. Fig. 3.2 shows the case when $\Phi_S < \Phi_M$, where a flow of electrons from the semiconductor into the metal equalizes the Fermi levels and produces a depletion region in the semiconductor. This bends the bands upwards as shown in Fig. 3.2a) for n-type semiconductors. Here, the electrons need to overcome the barrier Φ_{bn} to be able to pass from the semiconductor into the metal, which results in rectifying properties. For the case of a p-type semiconductor, the bending of the band does not stop the flow of holes, thus the contact becomes Ohmic as shown in Fig. 3.2b) [3.5].

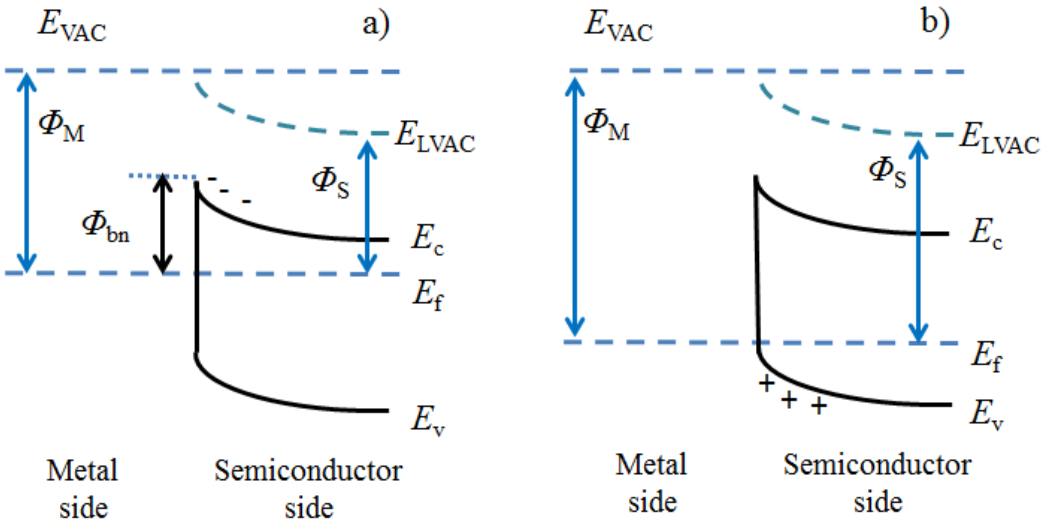

Figure 3.2. a) Schottky barrier for an n-type semiconductor when $\Phi_M > \Phi_S$. The Fermi levels equalize once that materials are in contact, which causes the bands to bend upwards and to create a barrier Φ_{bn} that electrons need to overcome to cross from the semiconductor to the metal, thus rectifying properties are achieved. b) When $\Phi_M > \Phi_S$ for a p-type material, the bending of the bands does not prevent the motion of holes, and a contact with Ohmic instead of rectifying properties is created.

On the other hand, the bands bend downwards when $\Phi_M < \Phi_S$. For this case, an Ohmic behaviour is achieved for n-type materials, since the flow of electrons does not find a barrier as shown in Fig. 3.3a), whereas a rectifying contact is created for p-type material, where holes find difficulties to pass underneath the barrier, as shown in Fig. 3.3b). Generally, the

case $\Phi_M > \Phi_S$ is true for most of the metal/n-type semiconductor contacts, whereas $\Phi_M < \Phi_S$ is true for most of the metal/p-type semiconductor contacts therefore, the majority of the metal-semiconductor contacts produce Schottky contacts [3.5]. However, ideal Schottky contacts as shown in Fig. 3.2 and Fig. 3.3 are seldom achieved due to a 1-2 nm thick layer of oxide on the surface of the semiconductor that acts as an interfacial layer [3.5]. A more realistic contact is comparable to a metal-insulator-semiconductor junction, as shown for a p-type semiconductor when $\Phi_M < \Phi_S$ before and after contact in Fig. 3.4a) and Fig. 3.4b) respectively. Here, the insulator layer has a wide bandgap structure which represents an enormous barrier for holes however, there is a possibility for holes to travel through the insulator without the need to overcome the barrier. More details will be provided in section 3.3.

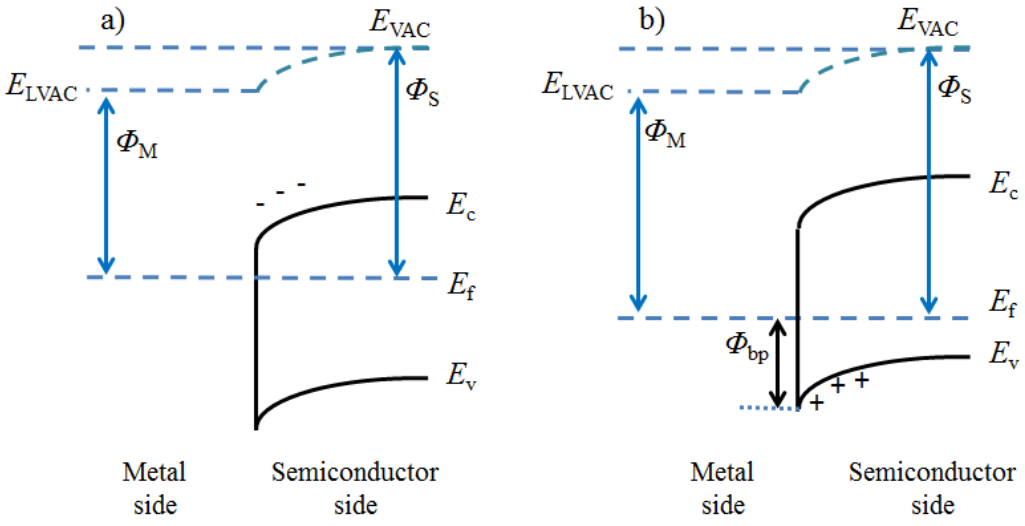

Figure 3.3. When $\Phi_M < \Phi_S$ bands are bent downwards and, a) Ohmic properties are achieved for n-type semiconductors whereas b) p-type semiconductors produce rectifying contacts due to the difficulty of holes to pass below the barrier Φ_{bp}.

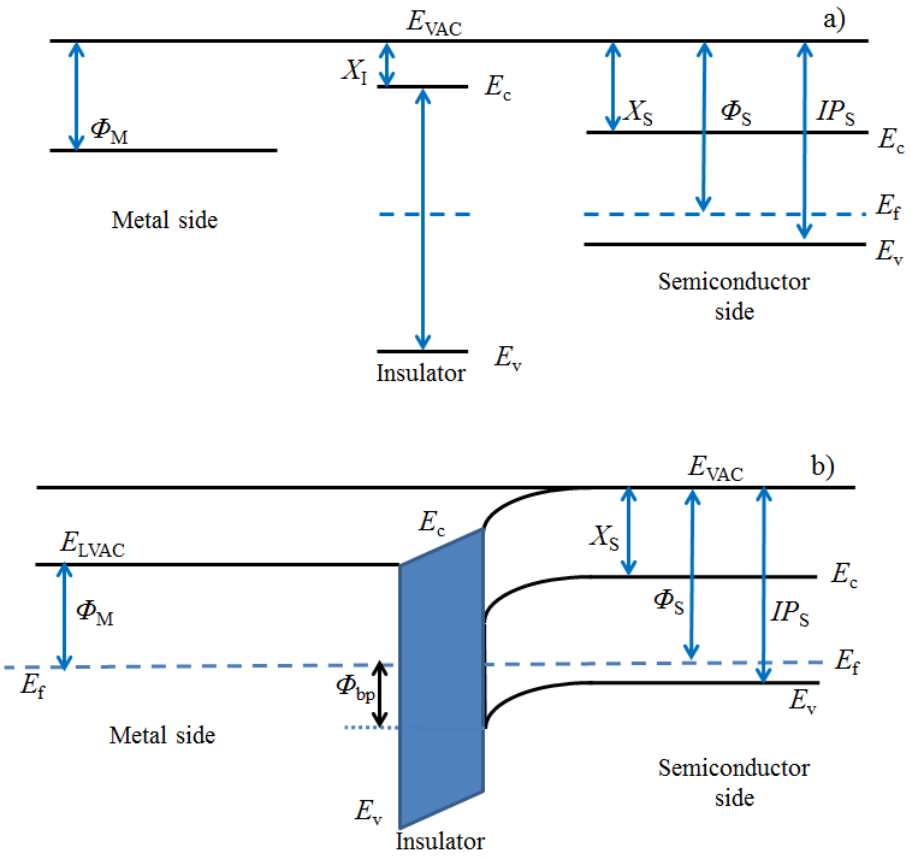

Figure 3.4. Practical case of a metal-semiconductor contact for a p-type material when $\Phi_M<\Phi_S$ including an interfacial layer of thin oxide between the materials.

Such non–idealities in a Schottky barrier interface are considered by incorporating a charge neutrality level E_{CNL} into the semiconductor. E_{CNL} represents the point within the bandgap of a semiconductor where states below are mainly valence band or donor-like. The electrical charge in donor-like states becomes positive when they emit an electron, and neutral when filled by an electron. Similarly, states above the E_{CNL} are conduction band or acceptor-like states, which are electrically neutral when they are empty, and negatively charged when they trap an electron. The convention used to name these trap states should not be confused with the names of atoms used to dope semiconductor, where donor atoms introduce levels close to E_c, whereas acceptor atoms introduce levels close to E_V.

The position E_{CNL} relative to the metal Fermi level when both materials are isolated will determine the direction of non-ideal additional charge transfer. In Fig. 3.5a), E_{CNL} can

be found above the metal Fermi level, thus additional charge needs to be transferred from the semiconductor to the metal, which will result in an increase of the built-in potential and the Schottky barrier height as in Fig. 3.5b). If the charge neutrality level is positioned below E_F, then the charge transfer occurs from the metal to the semiconductor. The effect this time will be opposite, decreasing the built-in potential and the Schottky barrier.

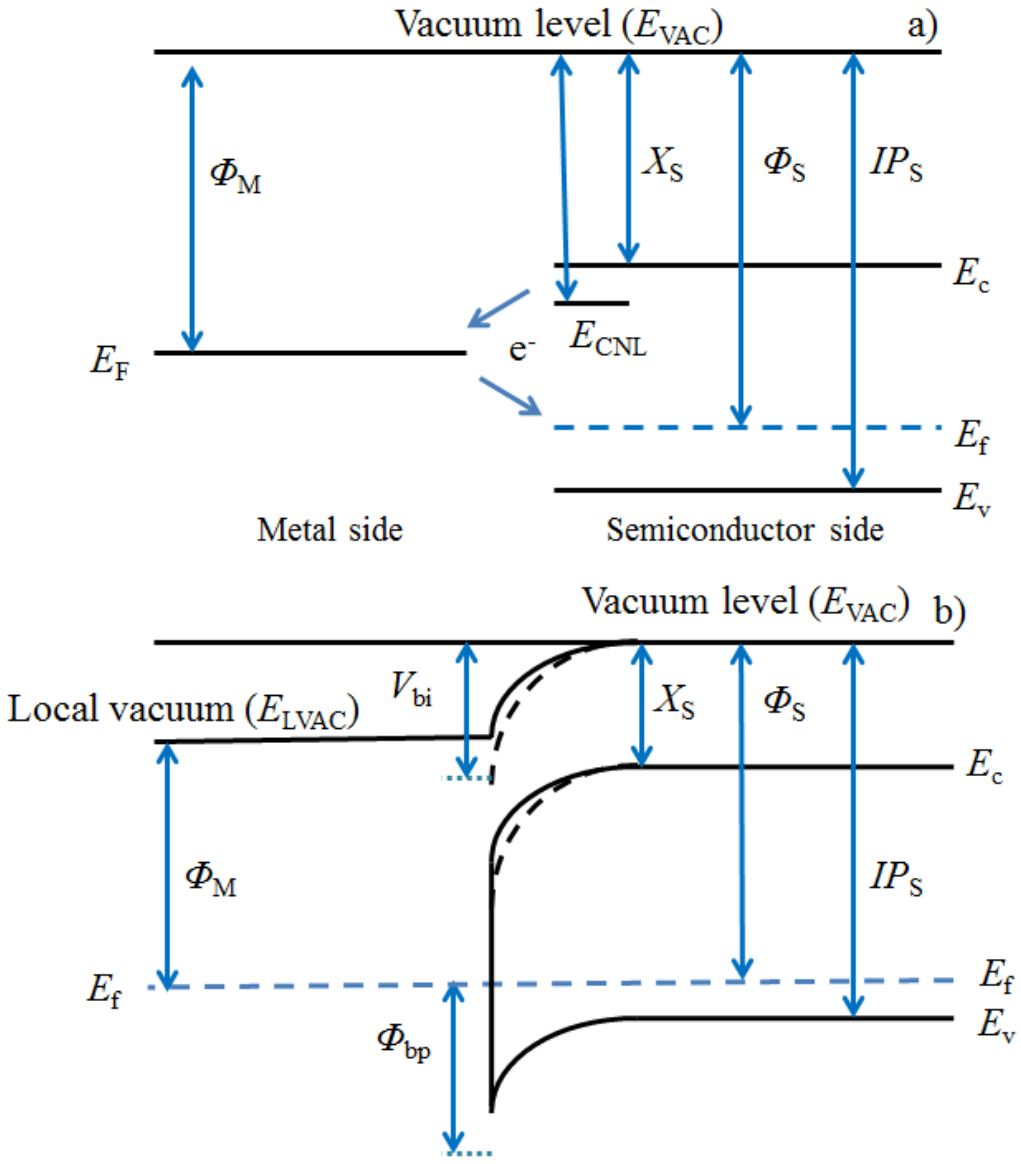

Figure 3.5. Energy band diagrams for a p-type semiconductor when $\Phi_M<\Phi_S$ and $\Phi_M>\Phi_{CNL}$. Materials are shown while isolated (a) and after contact (b). An increase in the Schottky barrier height Φ_{bp} is a consequence of the negative microscopic dipole (electron charge transfer from semiconductor to metal).

The Schottky barrier for a p-type semiconductor including non-idealities can be represented by Eq. 3.2.

$$\Phi_{\mathrm{bp}} = IP_{\mathrm{S}} - \Phi_{\mathrm{M}} - \Delta_{\mathrm{SB}} \tag{3.2}$$

where Δ_{SB} is the Schottky barrier microscopic dipole correction, which includes the transfer of non-ideal charges between the semiconductor E_{CNL} and E_{f} due to misalignments of both levels [3.6]. If Δ_{SB}=0 then the junction becomes ideal.

3.2 Measurement of the Schottky barrier height

Due to its simplicity, *I-V* measurements are the most common method to evaluate a Schottky barrier. In this case, pure thermionic emission over the barrier is assumed and represented by Eq. 3.3.

$$I_1 = I_{\mathrm{te}}\left[e^{\left(\frac{\mathrm{q}V}{\mathrm{k}T}\right)} - 1\right] \tag{3.3}$$

where k represents the Boltzmann constant and T the absolute temperature. In order to refine Eq. 3.3, the series resistance R_{S} and the ideality factor n, are introduced to include the contributions of other current transport mechanisms [3.9]

$$I = I_{\mathrm{te}}e^{\left[\frac{\mathrm{q}(V-IR_{\mathrm{S}})}{nkT}\right]}\left[1 - e^{\left[\frac{-\mathrm{q}(V-IR_S)}{\mathrm{k}T}\right]}\right] \tag{3.4}$$

$$I_{\mathrm{te}} = A\mathrm{A}^{**}T^2e^{\left(\frac{-\mathrm{q}\Phi_{\mathrm{b}}}{\mathrm{k}T}\right)} \tag{3.5}$$

Eq. 3.5 represents the saturation current, where A is the area of the diode and A^{**} the effective Richardson constant.

By extrapolating the semilog *I-V* curve, the value of saturation current can be calculated as the intercept of the vertical axis obtained from the slope of the linear region of the same plot. An example is shown in Fig. 3.6.

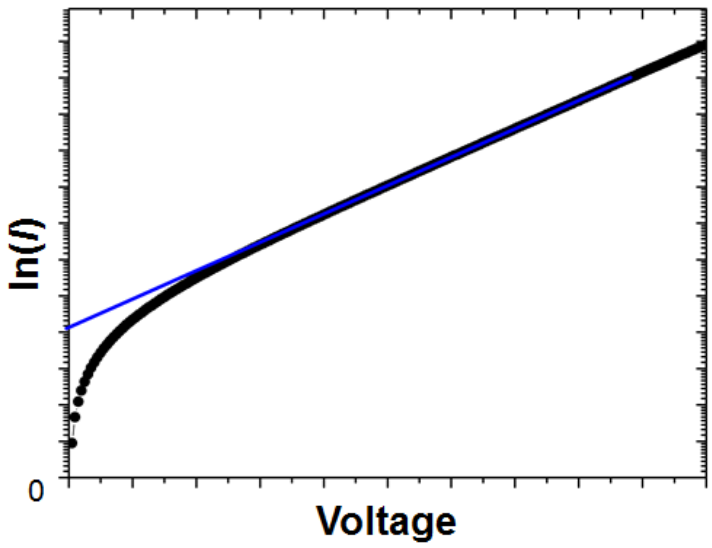

Figure 3.6 Example sketch of extrapolation of the linear region of an *I-V* curve. The ideality factor is calculated from the slope of the linear region and the saturation current as the vertical axis intercept of the extrapolated section.

In the presence of multiple transport mechanisms simultaneous to thermionic emission such as quantum mechanical tunnelling through the barrier, generation-recombination in the space charge region or leakage current through the contact periphery, the linear region of the semilog plot can be altered or reduced, which complicates the extraction of saturation current and other parameters. However as soon as thermionic emission is no longer the only dominant transport mechanism or the value of R_S becomes too large, the magnitude of the ideality factor starts to increase, therefore calculating the Schottky barrier height Φ_B may lead to inaccurate values or to a lack of linear region on the plot [3.8, 3.9]. An example can be seen in Fig. 3.7.

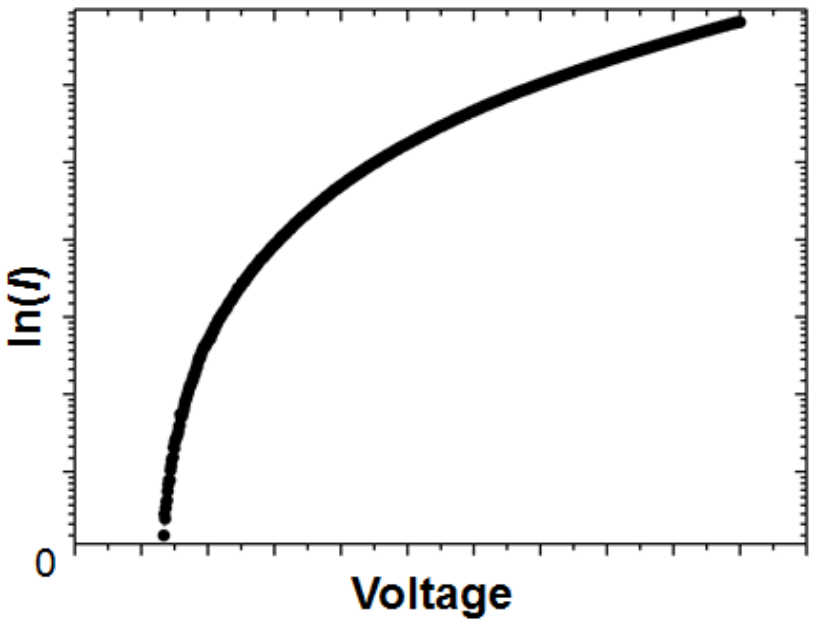

Figure 3.7. Example of a non-ideal *I-V* curve. Multiple transport mechanism have a detrimental effect on the ideal rectifying properties of the metal-semiconductor interface, which causes difficulties to extract the parameters of the Schottky barrier

3.2.1 Evaluation of the Schottky barrier height by current – voltage measurements

The Schottky barrier is evaluated from *I-V* measurements when an applied forward bias is large enough to set the diode in the on-state. Assuming a large value of *V* and including the ideality factor *n*, then the *I-V* characteristics become as in Eq. 3.6 and Eq. 3.7.

$$I = I_{SS} e^{\left(\frac{qV}{nkT}\right)} \tag{3.6}$$

$$ln(I) = \ln(I_{SS}) + \frac{qV}{nkT} \tag{3.7}$$

If ln(*I*) is plotted against *V*, ideally a straight line with slope q/*n*kT and vertical axis intercept ln(I_{SS}) should be obtained, which allows to calculate *n* and Φ_b as,

$$n = \frac{\mathrm{q}}{\mathrm{k}T}\frac{dV}{dln(I)} \tag{3.8}$$

$$\Phi_{\mathrm{b}} = \frac{\mathrm{k}T}{\mathrm{q}}\ln\left(\frac{AA^{**}T^2}{I_{\mathrm{SS}}}\right) \tag{3.9}$$

This will give the barrier height at zero bias however, uncertainties in the value of A^{**} may lead to incorrect results [3.10].

3.2.2 Schottky barrier height by current – temperature measurements

A Richardson plot is obtained by plotting $\ln(I/T^2)$ versus $1/T$ at a constant value of voltage $V=V_1$, which has a slope of $-q(\Phi_b-V_1/n)/k$ and a vertical axis intercept at $\ln(AA^{**})$. The problem to find the Richardson constant from this plot arises due to the big range of temperature values that the slope needs to be extrapolated. Barrier height is calculated from Eq. 3.10.

$$\Phi_{\mathrm{b}} = \frac{V_1}{n} - \frac{\mathrm{k}}{\mathrm{q}}\frac{d[\ln(I/T^2)]}{d(I/T)} \tag{3.10}$$

For this case, the ideality factor n, must be evaluated independently. This can be avoided by choosing a value of $V_1=0$, but $I=I_{SS}$ will be needed. Furthermore, if a temperature dependence of barrier height ξ, measured in eV/K is considered, then

$$\Phi_{\mathrm{b}}(T) = \Phi_{\mathrm{b}}(0) - \xi T \tag{3.11}$$

from which

$$\ln(I/T^2) = \ln(AA^{**}) + \mathrm{q}\xi/\mathrm{k} - \mathrm{q}(\Phi_{\mathrm{b}}(0) - V/n)/\mathrm{k}T \tag{3.12}$$

Now the barrier height at zero Kelvin is obtained and the vertical axis intercept will give $\ln(AA^{**})+q\xi/k$ and A^{**} cannot be determined anymore due to non-linearities caused by mechanisms other than thermionic emission, increasing the value of the ideality factor [3.11].

3.3 Transport mechanisms

Poor quality of the Schottky contact introduce transport mechanisms different to thermionic emission. Normally, these are unwanted effects in a Schottky contact however, it is possible to take advantage of them when an Ohmic contact is the priority. This is the case of a-Si:H solar cells, where Ohmic contacts are needed, but the lack of a p-type TCO with high work function necessitates the use of a material that can cause a Schottky interface. These transport mechanisms are described in this section.

3.3.1 Thermionic emission over the barrier

The first theory addressing the conduction mechanism in a Schottky diode was the diffusion theory proposed by Wagner [3.12] and Schottky and Spenke [3.13]. According to this theory, electrons emitted over the barrier from the semiconductor to the metal side must be transported through the depletion region, and their motion would be limited by the mechanisms of diffusion and drift. Bethe later proposed that the Fermi level for electrons remains horizontal across the depletion region, in the same way as in a p-n junction. This became known as the thermionic emission theory [3.14].

The barrier height Φ_B may depend on applied bias. One reason could be due to the presence of an interfacial layer (a thin oxide layer between the metal and semiconductor) causing a drop in voltage and thus reducing the barrier height. Furthermore, even without the existence of an interfacial layer, a bias dependence of barrier height can be found due to image force effect, which happens when an electron near to the surface of the metal is attracted to it by the positive image charge. The result of this effect is a reduction of barrier height by an amount proportional to the electric field in the semiconductor [3.5].

Considering a Φ_B that depends linearly on the applied bias, which is true for low voltage, and neglecting the series resistance, then a bias dependence can be established by $\Phi_b=\Phi_{b0}+\beta V$ where $\beta>0$. Therefore

$$I_1 = AA^{**}T^2 e^{\left[\frac{-q(\Phi_{b0}+\beta V)}{kT}\right]}\left[e^{\left(\frac{qV}{kT}\right)} - 1\right] = I_0 e^{\left(\frac{-q\beta V}{kT}\right)}\left[e^{\left(\frac{qV}{kT}\right)} - 1\right] \quad (3.13)$$

$$I_0 = AA^{**}T^2 e^{\left(-\frac{q\Phi_{b0}}{kT}\right)} \quad (3.14)$$

Eq. 3.13 is more often written in the literature as shown in Eq. 3.15, since a plot of $\ln[I/\{1\text{-}\exp(-qV/kT)\}]$ vs V results in a straight line whose intercept with the vertical axis gives the value of I_0. Here, the relation shown in Eq. 3.16 is used as a way to simplify Eq. 3.15 in terms of the ideality factor, n. This allows the evaluation of the Schottky diode parameters from a $\ln|I|$ - V plot as explained in section 3.2.1.

$$I = I_0 e^{\left(\frac{qV}{nkT}\right)}\left[1 - e^{\left(\frac{-qV}{kT}\right)}\right] \quad (3.15)$$

$$\frac{1}{n} = 1 - \beta = 1 - \frac{\partial \Phi_b}{\partial V} \quad (3.16)$$

If the ideality factor n is constant, then the term on the right (bias dependence of barrier) will also be constant.

3.3.2 Tunneling through the barrier

Electrons with low energy in an n-type semiconductor are not able to overcome the barrier via thermionic emission. However, it is possible for them to penetrate the barrier by means of tunnelling. For the case of p-type semiconductors, it is useful to think about holes tunnelling from the metal to the semiconductor in a similar way the electrons tunnel from the semiconductor valence band to the metal. The process of tunnelling is unwanted for rectification however, it is able to modify the thermionic emission process [3.5].

There exists a dependence of tunnelling transport on temperature. For degenerate semiconductors at low temperature, the donor density is high and the potential barrier becomes so thin that tunnel transport mechanism is highly probable. This is also known as

field emission. Tunnelling increases with temperature due to carriers being promoted to higher energy levels that now seem to find a thinner and lower barrier. This process is called, thermionic-field emission. If the temperature increases even further, all of the carriers obtain sufficient energy to overcome the barrier therefore, the effect of tunnelling is negligible and pure thermionic emission is reached.

The theory of field and thermionic-field emission was developed by Padovani and Stratton, and its *I-V* relation including resistive effects is expressed in Eq. 3.16 where E_0 is a parameter dependent on temperature and doping concentration [3.17].

$$I_2 = I_t e^{\left(\frac{q(V-IR_S)}{E_0}\right)} \tag{3.16}$$

Besides a deviation of the *I-V* relation from pure thermionic emission, tunnelling causes an increase in the magnitude of the current since it is a simultaneous transport mechanism. Although the ideal rectifying properties are lost by the introduction of tunnelling, a positive effect is achieved when the objective is to fabricate Ohmic contacts for semiconductors, which are often made of highly doped materials. Dependence of the barrier height on temperature and ideality factor are included in Eq. 3.17,

$$I_t = AA^{**}T^2 e^{(-a\chi^{1/2}\delta)} e^{\left(-\frac{q\Phi_{bf}}{nkT}\right)} \tag{3.17}$$

where Φ_{bf} is the flat band barrier height and $a\chi^{1/2}\delta$ represents the hole tunnelling factor.

3.3.3 Generation - Recombination

The current due to recombination near the middle of the gap is expressed by equation 3.18 and Eq. 3.19..

$$I_3 = I_{gr}\left[e^{\left(\frac{q(V-IR_S)}{2kT}\right)} - 1\right] \tag{3.18}$$

$$I_{gr} = {Aqn_i w}/{\tau} \tag{3.19}$$

where, n_i is the intrinsic concentration, w the thickness of the depletion region and τ the lifetime [3.5]. This transport mechanism is normally found in crystalline silicon.

3.3.4 Leakage current

$$I_4 = \frac{V - IR_S}{R_P} \tag{3.20}$$

Leakage current is expressed by Eq. 3.20, where R_S represents the series resistance and R_P the shunt resistance of the diode. A low value of R_P causes an abnormal increase of current in the low voltage region, whereas a large value of R_S limits the flow of current at high voltages. This modifies the *I-V* curve of the Schottky diode and compromises the linear region of the ln|*I*| - *V* plot, as was mentioned for the case of the solar cell in section 2.3. This leads to an overestimated evaluation of *n* therefore, a large value of *n* can be used as an indication of leakage current [3.9].

3.4 Summary of Chapter 3

Chapter 3 describes the theory of the formation of Schottky contacts, and the techniques to evaluate the Schottky barrier height from the analysis of the *J-V* curve of diode structures. Furthermore, the transport mechanisms across a Schottky interface are described, focusing on the two most important transport mechanisms that exist in the ZnO/a-Si:H(p) interface, which are 1) thermionic emission over the barrier, and 2) tunnelling through the barrier. An important distinction mentioned between these two transport mechanisms is that the former causes the process of rectification in a metal-semiconductor junction, whereas the latter is unwanted for rectification. The understanding of the concepts and equations presented in Chapter 3 is fundamental for the further development of TCAD models discussed in the next chapters.

3.5 References in Chapter 3

[3.1] F. Braun, "Uber die Stromleitung durch Schwefelmetalic", Annalen der Physik und Chemie, Vol. 153, No. 4, pp. 556-563, 1874. Reprinted in English as "On the current conduction in metal sulphides," in Sze, S.M. Semiconductor Devices: Pioneering Papers. (Singapore: World Scientific Publishing Co., 1991) pp. 377-380.

[3.2] G. W. Pickard, "Means for receiving intelligence communicated by electric waves," U. S. Patent 836,531 (Filed August 20, 1906. Issued Nov 20, 1906).

[3.3] G. W. Pierce, "Crystal rectifiers for electric currents and electric oscillations. Part I. Carborundum". *Physical Review* (Series I) pp. 25-31. 1907

[3.4] J. A. Spies, R. Schafer, J.F. Wager, P. Hersh, H.A.S. Platt, D.A. Keszler, G. Schneider, R. Kykyneshi, J. Tate, X. Liu, A.D. Compaan, W.N. Shafarman, "Pin Double-Heterojunction Thin-Film Solar Cell P-Layer Assessment," *Solar Energy Materials and Solar Cells*, vol. 93, no. 8, pp. 1296-1308, Aug. 2009.

[3.5] E. H. Rhoderick, "Metal-semiconductor contacts," *Electrical Engineering*. Vol. 129, Pt. 1, No. 1. February 1982.

[3.6] J. Wager, "Transparent electronics: Schottky barrier and heterojunction considerations," *Thin Solid Films*, vol. 516, no. 8, pp. 1755-1764, Feb. 2008.

[3.7] D. Donoval, M. Barus and M. Zdimal, "Analysis of I-V measurements on PtSi-Si Schottky structures in a wide temperature range," *Solid-State Electronics*, vol. 34 no. 12, pp. 1365-1373, 1991.

[3.8] D. Donoval, V. Drobny, and M. Luza, "A contribution to the analysis of the I-V characteristics of Schottky structures," *Solid-State Electronics*, vol. 42, no. 2, pp. 235-241, 1998.

[3.9] I. Ay and H. Tolunay, "The influence of Ohmic back contacts on the properties of a-Si:H Schottky diodes," *Solid-State Electronics*, vol. 51, no. 3. pp. 381-386, Mar-2007.

[3.10] David Wood, "Optoelectronic semiconductor devices," Prentice Hall, International series in optoelectronics, pp. 33-59, 1994.

[3.11] Dieter K. Schroder, "Semiconductor material and device characterization," third edition. Wiley- IEEE Press, pp 157-161.

[3.12] C. Wagner, "Theory of current rectifiers," *Phys. Z.*, vol 32, pp. 641 – 645, 1931.

[3.13] W. Schottky, and E. Spenke, "Quantitative treatment of the space-charge and boundary-layer theory of the crystal rectifier," *Wiss. Veroff. a. d. Siemens-Werken,* vol. 18, pp. 225-291, 1939.

[3.14] H. A. Bethe, 'Theory of the boundary layer of crystal rectifiers'. *MIT Radiation Laboratory Report* 43-12, 1942

[3.15] F. A. Padovani, and R. Stratton, "Field and thermionic-field emission in Schottky barriers," *Solid-State Electronics*, vol. 9, pp. 695-707, 1966.

Chapter 4.

Effective Schottky barrier height of TCO/Si interfaces

Extraction of the Schottky barrier height for ZnO/a-Si:H(p) and ZnO/µc-Si:H(p) heterojunction structures is achieved from J-V-T measurements. The experimental curves and extracted barriers are in reasonable agreement with the results of computer simulations. Both, experiments and simulations show that an increase of boron doping causes the contact to evolve from a Schottky to an Ohmic behaviour, as shown by an increase on the Schottky diode ideality factor.

In this chapter the electrical characterization of ZnO/a-Si:H(p) and ZnO/µc-Si:H(p) diode structures which are later used as contacts for solar cells is discussed. Here, each structure is analysed as a Schottky diode, where the effective Schottky barrier height is calculated from current-voltage measurements at different temperatures (*J-V-T*). For the transport mechanism mentioned, the diode ideality factor (*n*) is expected to be equal to 1, however larger values of *n* are often reported for the case of amorphous p-materials.

Ideality factors different from unity are a result of interface states or traps found at the metal-semiconductor interface. The main reason of deviation from ideal characteristics at medium bias levels is the influence of different transport mechanisms simultaneous to thermionic emission, thus altering the ideality factor.

The *J-V-T* characteristics for ZnO/a-Si:H(p) Schottky diodes with different metals have been studied previously, where it was found that thermionic emission is the dominant conduction mechanism above room temperature, whereas tunneling currents become more effective at lower temperatures as discussed by Tolunay in metal/a-Si:H diodes [4.1] and by Allen in nearly ideal metal/ZnO diodes [4.2]. The same behaviour has been detected for µc-Si thin films by Liu [4.3].

Since an effective p-type TCO for p-layers in solar cells is still under development, some methods that researchers have attempted in order to lower the Schottky barrier include, the replacement of the a-Si:H(p) layer with molybdenum oxide (MoO_3), which has a wide bandgap, high work function, and good electrical conductivity [4.4]. Another explored option is the use of interlayers between ZnO and p-type a-Si:H to reduce the barrier height. Some examples of interlayers include µc-Si:H(n) [4.5,4.6], amorphous hydrogenated germanium [4.7,4.8] n-type amorphous tungsten oxide [4.9], and metallic nanodots of high work function materials, such as gold, platinum, palladium, or silver [4.10]. A simpler but still effective approach is addition of a µc-Si:H(p) interlayer between ZnO and a-Si:H [4.11,4.12]. Some novel approaches still in development include the use of highly conductive and anti-reflective graphene-silica contact [4.13], or the use of a negatively charged tunnel layer (t^+) as a hole collector instead of the p-layer, creating a t^+-i-n structure [4.14]. The importance of assessing

the ZnO/p-type Si Schottky barrier at the interface is essential for the optimization of the solar cell.

The experiments conducted in this chapter follow a similar methodology as the one presented in [4.1 – 4.3] however, the results shown here are specifically analysed in the context of contacts for solar cells in order to discuss the current issues of the contacts consisting of ZnO/a-Si:H(p) and ZnO/µc-Si:H(p) layers. The results presented in this chapter have been published in [4.15] and are important for developing the full electronic circuit presented in chapter 5, which includes the effects of the Schottky barrier on the performance of the solar cell.

4.1 Evaluation of Schottky barrier for ZnO/µc-Si:H(p) and ZnO/a-Si:H(p) interfaces

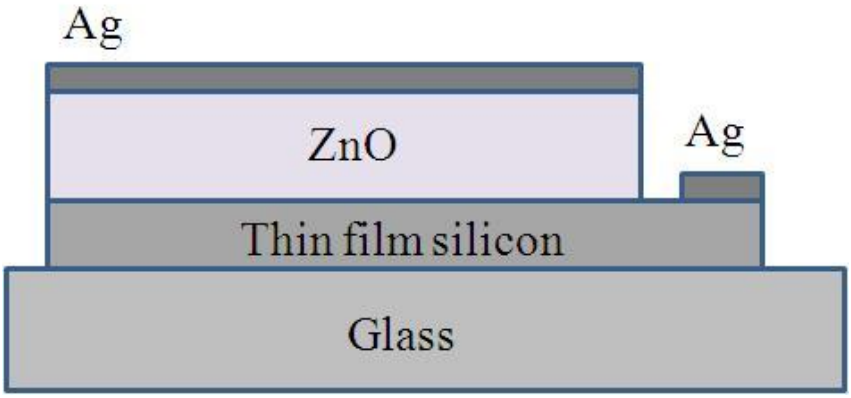

Figure 4.1. Structure of the fabricated heterojunctions. The thin film silicon layer represented in the diagram consisted of either a-Si:H and/or µc-Si:H.

Fig. 4.1 shows the structure used to evaluate the Schottky barrier height in the contact of thin film silicon solar cells. The fabrication details of the a-Si:H(p) or µc-Si:H(p) thin film layers are described in section 2.6, whereas the analytical procedure to evaluate the Schottky barrier height from *J-V* measurements under the assumption of thermionic emission is explained in section 3.2. Ideally, the value of the Schottky barrier Φ_{bp} should depend only on the fundamental properties (bandgap and work function) of the materials used to fabricate

the device, as expressed in Eq. 4.1, where X_S is the electronic affinity of the semiconductor, E_g the bandgap of the semiconductor, and Φ_M the work function of the metal.

$$\Phi_{bp} = X_S + E_g - \Phi_M \tag{4.1}$$

Fig. 4.2 shows the expected transport mechanisms at the metal-semiconductor interface of the fabricated devices. Here, tunnelling transport (also known as field emission), can occur if (1) the doping concentration of the semiconductor is high enough to narrow the depletion region, (2) the temperature is sufficiently low to eliminate transport over the barrier, or (3) a large reverse bias is applied. Additionally, Padovani and Stratton described the combination of thermionic emission and tunnelling transport which is achieved when temperature assisted carriers are able to tunnel through thinner regions of the depletion region. They refered to this transport as thermionic field emission [4.16]. This contribution of tunnelling transport causes the ideality factor to increase beyond n=1 and the Schottky barrier calculated from Eq. 3.5 to suffer an apparent decrease. This apparently reduced barrier height is referred as effective Schottky barrier height Φ_{eff}, and is the result of carriers tunnelling through the barrier at lower heights.

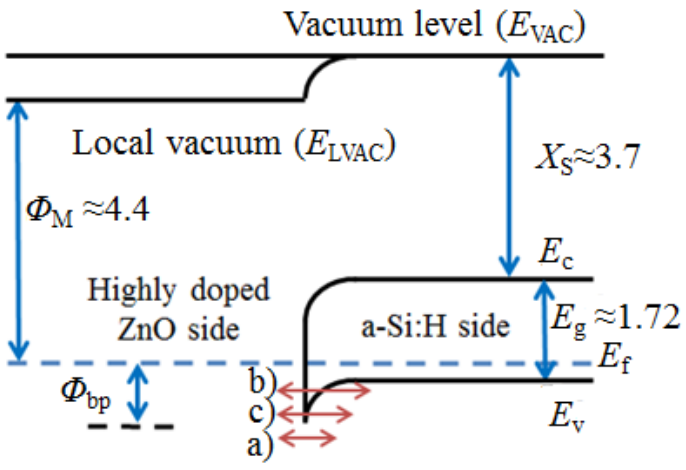

Figure 4.2. Metal-semiconductor contact for highly doped ZnO and a-Si:H not drawn to scale. All values are in eV. Horizontal arrows represent the different transport mechanisms present. (a) Thermionic emission over the barrier, (b) field emission or tunnelling through the barrier, and (c) thermionic field emission.

4.2 Description of the computer model

The effects of doping concentration on the different p-type layers used for the ZnO / thin film silicon heterojunctions were also studied by means of Technology Computer Aided Design (TCAD) simulations. The program used to perform the simulations was ATLAS from Silvaco TCAD. This program allows for a physics based study of 2-D and 3-D devices in order to predict the electrical characteristics of specified semiconductor structures under different bias conditions such as bias, temperature or light. This is done in ATLAS by representing the structure of the device as a 2-D or 3-D grid and by solving the Poisson equations, the carrier continuity equations and the transport equations [4.17] at different points of the grid. These equations are described in section 4.2.1. The problem to solve is then approximated as a non-linear algebraic system which depends on the set of equations to simulate and the specified grid. A variety of iterative methods can be chosen to solve the system of equations. Here, the Newton method is chosen to approximate the solution due to its simplicity and normally fast convergence.

4.2.1 Basic equations for simulation of semiconductors

The Poisson equation relates the electrostatic potential ψ to a local distribution of charge density ρ as shown in Eq. 4.2, where ε is the permittivity of the material. The local charge density corresponds to the contribution of all charges whether mobile or fixed, which includes electrons, holes and impurities. Once the Poisson equation is solved, the electric field can be calculated as the gradient of the potential as shown in Eq. 4.3.

$$div(\epsilon\nabla\psi) = \nabla\cdot(\epsilon\nabla\psi) = -\rho \tag{4.2}$$

$$\vec{E} = -\nabla\psi \tag{4.3}$$

The continuity equations are based on the principle that the number of carriers is conserved. This is represented for electrons and holes in Eq. 4.4 and Eq. 4.5 respectively, where G is the rate of generation and R the rate of recombination of carriers. Fig. 4.3

illustrates the continuity equations Eq. 4.4 and Eq. 4.5 as the flow of current through a differential volume, dV=dAdx within the semiconductor. Added to the generation G and recombination R of carriers, carriers can be introduced or removed by currents flowing inside and outside of dV.

$$\frac{\partial n}{\partial t} = \frac{1}{\mathrm{q}} \nabla \cdot J_{\mathrm{n}} + G_{\mathrm{n}} - U_{\mathrm{n}} \tag{4.4}$$

$$\frac{\partial p}{\partial t} = \frac{1}{q} \nabla \cdot J_{\mathrm{p}} + G_{\mathrm{p}} - U_{\mathrm{p}} \tag{4.5}$$

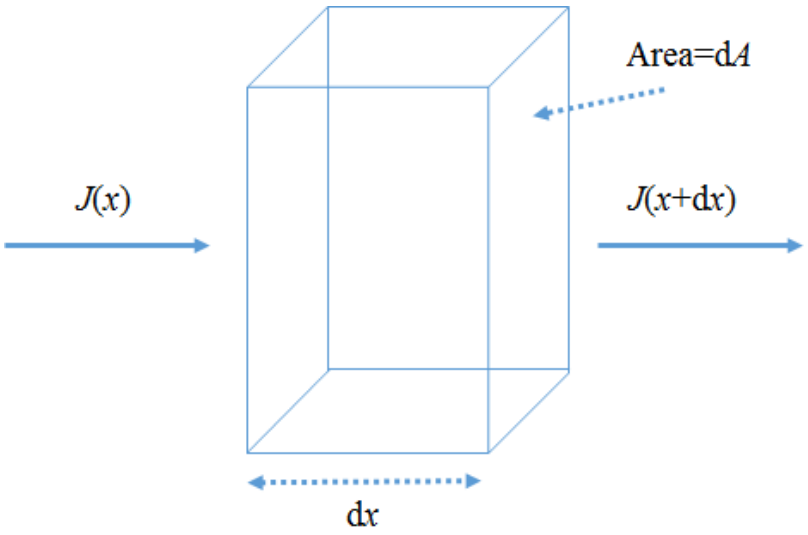

Figure 4.3. Representation of the continuity equation.

The transport equations used in these simulations are included in the drift-diffusion transport model. Here, the current densities J_{n} and J_{p} are expressed as shown in Eq. 4.6 and 4.7, where μ_{n} and μ_{p} are the electron and hole mobilities respectively.

$$\overrightarrow{J_{\mathrm{n}}} = -q\mu_{\mathrm{n}} n \overrightarrow{E_{\mathrm{n}}} + qD_{\mathrm{n}} \nabla n \tag{4.6}$$

$$\overrightarrow{J_{\mathrm{p}}} = -q\mu_{\mathrm{p}} n \overrightarrow{E_{\mathrm{p}}} + qD_{\mathrm{p}} \nabla p \tag{4.7}$$

D_n and D_p are the diffusion of electrons and holes respectively, which are simplified as shown in Eq. 4.8 and Eq. 4.9, where T_L is the temperature of the lattice, and μ_n and μ_p are the mobility for electrons and holes respectively.

$$D_n = \frac{kT_L}{q}\mu_n \tag{4.8}$$

$$D_p = \frac{kT_L}{q}\mu_p \tag{4.9}$$

4.2.2 Input parameters and models

Simulations for both types of heterojunctions are conducted and compared in the low voltage range to experimental measurements at room temperature (T=295 K). The program requires the input parameters such as electron affinity, bandgap, density of states, electron and hole mobilities and other for each material simulated, in order to estimate the electrical characteristics of a device.

For the case of amorphous materials, it is critical to define the density of states (DOS), which represents the quantity of allowed energy states per unit of volume per unit of energy. The DOS function is presented in Eq. 4.10, and it affects the electrical and optical properties of materials. This function depends only on the microscopic structure of the material.

$$g(E) = g_D^e(E) + g_A^e(E) + g_D^g(E) + g_A^g(E) \tag{4.10}$$

Eq. 4.10 represents two exponentially decreasing functions (Urbach tails) entering into the gap, which are the donor band tail $g_D^e(E)$ and the acceptor band tail $g_A^e(E)$. They indicate the degree of disorder in the atomic structure of the material. The higher the disorder in the atomic structure, the higher the quantity of energy states allowed between the valence and conduction bands [4.18]. The carriers that fall in these energy states are trapped and cannot contribute to the current of the system anymore, except if they are able to tunnel from one state to another of similar energy. These distributions exist for donor-like and acceptor-

like states as expressed in Eq. 4.11 and Eq. 4.12, where E_m represents the minimum energy value of the tail states, E_D and E_A are the characteristic decay energies of the band tails for donors and acceptors respectively, and g_0 is the maximum value of states in the tails.

$$g_D^e(E) = \frac{g_0}{2} exp\left(-\frac{E-E_m}{E_D}\right) \quad (4.11)$$

$$g_A^e(E) = \frac{g_0}{2} exp\left(\frac{E-E_m}{E_A}\right) \quad (4.12)$$

Besides the band tails, trap centres in the middle of the gap are also found for a-Si:H and µc-Si:H. These midgap states are subdivided in two types: traps that are charged for electron but keep neutral for holes are known as donor-like ($g_D^g(E)$), whereas traps that are charged for holes and keep neutral for electrons are considered acceptor-like ($g_A^g(E)$). Midgap states are distributed as a Gaussian function and represent the dangling bonds that are found in amorphous materials. These two Gaussian distributions are described by Eq. 4.13 and Eq. 4.14.

$$g_D^g(E) = \frac{N_D^G}{\sigma_D} \exp\left[-\frac{\left(E-E_D^g\right)^2}{2\sigma_D}\right] \quad (4.13)$$

$$g_A^g(E) = \frac{N_A^g}{\sigma_A} exp\left[-\frac{\left(E-E_A^g\right)^2}{2\sigma_A}\right] \quad (4.14)$$

For Eq. 4.13 and Eq. 4.14, E_D^g and E_A^g are the position in energy of Gaussian peaks for donor-like states and acceptor-like states respectively, while σ_D and σ_A define the standard deviation of the Gaussians, and N_D^g and N_A^g are the peak number of states of the Gaussian distributions.

Eq. 4.10 to Eq. 4.14 are implemented to build the DOS diagrams for a-Si:H and µc-Si:H as shown in Fig. 4.4. Also, a complete list of the parameters used for the materials in these simulations are shown in Table 1. All the parameters used were based on the literature

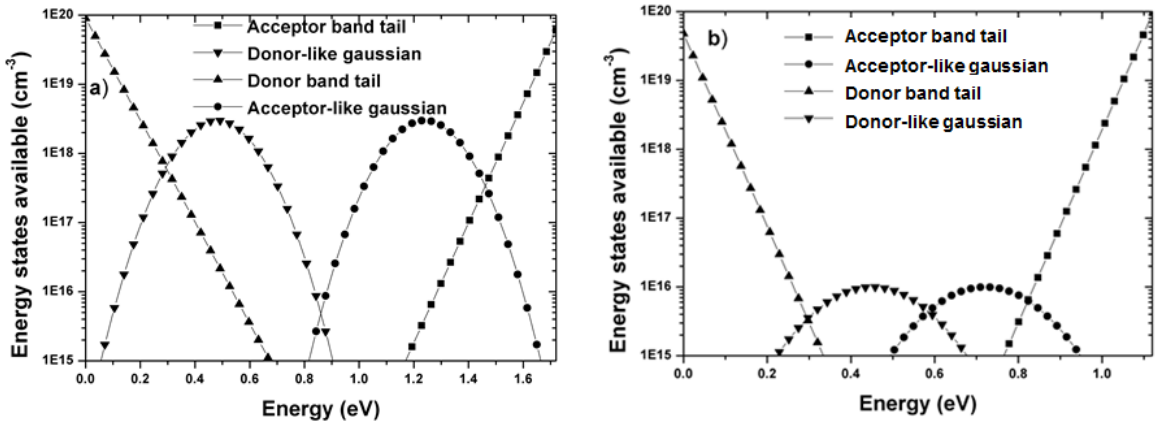

Figure 4.4. Density of states functions used in the simulations for a) a-Si:H(p) and b) µc-Si:H(p).

[4.19-4.32], and not measured experimentally, with the exception of the thickness, which has an experimental error of +/- 20%.

ATLAS also allows to include physical models to be considered during the simulations. Models are used to describe properties of the material and their dependence on doping concentration, temperature or voltage. They can also be used to select the transport mechanism that carriers will show in different sections of the device, such as bulk or interfaces. Models of recombination mechanisms are introduced to consider the reduction in current density due to non-idealities of the material such as defects.

The model of generation and recombination chosen can heavily impact the levels of current simulated. The process of carrier generation explains how electrons gain energy and become able to jump from the valence band to the conduction band, whereas the opposite case is known as recombination, and refers to electrons on the conduction band losing energy and reoccupying a place in the valence band.

The Shockley-Read-Hall model included in the simulations represents recombination as a two-step process in which a carrier is initially trapped by an energy state inside the bandgap that results from a defect in the lattice. Then, the trapped carrier is either released by thermal activation, or recombined with the opposite carrier. The SRH process is the dominant generation and recombination process in silicon, and is represented by Eq. 4.15,

Table 1. List of parameters used for TCAD simulations of the ZnO/a-Si:H and ZnO/μc-Si:H interfaces. A description of the parameters used to simulate the DOS (tail and Gaussian states) is included in section 4.2.2. The DOS modelled is shown in Fig. 4.4.

Parameter	***ZnO***	***a-Si:H***	***μc-Si:H***
Thickness (μm)	1.8	0.015	0.015
Donor concentration (cm^{-3})	10^{20}		
Acceptor concentration (cm^{-3})		$[2x10^{17}$, $3x10^{18}]$	$[10^{17}$, $3x10^{19}]$
Bandgap (eV)	3.3	1.72	1.124
Electron affinity (eV)	4.35	3.7	4
Effective conduction band density of states (cm^{-3})	10^{21}	$2.5x10^{20}$	$4.8x10^{19}$
Effective valence band density of states (cm^{-3})	10^{21}	$2.5x10^{20}$	$2.4x10^{19}$
Electron mobility ($cm^2\ V^{-1}\ s^{-1}$)	30	10	20
Hole mobility ($cm^2\ V^{-1}\ s^{-1}$)	3	1	5
Band tail states			
Peak density of states for acceptors ($cm^{-3}\ eV^{-1}$)		$6x10^{19}$	$9.6x10^{19}$
Peak density of states for donors ($cm^{-3}\ eV^{-1}$)		$9x10^{19}$	$4.8x10^{19}$
Characteristic decay energy for E_c tail (eV)		0.05	0.031
Characteristic decay energy for E_v tail (eV)		0.059	0.031
Electron capture cross section for donors (cm^2)		$2.5x10^{-15}$	$2.5x10^{-15}$
Hole capture cross section for donors (cm^2)		$2.1x10^{-17}$	$2.1x10^{-17}$
Electron capture cross section for acceptors (cm^2)		$2.1x10^{-17}$	$2.1x10^{-17}$
Hole capture cross section for acceptors (cm^2)		$2.5x10^{-15}$	$2.5x10^{-15}$
Gaussian states			
Peak density of states for acceptors ($cm^{-3}\ eV^{-1}$)		$8x10^{17}$	10^{16}
Peak density of states for donors ($cm^{-3}\ eV^{-1}$)		$8x10^{17}$	10^{16}
Peak energy for donor-like from E_v (eV)		0.48	0.40
Peak energy for acceptor-like from E_c (eV)		0.48	0.45
Standard deviation for Gaussian states (eV)		0.15	0.15
Electron capture cross section for donor (cm^2)		10^{-14}	10^{-14}
Hole capture cross section for donor (cm^2)		10^{-15}	10^{-15}
Electron capture cross section for acceptor (cm^2)		10^{-15}	10^{-15}
Hole capture cross section for acceptor (cm^2)		10^{-14}	10^{-14}

where E represents the energy of the trap state measured from the intrinsic Fermi level E_i, τ_p and τ_n are the average carrier lifetime for holes and electrons respectively, n_{ie} the intrinsic carrier concentration, and T_L is the temperature of the lattice measured in Kelvin.

$$\mathcal{R}_{SRH} = \frac{pn - n_{ie}^2}{\tau_p\left[n + n_{ie} exp\left(\frac{E-E_i}{kT_L}\right)\right] + \tau_n\left[p + n_{ie} exp\left(-\frac{E-E_i}{kT_L}\right)\right]} \quad (4.15)$$

It is also possible for electrons in strong electric fields to tunnel from valence band to conduction band through one or more trap states. This modifies the SRH equation as shown in Eq. 4.16, where Γ_n and Γ_p are electron and hole field-effect enhancements terms. Inclusion of a trap assisted tunnelling model for materials with defects can have significant effects on the simulation of their electrical characteristics. The different transitions of carriers from the energy bands to the inner traps are shown in Fig. 4.5.

$$\mathcal{R}_{SRH} = \frac{pn - n_{ie}^2}{\frac{\tau_p}{1+\Gamma_p}\left[n + n_{ie} exp\left(\frac{E-E_i}{kT_L}\right)\right] + \frac{\tau_n}{1+\Gamma_n}\left[p + n_{ie} exp\left(-\frac{E-E_i}{kT_L}\right)\right]} \quad (4.16)$$

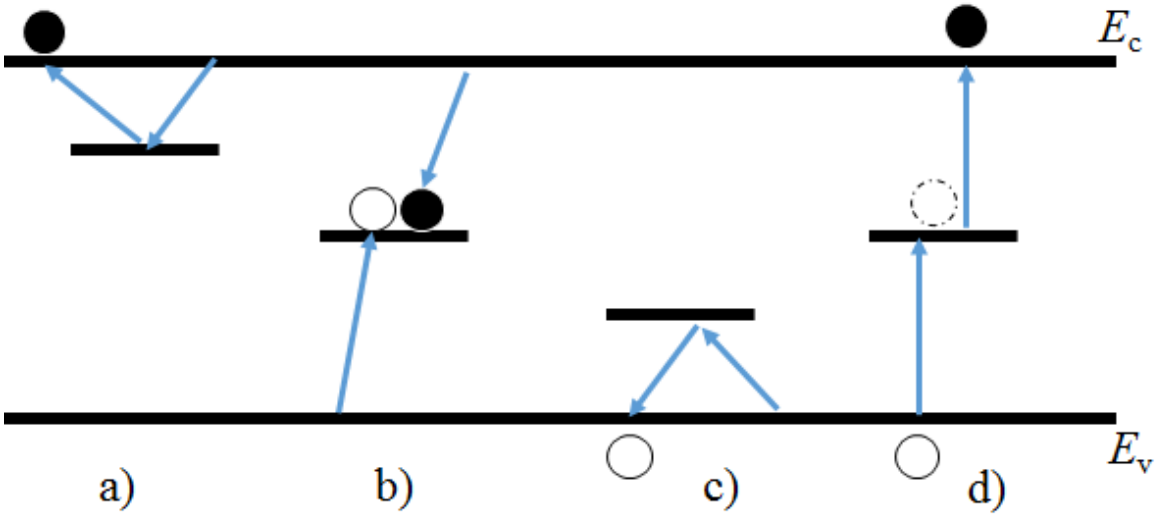

Figure 4.5. a) Trapping and de-trapping of an electron, b) recombination of electron and hole, c) trapping and de-trapping of a hole, d) trap assisted tunnelling of an electron.

The bandgap narrowing effect demonstrated in the work of Slotboom [4.33] is also included in the simulations. He showed that the *pn* product in silicon is dependent on the doping concentration, and that there is a reduction of the bandgap for doping concentrations greater than 10^{18} cm^{-3}. The modified intrinsic concentration n_{ie} is calculated in ATLAS as a function of the intrinsic concentration n_i defined in Eq. 1.7, and the change in the bandgap ΔE_g as shown in Eq. 4.17. Here, ΔE_g is fitted as shown in Eq, 4.18, where E_{BGN}=9x10^{-3} V, N_{BGN}=10^{17} cm^{-3}, and C_{BGN}=0.5 [4.34].

$$n_{ie}^2 = n_i^2 \exp\left(\frac{\Delta E_g}{kT}\right) \tag{4.17}$$

$$\Delta E_g = E_{BGN}\left\{\ln\left(\frac{N}{N_{BGN}}\right) + \sqrt{\left[\ln\left(\frac{N}{N_{BGN}}\right)\right]^2 + C_{BGN}}\right\} \tag{4.18}$$

4.3 Results

Fig. 4.6 shows the experimental $|J|$-V curves (open figures) for all ZnO/Si heterojunctions measured at room temperature (T=295 K), compared with simulations using the values from Table I (solid lines). Higher current density levels are observed for µc-Si:H(p) layer in comparison to a-Si:H(p). This is because the lower bandgap of µc-Si:H (E_g=1.124 eV) represents a lower barrier height for holes, as compared to the a-Si:H case (E_g=1.72 eV). According to Eq. 4.1 and the simulated parameters, the barrier height should be approximately Φ_{bp}=1 eV and Φ_{bp}=0.7 eV for ZnO/a-Si:H and ZnO/µc-Si:H heterojunctions, respectively. At low doping concentrations, the reverse current is orders of magnitude lower than in the forward case, and a linear region is clearly observed at low positive voltage range, before the series resistance becomes dominant. These observations are proof of the rectifying properties of the heterojunctions. Here, thermionic emission over the barrier is expected to be the dominant transport mechanism. However, as the TMB flow is increased, the linear region in the forward bias is reduced, which complicates the evaluation of diode parameters. Also, reverse current density increases up to the point where it reaches almost the same level as the forward current, producing symmetry around V=0, pointing to additional mechanisms than thermionic emission. This behaviour is reproduced

in simulations by increasing the doping concentration alone. Here, the doping concentration is varied within the range of values found in literature [$1x10^{17}$, $3x10^{19}$] cm^{-3} until a match with the experimental results is obtained, while the rest of the parameters is kept constant. The values of doping concentration obtained data are N_A=$2x10^{17}$ cm^{-3}, N_A=$9x10^{17}$ cm^{-3}, and N_A=$3x10^{18}$ cm^{-3} for the low, medium, and high doping concentrations of a-Si:H layer and N_A= 10^{17} cm^{-3}, N_A=$1.5x10^{19}$ cm^{-3}, and N_A=$3x10^{19}$ cm^{-3} for low, medium, and high doping concentrations of the µc-Si:H(p) layer, respectively. It can be seen that some of the simulated curves fit better because no attempt has been made to fit other parameters such as bandgap and density of defects with change of doping concentration. Also, it is observed that the simulated curves do not cover the entire range of values measured. The reason of this limitation is discussed in section 4.4.

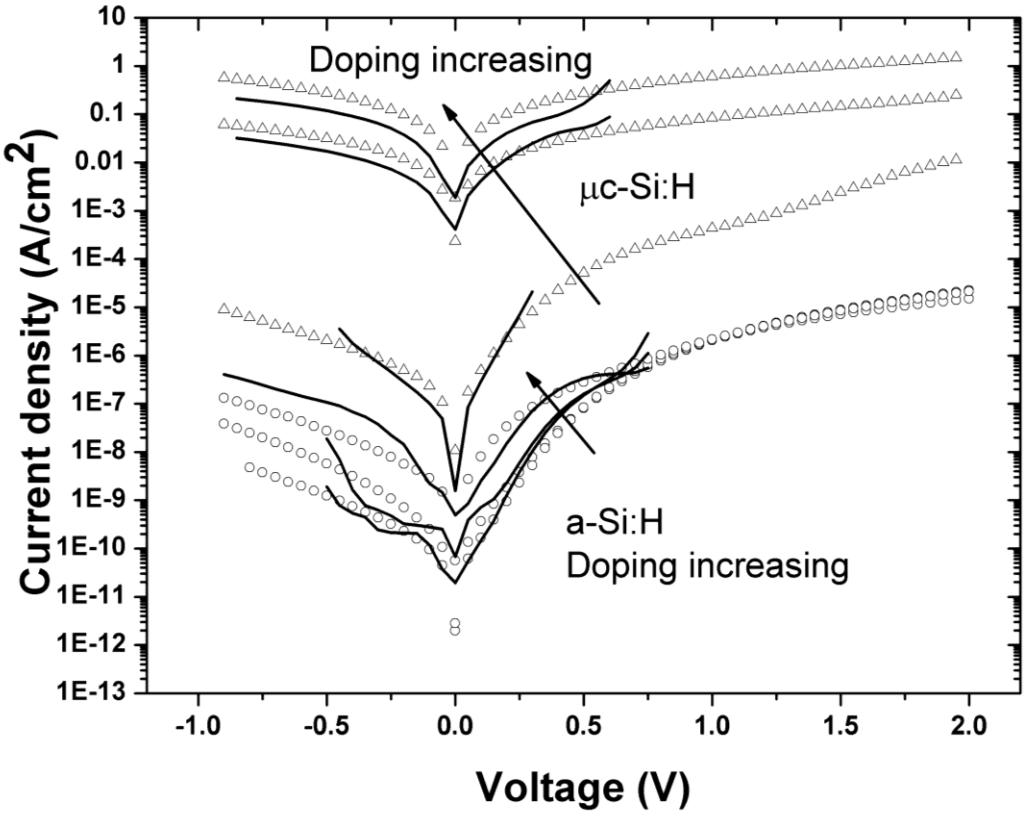

Figure 4.6. *J-V* measurements of all ZnO/µc-Si:H and ZnO/a-Si:H heterojunctions. Current density levels are increased as doping concentration is increased for all samples. The accuracy of the experimental curves depends on the level of current measured. The average accuracy for the range [10^{-14}, 10^{-1}] A is equal to 0.06%.

Schottky barrier heights extracted from simulated energy band diagrams in Fig. 4.7 for the low, medium, and high doping concentrations are 0.98 eV, 0.96 eV and 0.92 eV for the a-Si:H heterojunctions, and 0.76 eV, 0.57 eV, and 0.41 eV for µc-Si:H. The band diagram for ZnO/a-Si:H samples does not change with doping as much as for ZnO/µc-Si:H samples because of the poor doping efficiency of a-Si:H. Increasing the doping concentration has a thinning effect on the depletion region to a point where carriers are able to tunnel through the barrier irrespective of polarity, producing the symmetry around V=0.

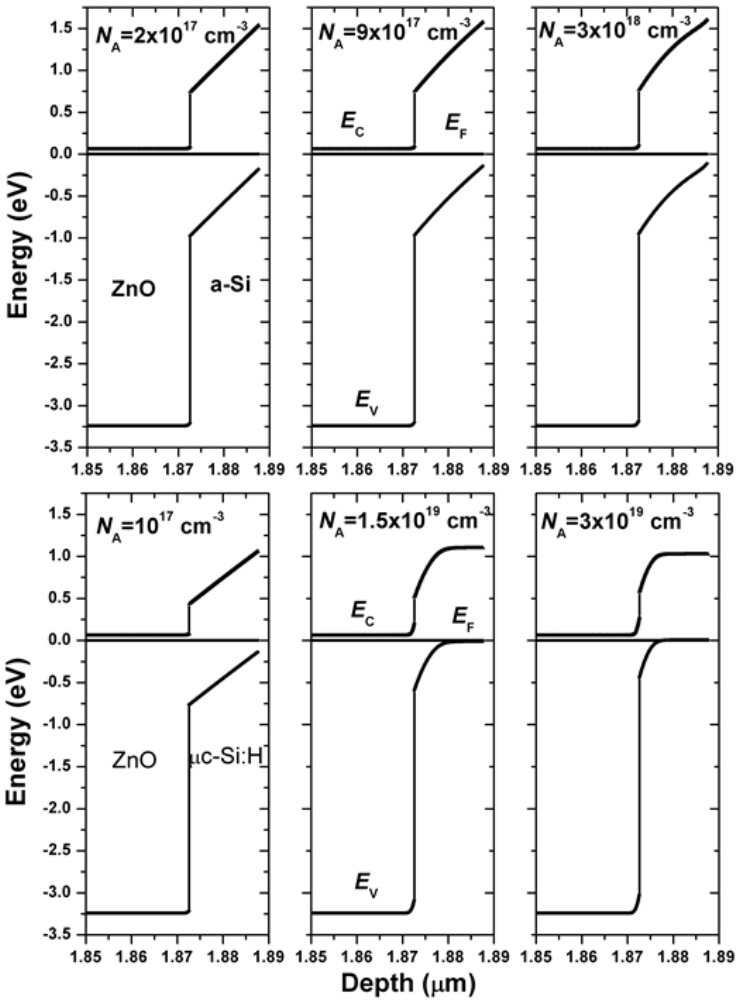

Figure 4.7. Zoomed energy band diagrams for both types of heterojunctions. Low doping of a-Si:H causes the Fermi level to remain distant from E_v and deep into E_g, which causes a low charge transfer from ZnO to a-Si:H and therefore, not enough band bending to improve tunnelling transport. For ZnO/µc-Si:H samples, a high doping of µc-Si:H reduces the effective barrier height and makes the depletion region thinner, which increases tunnelling transport.

Fig. 4.8 shows the *J-V-T* measurements performed for the ZnO/a-Si:H heterojunctions. Steep and clearly defined linear regions are observed for the sample with lowest doping concentration at all the measured temperatures. However, as the doping concentration is increased, current density at low voltages rises steeply but causes the slope of the linear region to decrease. This effect combined with the series resistance complicates the identification of the linear region. A reduction of temperature slows the rise of the *J-V* curve revealing the slope of the curve. Therefore, measurements at lower temperatures are essential for extracting the diode parameters of highly doped samples. These alterations to the curve show that the transport mechanism of the samples changes with doping and also with temperature.

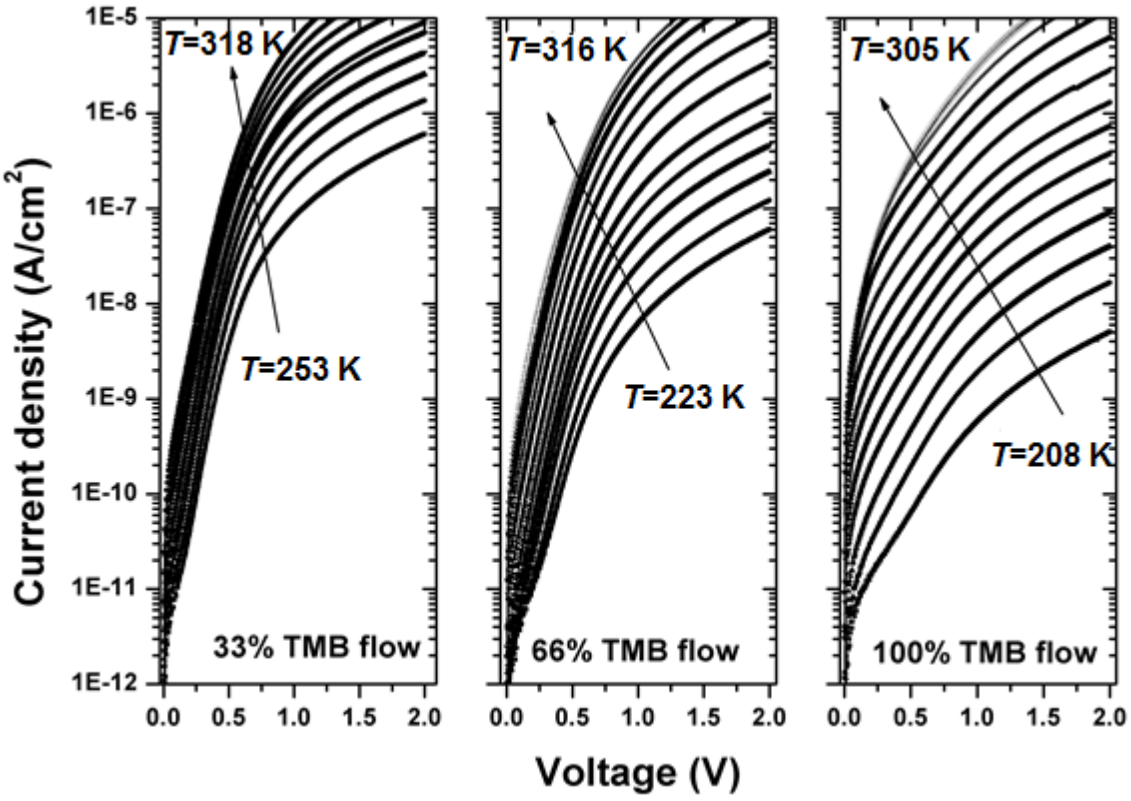

Figure 4.8 *J-V-T* forward bias measurements of ZnO/a-Si:H heterojunctions. Steeper slopes for lower doping concentrations and higher temperatures reveal the influence of thermionic emission transport mechanism. As the temperature is decreased or the doping concentration increased, contribution of multiple transport mechanisms takes effect and causes deviation of the curve from the ideal diode characteristics.

Fig. 4.9 shows that the ideality factor for the three samples decreases towards n=1 as temperature increases. This indicates that thermionic emission becomes more important and more carriers are able to jump over the barrier as the temperature is increased, nevertheless values of n>2 indicate a strong influence of field emission, thermionic field emission and leakage. At room temperature, extracted values of n=2.39, n=2.77, and n=8.85 are obtained from the experimental data for the samples with 33%, 66%, and 100% TMB flow, respectively. Also, a strong dependence of Φ_{eff} with temperature is observed from the experimental data in Fig. 4.10, indicating an increase of Φ_{eff} with temperature. The reason why Φ_{eff} changes with temperature is attributed to the multiple transport mechanisms at the interface [4.35, 4.36]. At room temperature, the values of Φ_{eff} obtained from *J-V-T* for the ZnO/a-Si:H(p) samples are 0.99 eV, 0.96 eV, and 0.82 eV for the 33%, 66%, and 100% TMB flow, respectively. The simulated and measured values of Schottky barrier for the lower and medium doping concentration are in close agreement to each other however, the measured value for the highly doped heterojunction is lower when compared to the simulated value. This occurs because the measured value represents the effective Schottky barrier height which is apparently lowered by tunnelling transport.

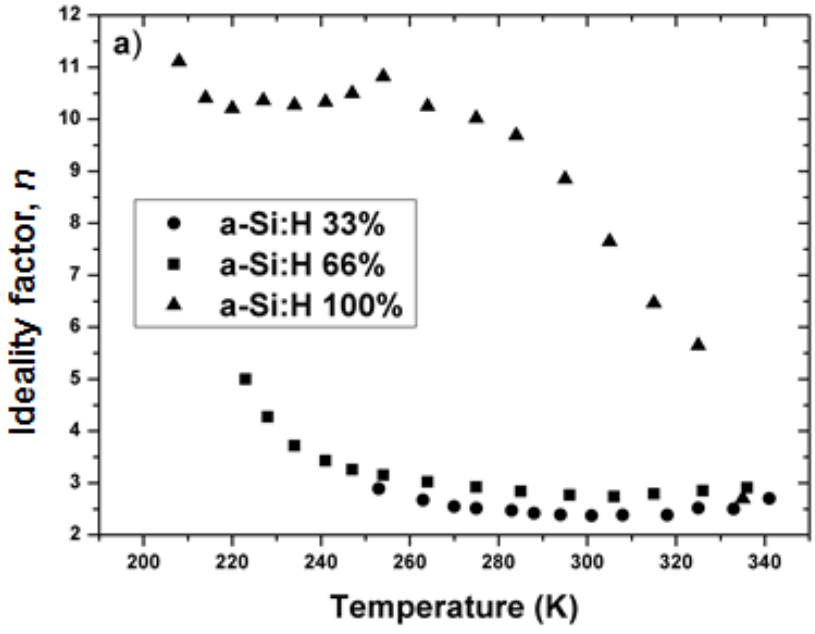

Figure 4.9. Influence of thermionic emission transport mechanism is revealed as temperature increases.

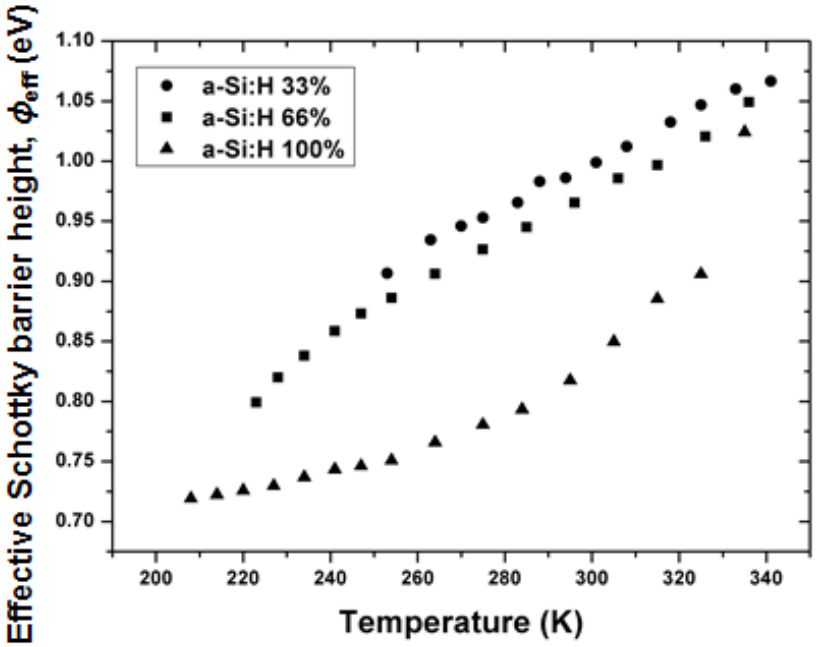

Figure 4.10. Effective Schottky barrier height as a function of temperature for the ZnO/a-Si:H(p) structures. The reduction of effective barrier as temperature decreases is attributed to contribution of transport mechanisms such as tunnelling.

The same procedure can be followed for the ZnO/µc-Si:H(p) heterojunction with the lowest doping concentration, since this is the only sample that shows a linear region from where ideality factor and saturation current can be evaluated. This time however, a weak temperature dependence is observed, as shown in Fig. 4.11, with average values of n=4. This suggests that the diode behaviour of ZnO/µc-Si:H(p) heterojunctions is inferior to that of ZnO/a-Si:H(p) heterojunctions. This agrees with the observed symmetry of the *J-V* curve around V=0, the steep rise of the *J-V* curve on low forward voltages, and the reduced Schottky barrier of Φ_{eff}=0.77 eV obtained from *J-V-T* measurements at room temperature.

The increasing symmetry of the ln|*J*|-V curve around V=0 V as the doping increases is also observed for the ZnO/µc-Si:H heterojunctions. Linear characteristics can be more easily noted for the two highest doped samples when plotted in linear scale as shown in Fig. 4.12. Since this desired behaviour is more Ohmic than rectifying, the complete loss of the linear region is understandable and calculation of the ideality factor has no motivation.

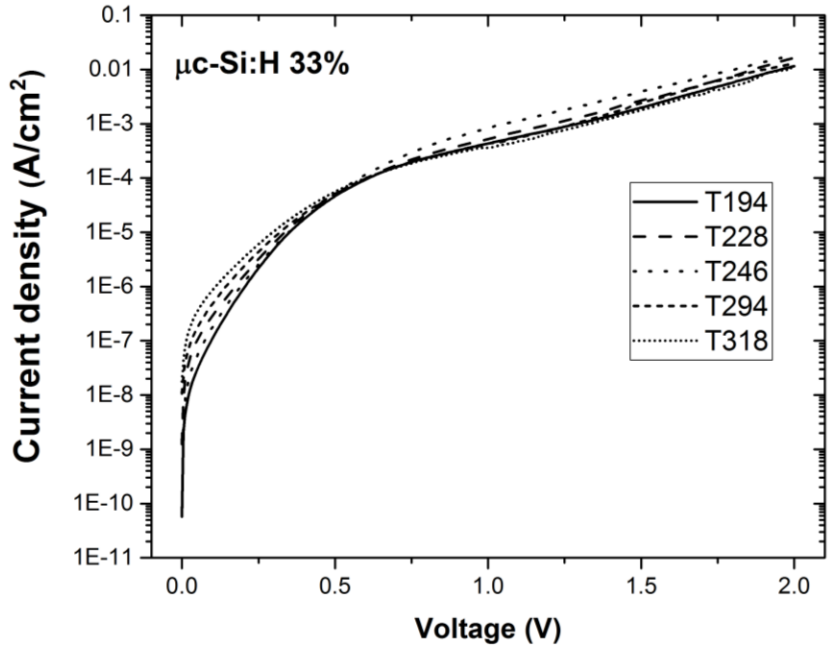

Figure 4.11. ***J-V*** **curves for ZnO/µc-Si:H samples show a weak dependence on temperature.**

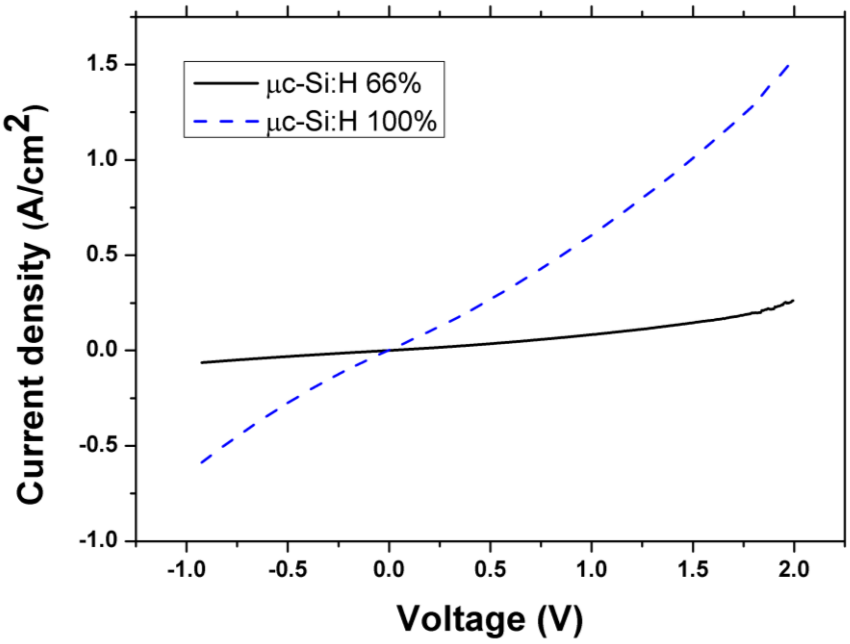

Figure 4.12. ***J-V*** **characteristics for ZnO/µc-Si:H heterojunctions with medium and higher doping concentrations in linear scale. Rectifying characteristics observed for the previous samples are no longer present on the samples with higher TMB flows. Ohmic characteristics are observed instead.**

4.4 Discussion

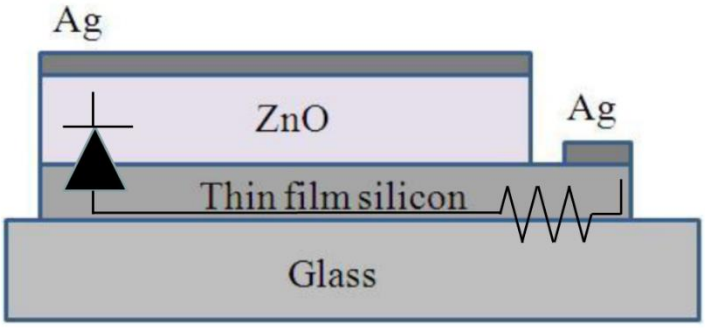

Figure 4.13. Equivalent circuit of the diode structures used for *J-V-T* measurements. The interface between ZnO and silicon represents a Schottky diode, whereas the lateral distance of silicon between contacts introduces resistive effects.

It was mentioned in section 4.3 that the range of simulation is limited, as shown in Fig. 4.6, where the simulated curve deviates from the experimental curve in the high voltage region. The reason for this limited range is due to the physical structure of the samples used to collect the experimental data. This structure can be represented by a two element electronic circuit which are, a Schottky diode introduced by the interface between ZnO and a-Si:H(p) or µc-Si:H(p), and by a series resistance introduced by the length of the p-type silicon layer as shown in Fig. 4.13. It has been mentioned that the measured thickness for ZnO and p-layer are 1.8 µm and 15 nm respectively however, the length of the p-layer from a silver contact to the other can be in the range of millimetres or even centimetres. This means that the measured *J-V* curve can be affected by the position where the measurement probes are placed. This undesired effect is only present in the high voltage region of the diode samples and not in the equivalent solar cell samples, which have a highly conductive ZnO layer at the bottom as shown in Fig. 2.12. The effect of the length of the p-layer on the *J-V* curve can be simulated by increasing the thickness of the simulated p-layer as shown in Fig. 4.14. It is observed in Fig. 4.15 that the simulated current in the high voltage region decreases as the thickness of the p-layer increases without any significant effect in the low voltage region, which is caused due to an increase of the series resistance of the sample as the thickness increases. This implies that it is possible extract the Schottky barrier height from simulated and measured *J-V* curves as long as it is evaluated from the low voltage region. Therefore, it

is more practical to limit the computer model of the diode samples to low voltages than to correct R_S in the experimental *J-V* curves in this case.

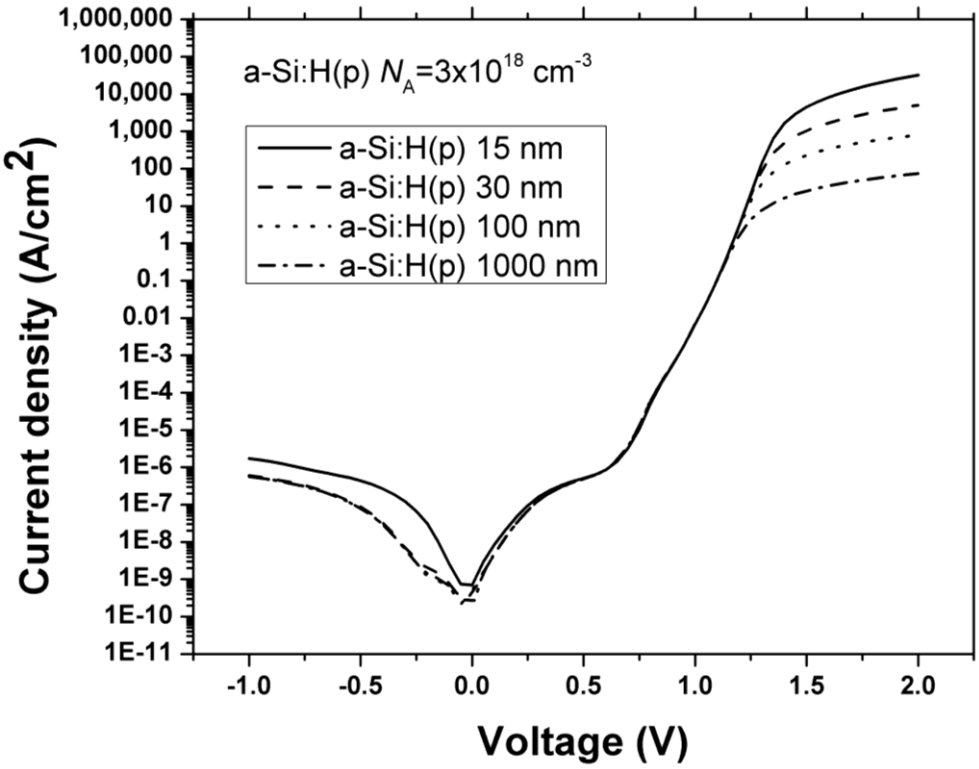

Figure 4.14. Simulated *J-V* curves for different values of thickness of a-Si:H(p). Thicker layers introduce resistive effects in the high voltage region of the curve without significant effects in the low voltage region. Other parameters for a-Si:H(p) are shown in Table 1.

An alternative explanation to the low values of current measured in the high voltage region is that the p-layer is partially or completely depleted. This can be simulated by introducing a low doping concentration in the p-layer to represent a low availability of free holes, as shown in Fig. 4.15. It is observed that a low doping concentration can approximate the magnitude of the current measured in the high voltage region however, the values of N_A simulated then become unrealistic for an a-Si:H(p) layer in a thin film silicon solar cell. Also, the shape of the *J-V* curve in the negative voltage region does not reproduce the shape observed experimentally, and the symmetry around V=0 is not evident either. Therefore, this possibility is discarded. The low values of current measured in the high voltage region are therefore attributed to the resistive effects introduced by the structure of the sample.

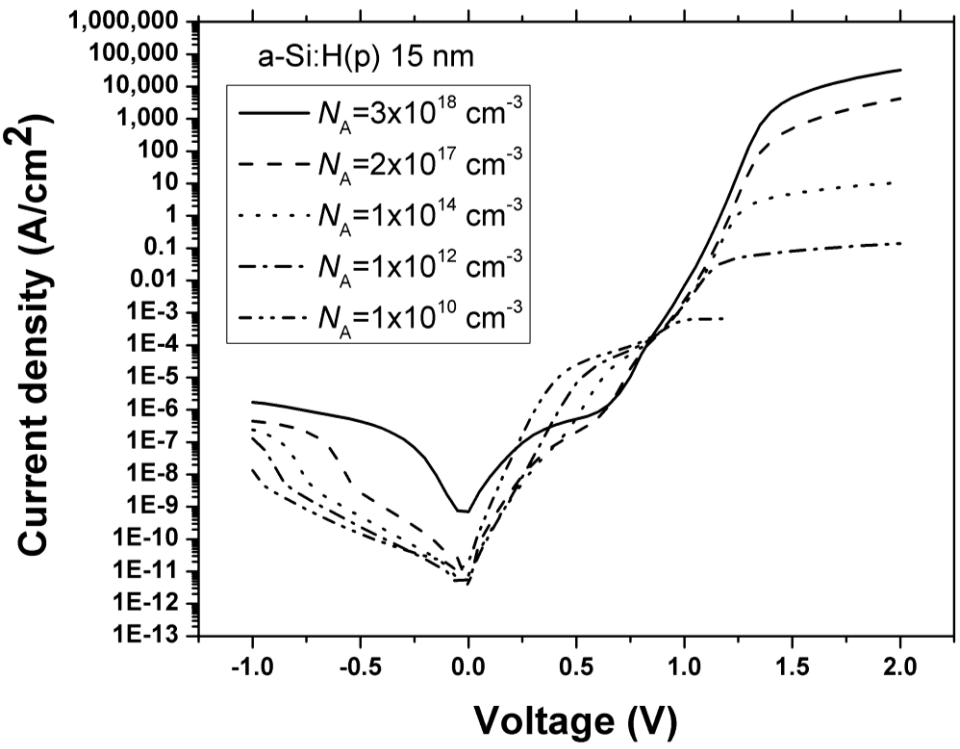

Figure 4.15. Simulated *J-V* curves as a function of doping concentration in the a-Si:H(p) layer. Other parameters for a-Si:H(p) are shown in Table 1.

4.5 Summary of Chapter 4

Chapter 4 describes the experimental results obtained by means of *J-V-T* measurements on ZnO/a-Si:H(p) and ZnO/µc-Si:H(p) diode structures. The samples demonstrate a highly resistive behaviour in the high voltage regime therefore, the extraction of the Schottky barrier height and diode ideality factor is evaluated in the low voltage regime, where the linear region of the ln|*I*|-*V* is identified. It is found that values of *n* were greater than 1, which means a deviation from thermionic emission over the barrier, due to the contribution of tunnelling transport through the barrier. Although this produces a diode with poor rectifying properties, it helps to produce an Ohmic contact, which is the type of contact desired in a solar cell. The evolution from Schottky to Ohmic is observed for both types of diode structures as the doping concentration is increased. The experimental measurements are also examined with a TCAD model that implemented the theory described in Chapter 3. Both, the experiments and simulations agree on the values of Schottky barrier height

extracted for the ZnO/a-Si:H(p) sample. On the other hand, it is not possible to measure a value of Φ_{bp} for the ZnO/µc-Si:H(p) sample with the medium and high doping concentrations, since a linear region of the ln|*I*|-*V* curve is not evident. This value is found to be approximately 0.42 eV, as evaluated from TCAD simulations. Finally, the analysis of the experiments presented in chapter 4 confirm highly doped µc-Si:H(p) to be the better contact with ZnO.

4.6 References in Chapter 4

[4.1] I. Ay and H. Tolunay, "The influence of Ohmic back contacts on the properties of a-Si:H Schottky diodes," *Solid-State Electronics*, vol. 51, no. 3. pp. 381-386, Mar-2007.

[4.2] M. W. Allen, X. Weng, J. M. Redwing, K. Sarpatwari, S. E. Mohney, H. Wenckstern, M. Grundmann and S. M. Durbin, "Temperature-Dependent Properties of Nearly Ideal ZnO Schottky Diodes," *IEEE Transactions on Electron Devices*, vol. 56, no. 9, pp. 2160-2164, Sep. 2009.

[4.3] F. Liu, M. Zhu, Y. Feng, Y. Han, J. Liu, S. Kasouit and R. Vanderhaghen, "Transport mechanism of microcrystalline silicon thin films," *Journal of Non-Crystalline Solids*, vol. 299-302, pp. 385-389, Apr. 2002.

[4.4] S. II Park, S. Jae Baik, J.S. Im, L. Fang, J.W. Jeon, and K. Su Lim, "Towards a high efficiency amorphous silicon solar cell using molybdenum oxide as a window layer instead of conventional p-type amorphous silicon carbide," *Appl. Phys. Lett.*, vol. 99, no. 6, p. 063504, 2011.

[4.5] M. Kubon, E. Boehmer, M. Gastel, F. Siebke, W. Beyer, C. Beneking, and H. Wagner in Photovoltaic Energy Conversion, Conference Record of the Twenty Fourth. IEEE Photovoltaic Specialists Conference (1994). IEEE First World Conference on Photovoltaic Energy Conversion, 5-9 Dec 1994

[4.6] M. Kubon, E. Boehmer, F. Siebke, B. Rech, C. Beneking, and H. Wagner, "Solution of the ZnO/p contact problem in a-Si:H solar cells," *Sol. Energy Mater. Sol. Cells*, vol. 41–42, pp. 485–492, Jun. 1996.

[4.7] J. Kim, A. I. Abou-Kandil, A. J. Hong, M. M. Saad, D. K. Sadana, and T.-C. Chen, "Efficiency enhancement of a-Si:H single junction solar cells by a-Ge:H incorporation at the p+ a-SiC:H/transparent conducting oxide interface," *Appl. Phys. Lett.*, vol. 99, no. 6, p. 062102, 2011.

[4.8] G. Ganguly, D. E. Carlson, S. S. Hegedus, D. Ryan, R. G. Gordon, D. Pang, and R. C. Reedy, "Improved fill factors in amorphous silicon solar cells on zinc oxide by insertion of a germanium layer to block impurity incorporation," *Appl. Phys. Lett.*, vol. 85, no. 3, p. 479, 2004.

[4.9] J-S Im, J-W Jeon, S. Park, Y. Lee, and K.S. Lim in Photovoltaic Specialists Conference (PVSC), 612 (2011). 37th IEEE Photovoltaic Specialists Conference (PVSC), Seattle, USA, 19-24 Jun 2011.

[4.10] J. Kim, A. Abou-Kandil, K. Fogel, H. Hovel, and D. K. Sadana, "The role of high work-function metallic nanodots on the performance of a-Si:H solar cells: offering Ohmic contact to light trapping.," *ACS Nano*, vol. 4, no. 12, pp. 7331–6, Dec. 2010.

[4.11] P.-K. Chang, P.-T. Hsieh, C.-H. Lu, C.-H. Yeh, and M.-P. Houng, "Development of high efficiency p–i–n amorphous silicon solar cells with the p-μc-Si:H/p-a-SiC:H double window layer," *Sol. Energy Mater. Sol. Cells*, vol. 95, no. 9, pp. 2659–2663, Sep. 2011.

[4.12] C-H Lin, J-H Liu, and I. M. Chan in Photovoltaic Specialists Conference (PVSC), 3038 (2011). 37th IEEE Photovoltaic Specialists Conference (PVSC), Seattle, USA, 19-24 Jun 2011.

[4.13] F. Vaianella, G. Rosolen, and B. Maes, "Graphene as a transparent electrode for amorphous silicon-based solar cells," *J. Appl. Phys.*, vol. 117, no. 24, p. 243102, 2015.

[4.14] C. Ke, I. M. Peters, N. Sahraei, A. G. Aberle, and R. Stangl, "On the use of a charged tunnel layer as a hole collector to improve the efficiency of amorphous silicon thin-film solar cells," *J. Appl. Phys.*, vol. 117, no. 24, p. 245701, 2015.

[4.15] A. N. Corpus-mendoza, M. M. De Souza, and F. Hamelmann, "Transport mechanisms and effective Schottky barrier height of ZnO / a-Si : H and ZnO / μc-Si : H heterojunction solar cells," *J. Appl. Phys.*, vol. 184505, 2013.

[4.16] F. A. Padovani and R. Stratton, "Field and thermionic-field emission in Schottky barriers," *Solid-State Electronics*, vol 9, no. 7, pp. 695-707, 1966

[4.17] Silvaco, "ATLAS user's manual. Device simulation software," pp. 23, May. 2009.

[4.18] A. Fantoni, "Simulation of hydrogenated amorphous and microcrystalline silicon optoelectronic devices," *Mathematics and Computers in Simulation*, vol. 49, no. 4-5, pp. 381-401, Sep. 1999.

[4.19] N. Hernández-Como and A. Morales-Acevedo, "Simulation of hetero-junction silicon solar cells with AMPS-1D," *Solar Energy Materials and Solar Cells*, vol. 94, no. 1, pp. 62-67, Jan. 2010.

[4.20] K. Ding, T. Kirchartz, B. Pieters, C. Ulbrich, A. Ermes, S. Schicho, A. Lambertz, R. Carius and U. Rau, "Characterization and simulation of a-Si:H/μc-Si:H tandem solar cells," *Solar Energy Materials and Solar Cells*, vol. 95, no. 12, pp. 3318-3327, Dec. 2011.

[4.21] A. Fantoni, M. Vieira, R. Martins, "Transport properties in microcrystalline silicon solar cells under AM1.5 illumination analysed by two dimensional numerical simulation," *Solid-State Electronics*, vol. 43, no. 9, pp. 1709-1714, Sep. 1999.

[4.22] J. Yuan, H. Shen, L. Lu, T. Wu, and X. He, "Simulation of HIT solar cells with μc-3C-SiC:H emitter," *Optoelectronics and Advanced Materials*, vol. 4, no. 8, pp. 1211-1214, 2010.

[4.23] J. S. C. Prentice, "The effect of surface states at the SnO_2/p-a-Si:H interface," *Journal of Non-Crystalline Solids*, vol. 262, no. 2000, pp. 99-105, 2006.

[4.24] M. I. Kabir, N. Amin, A. Zaharim, and K. Sopian, "Effect of energy bandgap of the amorphous silicon carbide (a-SiC:H) layers on a-Si multijuntion solar cells from numerical analysis," *Systems Engineering*, pp. 334-337.

[4.25] G. Cannella, F. Principato, M. Foti, S. Di Marco, a. Grasso, and S. Lombardo, "Carrier transport mechanism in the SnO_2:F/p-type a-Si:H heterojunction," *Journal of Applied Physics*, vol. 110, no. 2, p. 024502, 2011.

[4.26] F. Smole, M. Topie, and J. Furlan, "Analysis of TCO / p (a-Si:C:H) heterojunction and its influence on p-i-n a-Si:H solar cell performance," *Journal of Non-Crystalline Solids*, vol. 194, pp. 312-318, 1996.

[4.27] S. Miyajima, J. Irikawa, A. Yamada, and M. Konagai, "Modeling and simulation of heterojunction crystalline silicon solar cells with a nanocrystalline cubic silicon carbide emitter," *Journal of Applied Physics*, vol. 109, no. 5, p. 054507, 2011.

[4.28] M. W. M. van Cleef, J. K. Rath, F. a. Rubinelli, C. H. M. van der Werf, R. E. I. Schropp, and W. F. van der Weg, "Performance of heterojunction p^+ microcrystalline silicon n crystalline silicon solar cells," *Journal of Applied Physics*, vol. 82, no. 12, p. 6089, 1997.

[4.29] M. Vukadinović, F. Smole, M. Topič, R. E. I. Schropp, and F. a. Rubinelli, "Transport in tunneling recombination junctions: A combined computer simulation study," *Journal of Applied Physics*, vol. 96, no. 12, p. 7289, 2004.

[4.30] K. Ding et al., "Characterization and simulation of a-Si:H/μc-Si:H tandem solar cells," *Solar Energy Materials and Solar Cells*, vol. 95, no. 12, pp. 3318-3327, Dec. 2011.

[4.31] M. Nath, P. Roca i Cabarrocas, E. V. Johnson, a. Abramov, and P. Chatterjee, "The open-circuit voltage in microcrystalline silicon solar cells of different degrees of crystallinity," *Thin Solid Films*, vol. 516, no. 20, pp. 6974-6978, Aug. 2008.

[4.32] B. E. Pieters, H. Stiebig, M. Zeman, and R. a. C. M. M. van Swaaij, "Determination of the mobility gap of intrinsic μc-Si:H in p-i-n solar cells," *Journal of Applied Physics*, vol. 105, no. 4, p. 044502, 2009.

[4.33] J. W. Slotboom, "The PN product in silicon," *Solid State Electronics*, vol. 20, pp. 279-283, 1977.

[4.34] J. W. Slotboom, and H. C. De Graaf, "Measurements of bandgap narrowing in silicon bipolar transistors," *Solid State Electronics*, vol. 19, pp. 857-862, 1976.

[4.35] D. Donoval, V. Drobny, and M. Luza, "A contribution to the analysis of the I-V characteristics of Schottky structures," *Solid. State. Electron.*, vol. 42, no. 2, pp. 235–241, 1998.

[4.36] D. Donoval, M. Barus, and M. Zdimal, "Analysis of I-V measurements on PtSi-Si Schottky structures in a wide temperature range," *Solid State Electronics*, vol. 34, no. 12, pp. 1365-1373, 1991

Chapter 5.

Design of TCO/a:Si interfaces for optimum performance of solar cells

The heterojunctions shown in the previous chapter are used as window layers for thin film silicon solar cells. It is found that despite better contact properties of µc-Si:H(p) with ZnO, its energy band misalignment with the a-Si:H(i) layer reduces the performance of the solar cell. A simulation study and fabrication of a µc-Si:H(p)/a-Si:H(p) layer is shown that optimizes the performance of the solar cell.

In this chapter, a full-scale model of thin-film silicon solar cells with non-ideal contacts is validated with TCAD simulations, circuit simulations and experimental measurements. It is shown that the V_{OC} of a solar cell is considerably reduced due to a kink in its *J-V* characteristics that results from the existence of a Schottky contact with a barrier height greater than 0.5 eV when thermionic emission is the dominant transport mechanism. Different practical approaches have been implemented in order to reduce this barrier height. Some examples include the introduction of interlayer materials at the TCO/p-type Si interface such as μc-Si:H [5.1 - 5.3], amorphous hydrogenated germanium [5.4], amorphous tungsten oxide [5.5], and a high-work function metal nanodots [5.6]. A more common approach consists in allowing tunnelling transport mechanism at the interface by increasing the doping concentration of the semiconductor. However, this Schottky barrier is often ignored for modelling and simulation studies of solar cells.

A circuit model implemented by Niemegeers on CdTe cells [5.7], is one of the few exceptions that considers Schottky contacts in solar cells. This work demonstrates a model of the Au/CdTe contact as a Schottky diode and the entire solar cell structure as two diodes connected back-to-back. This model explains the saturation of current measured at high forward bias for CdTe solar cells under the assumption of thermionic emission dominating the transport across the back contact however, the model neglects the effect of tunnelling through the barrier height, which can have a significant effect on other technologies such as thin-film silicon. Although the effect of tunnelling has been previously considered for heterojunction solar cells by Kanevce [5.8] and for a-Si:H thin film solar cells by Arch and Rubinelli [5.9, 5.10], a complete model indicating the impact of the different discontinuities found at the interfaces of the window layer with the contact and the main junction, or at the interfaces of the interlayer between contact and semiconductor, has been missing. The understanding of these interfaces is critical for the correct optimization of solar cells. The results presented here are not limited to thin film solar cells only, and can be extended to other solar cell technologies where the use of an Ohmic contact is not yet possible, especially heterojunction solar cells. The content presented in this chapter has been published in [5.11].

5.1 Methodology for evaluation of thin film silicon solar cells

The ZnO/a-Si:H(p) and ZnO/µc-Si:H(p) interfaces presented in chapter 4 of this thesis were implemented as window layers for solar cells of area 1cm^2 with the structure ZnO/p-layer/a-Si:H(i)/a-Si:H(n)/ZnO/Ag shown in Fig. 5.1. These layers had a thickness of 1800, 15, 220, 25 and 1500 nm respectively, with a tolerance of ±20%, where the p-layer was made of 1) a-Si:H(p), or 2) µc-Si:H(p). A third type of p-layer made of µc-Si:H(p)/a-Si:H(p) was also tested as a window layer. All the cells were mounted on soda lime glass. The analysis of the circuit shown in Fig. 5.1 is explained in section 2.3, whereas the fabrication details are described in section 2.6.

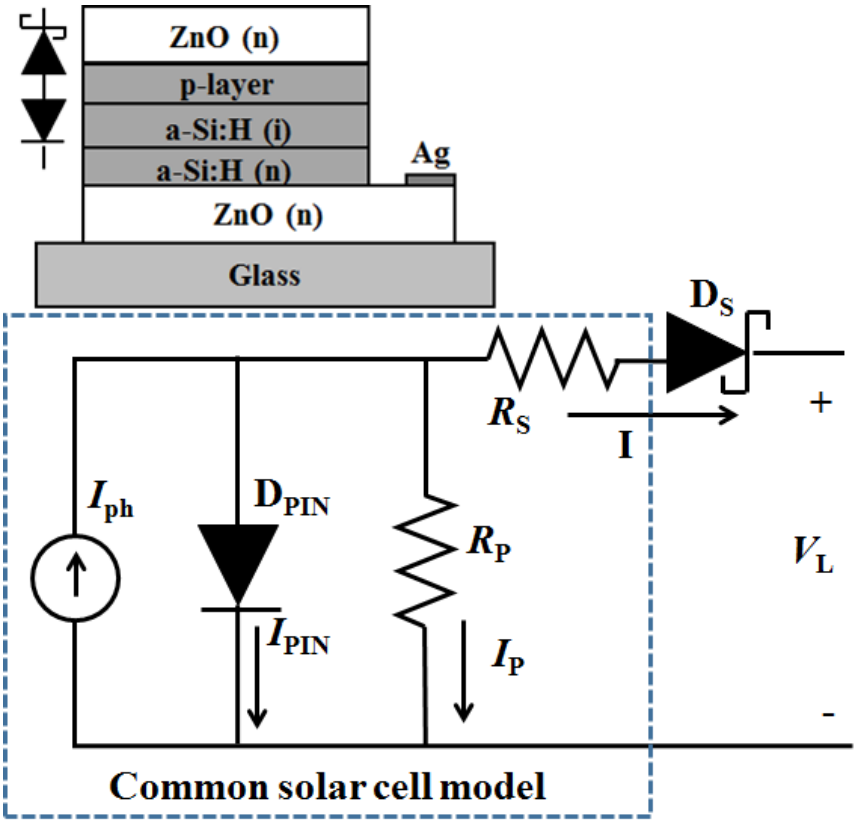

Figure 5.1. Schematic diagram of the structure of a solar cell which shows the main junction p-i-n diode and the ZnO/a-Si:H(p) diode. The p-layer can be a-Si:H(p), µc-Si:H(p) or a µc-Si:H(p)/a-Si:H(p) mixture. Also, the conventional equivalent circuit of a solar cell used to model the *J-V* characteristics is shown. In this work, an additional Schottky barrier contact D_S is included.

Fig. 5.1 shows the complete equivalent electronic circuit of a solar cell, where an improperly fabricated contact to the doped layers represents a Schottky diode D_S in series with the main junction of the cell. As a consequence of the Schottky contact, there is a drop of voltage across the interface that affects the *FF* and V_{OC}.

This back-to-back diode configuration has been previously used to represent the main junction and back contact of CdTe/metal solar cells and to explain the rollover characteristics of their *J-V* curve [5.7, 5.12, 5.13]. It has also been implemented as a PSPICE model to study the ITO/a-Si:H(p) and a-Si:H(p)/c-Si(n) junctions in heterojunction solar cells [5.8]. In the studies cited above, it has been assumed that thermionic emission is the dominant transport mechanism of the Schottky diode, neglecting other forms of transport such as tunnelling. Additionally, Demtsu included a shunt resistance for the Schottky contact that represents the degree of rollover of the *J-V* curve [5.7]. This shunt resistance is not included in the model presented here, since the solar cells measured did not show rollover characteristics.

5.2 Computer simulations

The methodology, program and models used to simulate the semiconductor structures are described in section 4.2. This time however, the complete solar cell structure was simulated. The simulations for the solar cells with the three different types of window layer were matched to the experimental curves after applying the correction for R_S described in Chapter 2. The temperature of measurement and simulation was always room temperature.

For these simulations, the ZnO layer was simulated as a metal in order to produce a Schottky diode with the p-layer and study the effects of different Schottky barrier heights. On the other hand, the ZnO/n-layer interface at the bottom of the cell was considered to be an Ohmic contact. Here, the Universal Schottky Tunnelling (UST) model [5.14, 5.15] is included since a key objective of this study is to consider the impact of tunnelling transport at the Schottky interface. The advantage of this model is that it includes the contribution of both, thermionic emission (I_{TE}) and field-emission (I_{TU}) currents at the contact node (see Fig. 5.2) as well as the transition from Schottky to Ohmic as the doping concentration is increased.

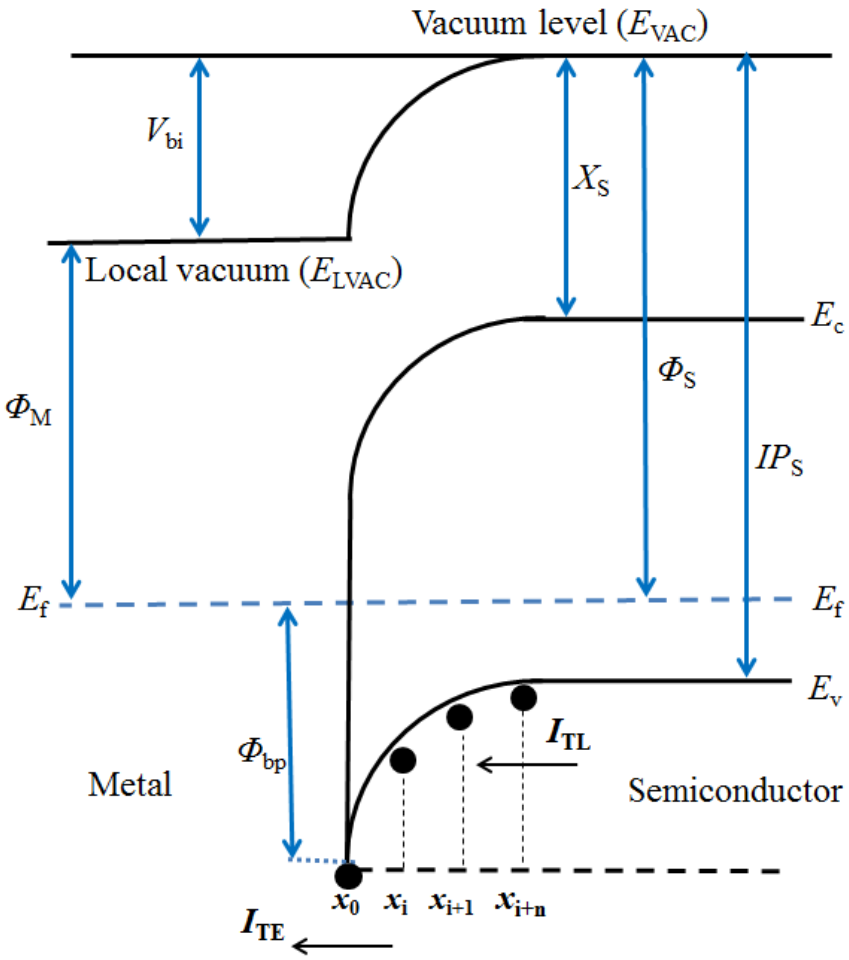

Figure 5.2. Metal/p-type semiconductor interface. Holes can travel from the semiconductor side to the contact by overcoming the barrier via thermionic emission (TE) or by tunnelling through the barrier (TL). I_{TE} is represented by localized tunnelling rates at different positions x_i.

The equations for I_{TE} and I_{TU} for a degenerate doping level are shown in Eq. 5.1 and Eq. 5.2, where A is the area of the device, f_s and f_m are the Maxwell-Boltzmann distribution functions for semiconductor and metal respectively, ξ the carrier energy and $\Delta\Phi_{bp}$ a barrier lowering term. I_{TU} is solved locally at grid locations x_i, that are near to the Schottky junction, as shown in Fig. 5.2. Here $\Delta\xi$ represents the energy difference calculated at a position x, and T_{TL} is the tunnelling probability as shown in Eq. 5.3, where m^* is the effective mass and ħ the reduced Planck constant.

$$I_{TE} = \frac{AA^{**}T}{k}\int_{\xi_0-q\Delta\Phi_{bp}}^{\infty} \ln\left(\frac{1+f_s(\xi)}{1+f_m(\xi)}\right) d\xi \qquad (5.1)$$

$$I_{\mathrm{TU}}(x) = \frac{AA^{**}T}{\mathrm{k}} \int_{\xi - \Delta\xi/2}^{\xi + \Delta\xi/2} T_{\mathrm{TL}}(\xi) \ln\left(\frac{1+f_s(\xi)}{1+f_m(\xi)}\right) d\xi \tag{5.2}$$

$$T_{\mathrm{TL}}(\xi) = exp\left[-\frac{4\sqrt{2m^*}(q\Phi_{\mathrm{bp}} - \xi)^{1.5}}{3\hbar q|E|}\right] \tag{5.3}$$

Finally, transport of electron-hole pairs generated in the intrinsic region and recombination in the bulk are simulated with the drift-diffusion [5.16] and Shockley-Read-Hall [5.17, 5.18] models. Bandgap narrowing of silicon layers due to high concentrations of p-type dopants is considered once again. The silicon layers were represented with a continuous density of states (DOS), which is composed of exponential functions as band tails entering into the bandgap and Gaussian distributions in the middle of the gap that represent dangling bonds of amorphous materials, as described in Chapter 4. A complete list of parameters used to define the different material layers found in the cell is shown in Table 2. These values are commonly found in the literature and in their majority, consistent with the previously published chapter [5.19]. However, some parameters such as the peak density of Gaussian and band tail states for a-Si:H(p) and µc-Si:H(p) are simulated here with larger values than those used in chapter 4. This is because only the p-layers with higher doping concentration are simulated here, and it is known that a high concentration of dopants leads to the creation of midgap states and to an extra disorder in the structure [5.20]. The effect that doping and other parameters not shown in this chapter can have on the *J-V* curve of the solar cell is shown in the appendix.

5.3 Results

Fig. 5.3. shows the simulated and experimental *J-V* curves of thin film silicon solar cells with a-Si:H(p), µc-Si:H(p) and µc-Si:H(p)/a-Si:H(p) layers. The series resistance of the experimental curves was calculated as explained using the methodology in Chapter 2, and the current was plotted as a function of $V+IR_S$ in order to compare the simulated and experimental data. It is observed that the value of J_{SC} reduces when µc-Si:H(p) is used as a

Table 2. List of parameters used for TCAD simulations of solar cells. A description of the parameters used to simulate the DOS (tail and Gaussian states) is included in section 4.2.2.

Parameter	*μc-Si:H(p)*	*a-Si:H(p)*	*a-Si:H(i)*	*a-Si:H(n)*
Thickness (nm)	15	15	220	25
Donor concentration (cm^{-3})				$3x10^{18}$
Acceptor concentration (cm^{-3})	$3x10^{19}$	$4.5x10^{18}$		
Bandgap (eV)	1.124	1.72	1.72	1.72
Electron affinity (eV)	4	3.7	3.7	3.7
Effective density of states for E_c (cm^{-3})	$4.8x10^{19}$	$2.5x10^{20}$	$2.5x10^{20}$	$2.5x10^{20}$
Effective density of states for E_v (cm^{-3})	$2.4x10^{19}$	$2.5x10^{20}$	$2.5x10^{20}$	$2.5x10^{20}$
Electron mobility ($cm^2\ V^{-1}\ s^{-1}$)	20	10	10	10
Hole mobility ($cm^2\ V^{-1}\ s^{-1}$)	5	1	1	1
Band tail states				
Peak density of states (acceptors) ($cm^{-3}\ eV^{-1}$)	$9.6x10^{19}$	$2x10^{21}$	$2x10^{21}$	$2x10^{21}$
Peak density of states for donors ($cm^{-3}\ eV^{-1}$)	$4.8x10^{19}$	$2x10^{21}$	$2x10^{21}$	$2x10^{21}$
Characteristic decay energy for tail states of the conduction band (eV)	0.031	0.03	0.03	0.03
Characteristic decay energy for tail states of the valence band (eV)	0.031	0.049	0.049	0.049
Electron capture cross section for donors (cm^2)	$2.5x10^{-15}$	$2.5x10^{-15}$	$2.5x10^{-15}$	$2.5x10^{-15}$
Hole capture cross section for donors (cm^2)	$2.1x10^{-17}$	$2.1x10^{-17}$	$2.1x10^{-17}$	$2.1x10^{-17}$
Electron capture cross section for acceptors (cm^2)	$2.1x10^{-17}$	$2.1x10^{-17}$	$2.1x10^{-17}$	$2.1x10^{-17}$
Hole capture cross section for acceptors (cm^2)	$2.5x10^{-15}$	$2.5x10^{-15}$	$2.5x10^{-15}$	$2.5x10^{-15}$
Gaussian states				
Peak density of states (acceptors) ($cm^{-3}eV^{-1}$)	$3x10^{18}$	$3x10^{18}$	$3x10^{16}$	$3x10^{18}$
Peak density of states (donors) ($cm^{-3}eV^{-1}$)	$3x10^{18}$	$3x10^{18}$	$3x10^{16}$	$3x10^{18}$
Peak energy for donor-like from E_v (eV)	0.40	0.48	0.57	0.57
Peak energy for acceptor-like from E_c (eV)	0.45	0.48	0.57	0.57
Standard deviation for Gaussian states (eV)	0.15	0.15	0.15	0.15
Electron capture cross section for donor (cm^2)	10^{-14}	10^{-14}	10^{-14}	10^{-14}
Hole capture cross section for donor (cm^2)	10^{-15}	10^{-15}	10^{-15}	10^{-15}
Electron capture cross section for acceptor (cm^2)	10^{-15}	10^{-15}	10^{-15}	10^{-15}
Hole capture cross section for acceptor (cm^2)	10^{-14}	10^{-14}	10^{-14}	10^{-14}

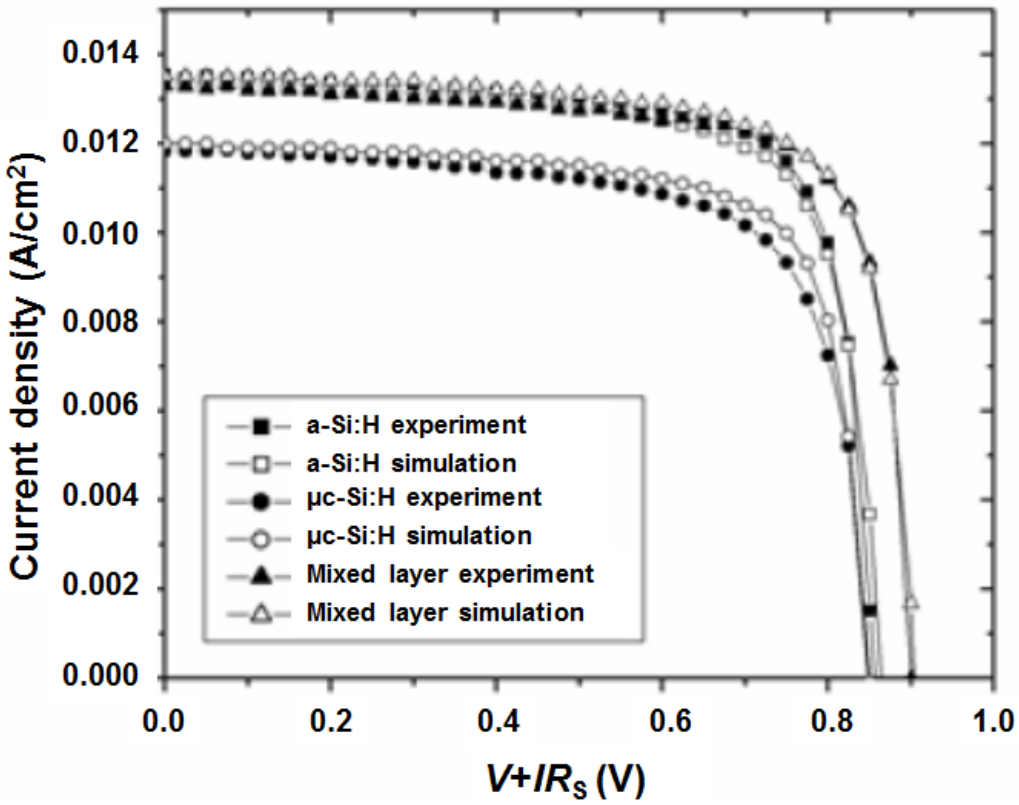

Figure 5.3. *J-V* measurements for a-Si:H solar cells with a-Si:H(p), µc-Si:H(p) and mixed µc-Si:H(p)/a-Si:H(p) window layers. Despite the better contact properties of µc-Si:H(p) with ZnO, a lesser performance is obtained for cells with a µc-Si:H(p) window layer due to a narrower bandgap that reduces J_{SC}.

window layer as a consequence of a narrower bandgap compared to that of a-Si:H(p), which prevents light from reaching the absorbing layer. On the other hand, the variations of V_{OC} for the cells with different p-type layers are explained by analysing Fig. 5.4. The band diagram for a ZnO/p-layer interface with ideal Ohmic contacts is shown in Fig. 5.4a), whereas Fig. 5.4b) and 5.4c) indicate an actual Schottky contact with ZnO when µc-Si:H(p) and a-Si:H(p) are used as window layers respectively. The case of a combined µc-Si:H(p)/a-Si:H(p) window layer is also shown in Fig. 5.4d). Figures 5.4a) and 5.4b) have been shown in [5.10] however, examples 5.4c) and 5.4d) have not, where a discontinuity exists at the p/i interface or materials with different bandgaps are used, respectively. The inclusion of 5.4c) and 5.4d) allows a broader optimization study of window layers for thin film silicon solar cells.

Ideally, the contact should be as in 4a), where the offset between the ZnO contact and the valence band of the p-type layer is minimal, which implies a low Schottky barrier height. This is simulated by declaring an Ohmic interface for the contact, which automatically adjusts the contact work function to avoid an offset with the p-layer. A comparison of the band diagram between 5.4b) µc-Si:H(p) and 5.4c) a-Si:H(p) window layers shows the former to produce better contact with the ZnO layer due to a reduced Schottky barrier height of Φ_{bp}=0.45 eV, compared to Φ_{bp}=0.75 eV for the a-Si:H(p) case. However, even though the ZnO/µc-Si:H(p) interface produces better contact properties than the ZnO/a-Si:H(p) interface, the cell using a µc-Si:H(p) window layer shows the lowest V_{OC} of the measured and simulated samples, and the reason for this drop of voltage can be explained as a consequence of the valence band offset between the µc-Si:H(p) a-Si:H(i) layers [5.21]. This misalignment at the p/i interface is not present for the a-Si:H(p) window layers. Therefore, there is a trade-off between producing a good quality ZnO/p or a p/i interface. Since µc-Si:H(p) produces a better contact with ZnO than a-Si:H(p), but a-Si:H(p) makes a better interface with the i-layer than µc-Si:H(p), it is natural to obtain the best cell performance by implementing a mixed µc-Si:H(p)/a-Si:H(p) window layer.

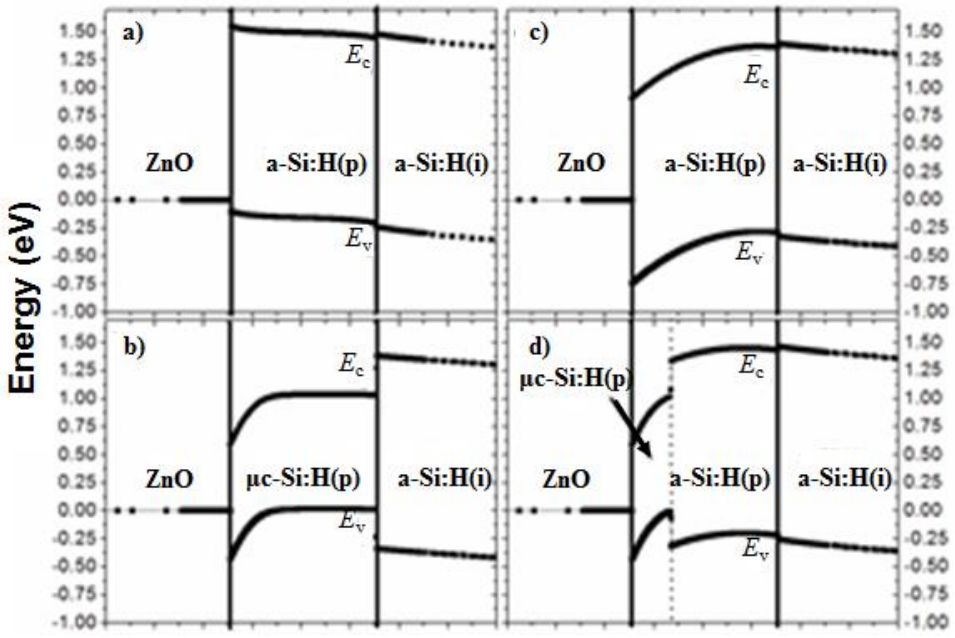

Figure 5.4. Energy Band diagrams of an a) Ideal ZnO/p-layer Ohmic interface, b) Actual ZnO/µc-Si:H(p) Schottky interface and c) Actual ZnO/a-Si:H(p) interface. A combined µc-Si:H(p)/a-Si:H(p) layer is shown in d).

The *J-V* curve and energy band diagram for the cell with mixed window layers are shown in Fig. 5.3 and Fig. 5.4d) respectively. In this case, an optimized µc-Si:H(p)/a-Si:H(p) thickness ratio allows a low barrier height when in contact with the ZnO layer without compromising the p/i interface hence, achieving higher V_{OC}. The simulated value of V_{OC} reaches a maximum for a 4 nm /11 nm µc-Si:H(p)/a-Si:H(p) thickness ratio when the sum of thicknesses of both materials that form the p-layer is equal to 15 nm, as shown in Fig. 5.5. Here, the value of 15 nm is used since it is the measured thickness of the p-layer therefore, the simulated µc-Si:H(p)/a-Si:H(p) ratio is varied as X/(15-X) where X is the µc-Si:H(p) thickness in nm. A thicker p-layer could increase the V_{OC} of the cell due to an increase of the electric field however, this would also obstruct the light from reaching the a-Si:H(i) layer, which would decrease J_{SC}. Furthermore, extending the µc-Si:H(p) or a-Si:H(p) sections in a mixed p-layer could negatively affect the tunnelling transport and reduce the *FF* of the cell.

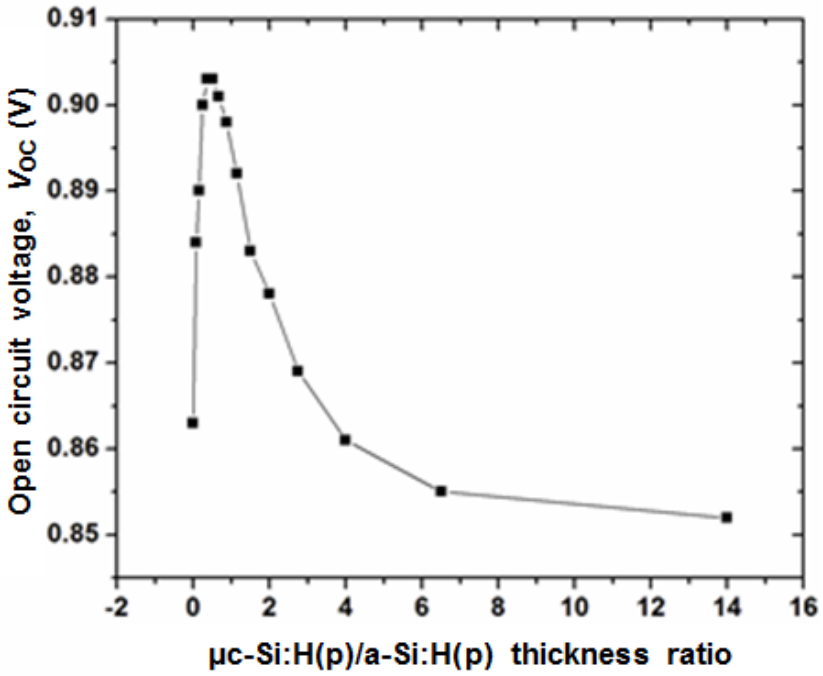

Figure 5.5. Open circuit voltage for the cell with µc-Si:H(p)/a-Si:H(p) layer as a function of the µc-Si:H(p)/a-Si:H(p) thickness ratio when the p-layer is 15 nm thick.

Simulation studies of a-Si:H solar cells often assume perfectly Ohmic contacts to the semiconductor layer and ignore the detrimental effects of the ZnO/p-type interface.

Therefore, it is of significant interest to investigate the performance of the solar cell as a function of the Schottky barrier height of the contact. Here, the value of surface recombination used was 10^7 cm/s due to the large quantity of dangling bonds at the surface of a-Si [5.8]. It can be seen in Fig. 5.6 and Fig. 5.7 that increasing the barrier height from the Ohmic case to 1 eV has a detrimental effect on the V_{OC} of the cell. Furthermore, irregular shapes of the *J-V* curve are observed in the inset for Φ_{bp}>0.50 eV. These irregular curves follow the behaviour of a back-to-back diode model. The analysis of the full circuit model presented in section 2.3 can be used to calculate the drop of voltage (V_{DS}) at the TCO/p-layer as a function of the Schottky barrier height, and it is observed that a value of Φ_{bp}>0.50 eV represents a considerable drop at the interface for practical solar cells. This is in close agreement with the results presented by Rubinelli in [5.10], where the forward bias curve of the illuminated solar cell is influenced by barriers higher than 0.6 eV approximately.

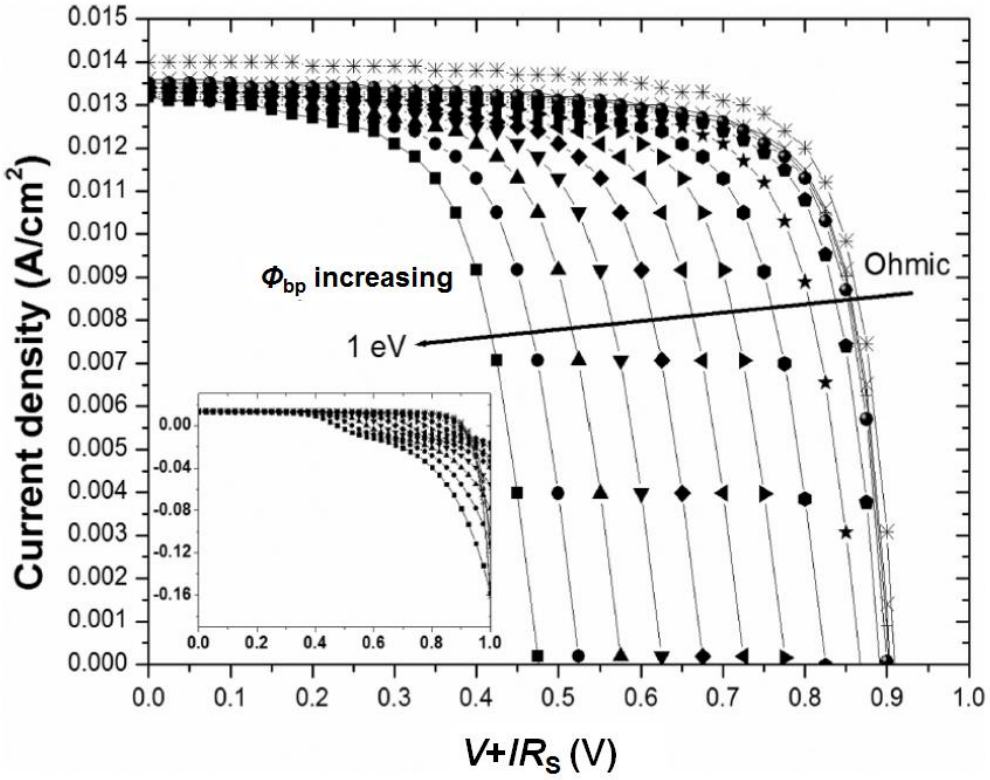

Figure 5.6. A detrimental effect on the V_{OC} is observed when the value of Φ_{bp} is increased higher than 0.50 eV when only thermionic emission is considered as a transport mechanism at the ZnO/a-Si:H(p) interface. Irregular *J-V* curves are obtained in the simulated voltage range for Φ_{bp}>0.50 eV.

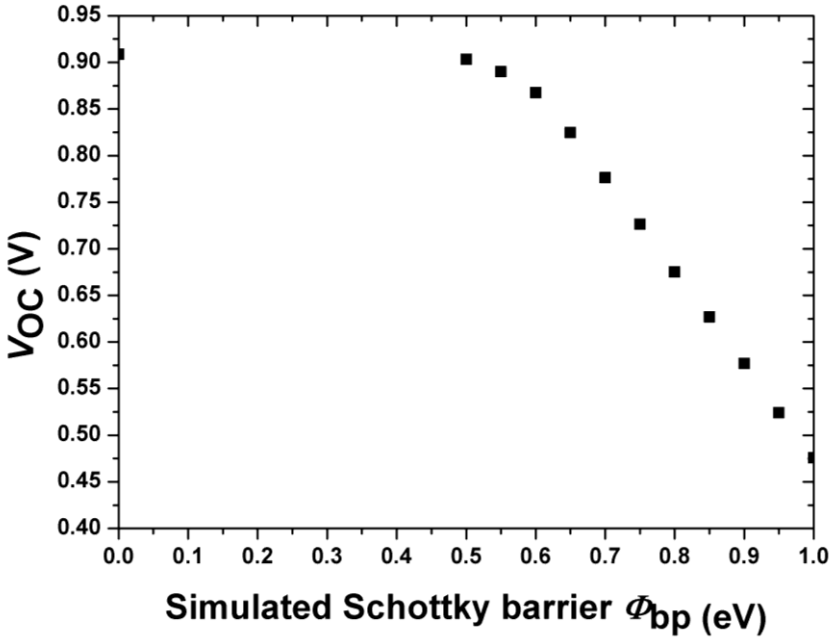

Figure 5.7. Simulated V_{OC} of the solar cell as a function of Φ_{bp}. A clear decrease of V_{OC} is observed when values of Φ_{bp}>0.50 eV are simulated.

However, even when a barrier in the range $0.7<\Phi_{bp}<0.9$ eV is expected for the real case, this kink has not been observed in experiment and the V_{OC} is not as low as in simulation either. It is found that the kink disappears only with the inclusion of tunnelling in the transport mechanism. Fig. 5.8 shows the impact of the UST model on the simulated *J-V* curves. Constant values of Φ_{bp}=0.75 eV and acceptor doping of $N_A= 4.5x10^{18}$ cm^{-3} (which is not as high as the optimistic value of $N_A=10^{19}$ cm^{-3} [5.9, 5.10]), were used to understand the effects of tunnelling transport. The value of Φ_{bp}=0.75 eV is taken from previous work [5.19], and it was evaluated by performing simulations and *J-V-T* measurements of ZnO/a-Si:H(p) diode structures. In the absence of such dedicated test structures, it is also possible to approximate a value of Φ_{bp} by applying the affinity rule when the electron affinity and bandgap of the semiconductor layer, and the work function of the metal contact are known. It is observed that even a high value of Φ_{bp}=0.75 eV matches the measured V_{OC} without destroying the shape of the *J-V* curve provided the universal Schottky tunnelling model is included.

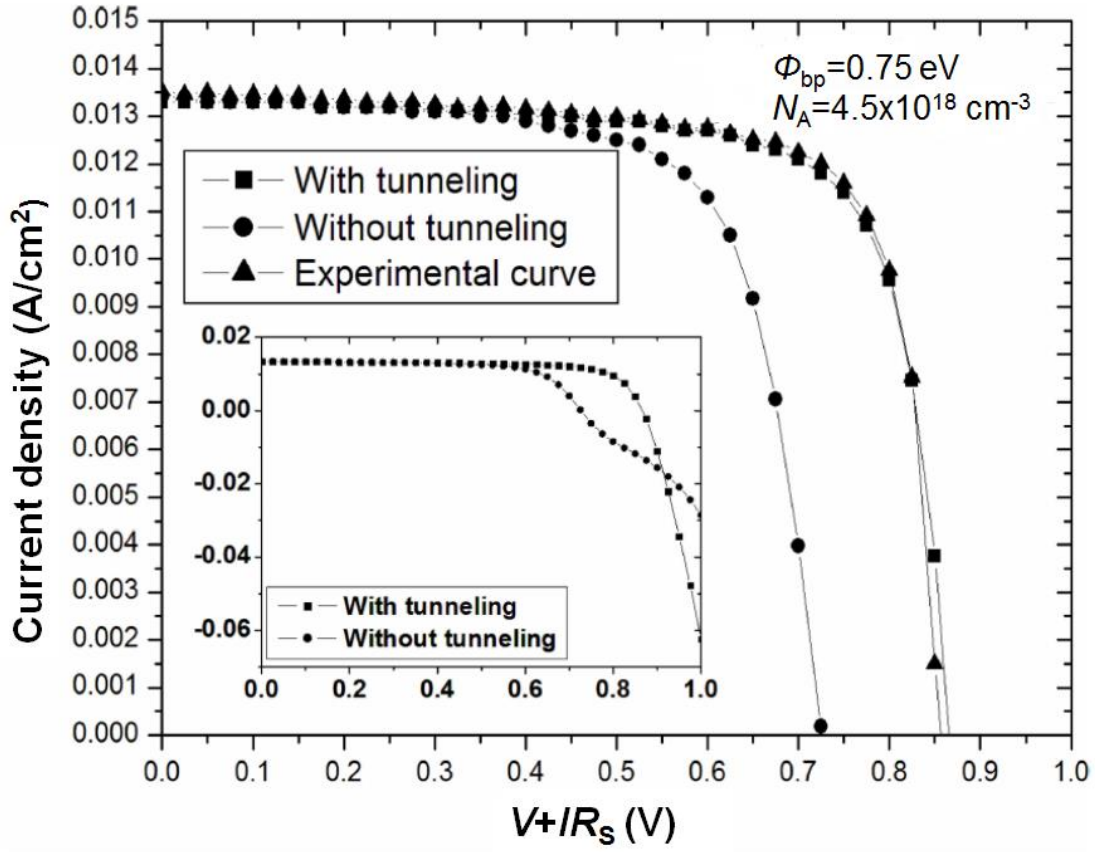

Figure 5.8. Impact of the tunnelling transport mechanism at the ZnO/a-Si:H(p) Schottky interface. The simulated *J-V* curve with Φ_{bp}=0.75 eV matches the experimental *J-V* curve only when tunnelling transport mechanism is considered. This also avoids the kink in the curve.

This result differs from [5.10], where inclusion of direct hole tunnelling has a minimal effect on the *J-V* curves. One possible explanation could be that other transport mechanisms such as multistep tunnelling or field-enhanced tunnelling have not been considered in their study. This would agree with the assumption made in [5.9], where it is mentioned that other types of tunnelling can have a significant effect on performance of the solar cell. An increased tunnelling transport would allow the existence of Schottky barriers heights greater than 0.50 eV without modifying the *J-V* curve, as is the case of our experimentally measured barrier of 0.75 eV.

The irregular behaviour of the *J-V* curve is not evident for the μc-Si:H(p) case, due to a low Φ_{bp}=0.45 eV. In Fig. 5.8 the measured *J-V* curves are compared with those predicted

by the circuit model in Eq. 2.5 for different values of the Schottky diode ideality factor *n*. Here, a variation of *n* represents a variation in the transport mechanism at the contact from pure thermionic emission (n=1) to high tunnelling ($n\geq2$). Once again, the value of the Schottky barrier height is kept constant at Φ_{bp}=0.75 eV. The ideality factor of the p-i-n diode is calculated from the slope of the linear region of the solar cell dark *J*-*V* characteristics presented in a semi-log scale as $n=(q/kT)dV/d\ln I$, with $I=JA$, whereas the saturation current is evaluated from the vertical axis intercept of the linear region extrapolated to V=0. Saturation current for the Schottky diode was calculated using Φ_{bp}=0.75 eV. It is observed that the V_{OC} of the solar cell decreases as *n* decreases. This demonstrates that increasing *n* in the Schottky junction indicates a transition of a contact from Schottky to Ohmic. A decrease of V_{OC} is also observed with an increase of Φ_{bp} as shown in Fig. 5.7. A combination of Φ_{bp} and *n* helps to model the interface and its effects on V_{OC}.

Finally, the effect of *n* as a function of Φ_{bp} on the drop of voltage V_{DS} at the interface is revealed in Fig. 5.9, where it can be seen that a high value of Φ_{bp} or a low value of *n* increases V_{DS}, which is calculated assuming a constant value of $I=I_{SC}$, since this represents the worst case possible. The drop of voltage at the Schottky interface of the purely a-Si:H cell is represented by the black dot for the evaluated values Φ_{bp}=0.75 eV and n=1.3, which corresponds to a significant drop of $V_{DS}\approx0.05$ V. It is also observed that the effects of tunnelling can be ignored provided that a low Φ_{bp} is achieved therefore, the study of *n* is irrelevant for interfaces such as ZnO/µc-Si:H(p), where $\Phi_{bp}\approx0.5$ eV, but becomes more important for other interfaces such as ZnO/a-Si:H(p), ZnO/a-SiC:H(p) or CdTe/Au.

5.4 Discussion

The explanations presented in this chapter are discussed in the context of previous work on electrical characterization and computer modelling of Schottky contacts for solar cells.

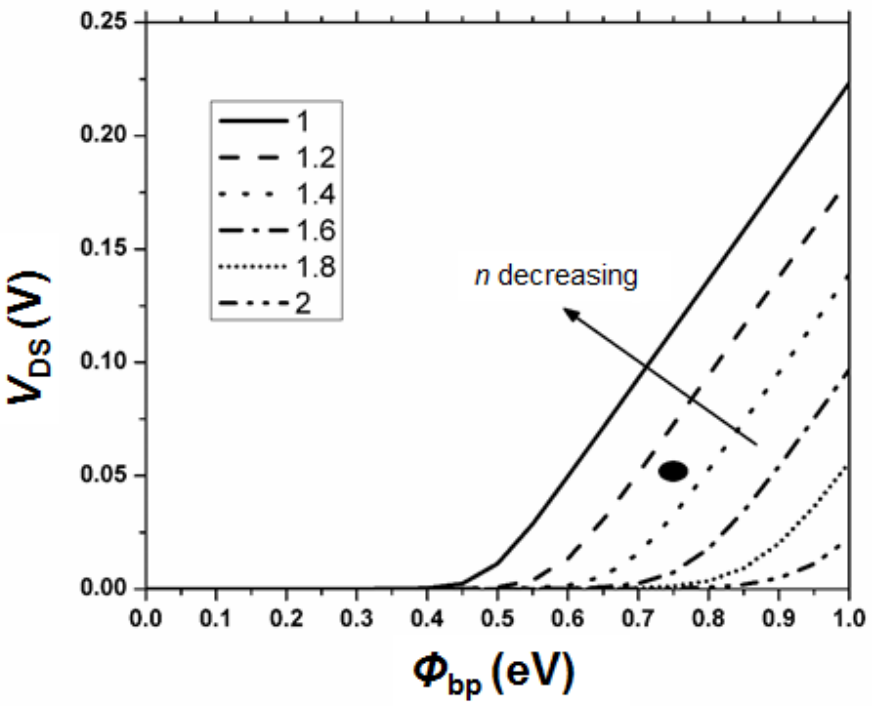

Figure 5.9. Drop of voltage at the Schottky interface as a function of Φ_{bp} and n for the sample with a-Si:H(p) layer. The black dot indicates the region of parameters evaluated for our cells, where $n \approx 1.3$.

Arch [5.9] examined the effects of a-Si:H(p) thickness and contact barrier height Φ_{bp} on the performance of a-Si:H solar cells. His computer simulations revealed that the barrier height of the front contact does not affect the performance of the solar cell when Φ_{bo}>1.2 eV, where he defined Φ_{bo} as the discontinuity between the work function of the contact and the conduction band edge of a-Si:H(p) layer. This critical value of Φ_{boe}=1.2 eV corresponds to Φ_{bp}=0.52 eV measured between the work function of the contact and the valence band edge of the a-Si:H(p) layer when a bandgap of E_g=1.72 eV is considered, which agrees with the results shown in this chapter. Since these threshold values are difficult to achieve experimentally, he implied the importance of considering the Schottky barrier height of the contact on the performance of the solar cell. Arch also concluded that tunnelling through the barrier at the contact/a-Si:H(p) interface should have significant impact on the performance of the solar cell. He also mentioned that tunnelling depends on the thickness of the barrier for holes, and on the defect density and doping concentration of the a-Si:H(p) layer. However, he did not provide quantitative evidence on the stated conclusion.

The work of Arch was continued by Rubinelli [5.9], who found that the reverse bias current and the forward bias current at low voltages are independent of the value of Φ_{bp} however, the illuminated and dark curves in the medium and high voltage regime do get affected. He mentioned that values of Φ_{bp}>0.6 eV affect the performance of the cell. This value is also in close agreement with the one found here.

The study of tunnelling at the contact of thin film silicon solar cells interface has often been ignored however, recently renewed interest on the physics of Schottky contacts for photovoltaic applications and their transport mechanism has developed due to the promising future of heterojunction solar cells. The low thickness of the a-Si:H(p) layer (≈5nm) in between 70 nm ITO(n^+) and 250 µm c-Si(n) produces a back-to-back diode structure, as reported by Kanevce [5.8]. She assumed thermionic emission in her simulations and PSPICE model of the solar cell and found a kink in the J-V curve, which is consistent with the results shown here. This kink disappeared only when tunnelling transport was included in the simulations. The results on the mixed µc-Si:H(p)/a-Si:H(p) layer discussed here could be applied to heterojunction cells to further improve their performance.

Bivour and Ritzau [5.22, 5.23] measured V_{OC} as a function of light intensity (Suns-V_{OC}) to study the influence of the Schottky barrier on the *FF* of the cell. They observed an increase of V_{OC} with an increase of illumination intensity, which reverses for illumination values of approximately 10 suns or higher. They attributed this behaviour to an increased photocurrent of the Schottky diode at high illumination. Although Suns-V_{OC} measurements are not presented in this thesis, their observation along with the results of Rubinelli [5.9] allow to explain the lack of rollover characteristics in the dark *J-V* curves of the cell, which is measured with the Schottky diode in reverse bias. This validates the methodology presented here for extraction of the solar cell parameters. Bivour and Ritzau also discussed that a proper adjustment of the work function of the TCO can result in values of *FF* higher than 80% for heterojunction solar cells.

The electronic circuit models developed by Niemegeers and Demtsu [5.7, 5.13] to explain the rollover characteristics of Au/CdTe/CdS/TCO solar cells are further improved

with the addition of tunnelling transport mechanism. This transport is more significant for thin-film silicon solar cells, since they include a-Si:H layers with thicknesses of few nanometres that increase the probability of thermionic-field emission at the Schottky interface. This explains why rollover characteristics are not observed for this type of solar cells. On the other hand, tunnelling transport is meaningless for CdTe solar cells, where the thickness of each layer is in the order of micrometres.

Finally, it is observed that the measured value of J_{SC} for solar cells with purely a-Si:H(p) is greater than for solar cells with µc-Si:H(p) layers. This observation is often discussed since there are reports indicating that the use of µc-Si:H(p) increases the absorption of light in the intrinsic region, as shown by Rath [5.21]. However, he also mentions that the crystallinity of µc-Si:H(p) increases as its thickness increases from 15 nm, which causes a decrease in its bandgap. As a consequence, this increases the band offset at the p/i interface which reduces the values of V_{OC} and J_{SC} in comparison to a more amorphous p-layer, as observed here.

5.5 Summary of Chapter 5

In chapter 5, the ZnO/a-Si:H(p) and ZnO/µc-Si:H(p) diode structures were used as window layers for solar cells in order to study the effects of the p-layer on the performance. The focus was on the development of a complete equivalent electronic circuit that considers the existence of a Schottky barrier height at the contacting interface. The inclusion of n improves the model developed in previous literature, which considered the existence of a Schottky barrier where the transport was completely dominated by thermionic emission over the barrier. The experimental measurements of the solar cells agree with the results of TCAD simulations. It was found that values of Φ_{bp}<0.5 eV can be considered as an Ohmic contact, which explains the difficulties to evaluate the Schottky barrier height for the ZnO/µc-Si:H(p) diode with the highest doping concentration in the previous chapter. This confirms once again that µc-Si:H(p) makes the better contact with ZnO. However, despite of the better contact properties of µc-Si:H(p), the cells using this layer showed the worst performance. It was identified in the simulated band diagrams that the reason of this detrimental effect on the

performance of the cell was the result of a discontinuity at the µc-Si:H(p)/a-Si:H(i) interface therefore, there is a compromise between producing a good contact with ZnO or a good interface with a-Si:H(i). These observations led to the testing of a mixed ZnO/µc-Si:H(p)/a-Si:H(p) window layer that benefit from the best properties of each material and further improve the performance of the cell.

5.6 References in Chapter 5

[5.1] M. Kubon, E. Boehmer, M. Gastel, F. Siebke, W. Beyer, C. Beneking, and H. Wagner, "Solution of the ZnO/p contact problem in a-Si:H solar cells," in *Photovoltaic Energy Conversion Conference Record of the Twenty Fourth IEEE PVSC*, 1994.

[5.2] M. Kubon, E. Boehmer, F. Siebke, B. Rech, C. Beneking, and H. Wagner, "Solution of the ZnO/p contact problem in a-Si:H solar cells," *Solar Energy Materials and Solar Cells*, vol. 41-42, pp. 485-492, 1996.

[5.3] P.-K. Chang, P.-T. Hsieh, C.-H. Lu, C.-H. Yeh, and M.-P. Houng, "Development of high efficiency p–i–n amorphous silicon solar cells with the p-μc-Si:H/p-a-SiC:H double window layer," *Solar Energy Materials and Solar Cells*, vol. 95, no. 9, pp. 2659, 2011.

[5.4] G. Ganguly et al., "Improved fill factors in amorphous silicon solar cells on zinc oxide by insertion of a germanium layer to block impurity incorporation," *Applied Physics Letters*, vol. 85, no. 3, p. 479, 2004.

[5.5] J.-San Im, J.-wan Jeon, S. Park, Y. Lee, and K. S. Lim, "Improvement of amorphous silicon solar cell performance by inserting a tungsten oxide layer between zinc oxide and p-type amorphous silicon carbide," in 37th IEEE *PVSC*, Seattle, USA, 2011 pp. 612-615.

[5.6] J. Kim, A. Abou-Kandil, K. Fogel, H. Hovel, and D. K. Sadana, "The role of high work-function metallic nanodots on the performance of a-Si:H solar cells: offering Ohmic contact to light trapping," *ACS nano*, vol. 4, no. 12, pp. 7331, 2010.

[5.7] A. Niemegeers and M. Burgelman, "Effects of the Au/CdTe back contact on IV and CV characteristics of Au/CdTe/CdS/TCO solar cells," *Journal of Applied Physics*, vol. 81, no. 6, pp. 2881, 1997.

[5.8] A. Kanevce and W. K. Metzger, "The role of amorphous silicon and tunneling in heterojunction with intrinsic thin layer (HIT) solar cells," *Journal of Applied Physics*, vol. 105, no. 9, pp. 094507, 2009.

[5.9] J. K. Arch, F. A. Rubinelli, J.-Y. Hou, and S. J. Fonash, "Computer analysis of the role of p-layer quality, thickness, transport mechanisms, and contact barrier height in the performance of hydrogenated amorphous silicon p-i-n solar cells," *Journal of Applied Physics*, vol. 69, no. 10, p. 7057, 1991.

[5.10] F. A. Rubinelli, J. K. Arch, and S. J. Fonash, "Effect of contact barrier heights on a-Si:H p-i-n detector and solar-cell performance," *Journal of Applied Physics*, vol. 72, no. 4, p. 1621, 1992.

[5.11] A. N. Corpus-Mendoza, M. M. De Souza, and F. U. Hamelmann, "Design of Schottky Contacts for Optimum Performance of Thin-Film Silicon Solar Cells," *IEEE Journal of Photovoltaics*, vol. 5, no. 1, pp. 22–27, 2015.

[5.12] G. Stollwerck and J. R. Sites, "Analysis of CdTe back-contact barriers," in *Proc. Of 13th European PVSEC*, Nice, France, 1995, pp. *107*.

[5.13] S. H. Demtsu and J. R. Sites, "Effect of back-contact barrier on thin-film CdTe solar cells," *Thin Solid Films*, vol. 510, no. 1-2, pp. 320, 2006.

[5.14] K. Matsuzawa, K. Uchida and A. Nishiyama, "A Unified Simulation of Schottky and Ohmic Contacts," *IEEE Transactions on Electron Devices*, vol. 47, no. 1, pp. 103, 2000.

[5.15] M. Ieong, P. M. Solomon and S. E. Laux "Comparison of raised and Schottky source/drain MOSFETs using a novel tunneling contact model," published in the technical digest of the IEDM meeting 1998, vol. 98, pp. 733.

[5.16] S. Selberherr, "Analysis and simulation of semiconductor devices," Springer-Verlag. Wien, New York, 1984.

[5.17] W. Shockley and W. T. Read, "Statistics of the Recombinations of Holes and Electrons," *Phys. Rev*, vol. 87, no. 5, pp. 835, 1952.

[5.18] R. N. Hall, "Electron-Hole Recombination in Germanium," *Phys. Rev.*, vol. 387, pp. 387, 1952

[5.19] A. N. Corpus-Mendoza, M. M. De Souza, and F. Hamelmann, "Transport mechanisms and effective Schottky barrier height of ZnO/a-Si:H and ZnO/μc-Si:H heterojunction solar cells," *Journal of Applied Physics*, vol. 114, pp. 184505, 2013.

[5.20] W. E Spear, and P. G. Le Comber, "Substitutional doping of amorphous silicon," *Solid State Communications*, vol. 17, issue 9, pp. 1193–1196, 1975.

[5.21] J. Rath, "Incorporation of p-type microcrystalline silicon films in amorphous silicon based solar cells in a superstrate structure," *Solar Energy Materials and Solar Cells*, vol. 53, no. 1-2, pp. 189, 1998

[5.22] M. Bivour, C. Reichel, M. Hermle, and S. W. Glunz, "Improving the a-Si:H(p) rear emitter contact of n-type silicon solar cells," *Solar Energy Materials and Solar Cells*, vol. 106, pp. 11–16, 2012.

[5.23] K. U. Ritzau, M. Bivour, S. Schröer, H. Steinkemper, P. Reinecke, F. Wagner and M. Hermle, "TCO work function related transport losses at the a-Si:H/TCO-contact in SHJ solar cells," *Solar Energy Materials and Solar Cells*, vol. 131, pp. 9–13, 2014.

Chapter 6.
The impact of the p-layer on the stability of thin film silicon solar cells

The use of current injection and light exposure is shown to distinguish the impact of degradation of the contact, and intrinsic regions of a-Si:H thin film solar cells respectively. The drop in the maximum power conversion capability of the cell after light exposure is a consequence of an increase of dangling bonds in the intrinsic layer of the cell due to the Staebler-Wronksi effect, which reduces all the parameters of the cell. On the other hand, injected current increases the open circuit voltage but greatly reduces the fill factor with no evident impact on short circuit current, which is attributed to a reduction of tunnelling transport at the Schottky interface. An explanation for this is found via TCAD simulations. A clear distinction of degradation mechanisms is observed from evolution of the ideality factor m of the main junction, and the ideality factor n of the ZnO/a-Si:H(p) interface.

The effects of a-Si:H(p) and µc-Si:H(p) window layers on the solar cell as a function of time exposure to light and current injection are presented in this chapter. Here, the conventional solar cell parameters (V_{OC}, J_{SC}, P_{MAX}, and FF) are used to evaluate the performance of the different samples with time, whereas the equivalent full circuit parameters (m, I_O, n and Φ) extracted in previous chapters are evaluated in order to identify the location of degradation within the cell.

Currently, the decrease of photoconductivity with intense light soaking (Staebler-Wronski effect), as found by Staebler and Wronski [6.1], represents the greatest obstacle for economic solar energy conversion in thin film silicon solar cells. This light induced degradation has been attributed to an increase of dangling bonds which dominates the density of states of amorphous silicon. However, light exposure is not the only way to introduce defects in a solar cell, it can also be done by carrier injection, as found by Street in a-Si:H p-i-n devices [6.2]. Since both methods produce an excess of electron-hole pairs, it has been suggested that a recombination of carriers near weak dangling bonds are responsible for the increase of defects [6.3]. Previous research has taken advantage of this similitude between light induced degradation (LID) and current induced degradation (CID) to implement an accelerated degradation process for a-Si:H solar cells which combines both degradation mechanisms [6.4]. However, it is well known that LID of a-Si:H solar cells occurs mainly due to an increase of defects in the intrinsic region of the structure, while some studies of CID degradation show the increase of defects mainly near the p/i interface [6.5] or defects migrating from the p/i interface to the intrinsic layer after prolonged current injection [6.6].

It is shown in this chapter that CID differs from LID, as the former has the effect of reducing the solar cell FF without having an effect on J_{SC} when a-Si:H(p) is used as the window layer in contact with ZnO, whereas a decrease of FF is always accompanied by a reduction of J_{SC} during the LID experiment as a consequence of an increase of defects in the intrinsic region. Since the reduction of FF during CID is only observed for cells with a-Si:H(p) window layer and not for cells with a µc-Si:H(p) layer, this degradation is attributed to a decrease of tunnelling transport at the ZnO/a-Si:H interface, as will be shown by the change of the extracted parasitic Schottky diode parameters.

6.1 Methodology for the study of stability of thin film silicon solar cells

The fabrication details for the solar cells have been described in Chapter 2. Here, the LID experiment consisted in exposing the solar cell to 1 Sun AM 1.5 illumination for a period of up to 100 hours, while the *J-V* curves were measured at different time intervals. A CID experiment was also performed on the cells by applying a constant current stress of 10 mA/cm^2 for the same period of time. A comparison of these two degradation techniques for thin film silicon solar cells with a-Si:H(p), µc-Si:H(p) and µc-Si:H(p)/a-Si:H(p) layers is presented next. Here, at least four different cells of each type were measured for each degradation technique.

6.2 Degradation of thin film silicon solar cells

Fig. 6.1 shows a change in the solar cell parameters as a function of time when exposed to 1 Sun AM1.5 illumination (LID) or when injected with a constant current density of 10 mA/cm^2 (CID). The absolute values used as the 100% reference in Fig. 6.1 are 0.83 V, 13.4 mA/cm^2, 7.7 mW, and 68.87% for V_{OC}, J_{SC}, P_{MAX}, and *FF*, respectively, for the cells with a-Si:H(p) layer, whereas the values for the cells with µc-Si:H(p) layers are 0.81 V, 12.4 mA/cm^2, 7 mW, and 69.6%. The data presented are averages of the different cells measured. The motivation is to understand the impact of a-Si:H(p) layer and the µc-Si:H(p) layers on the solar cell therefore, the cell with a mixed µc-Si:H(p)/a-Si:H(p) window layer will be analysed in a further section. It is observed that the LID curves can be very well fitted by an exponential decay that results from the Staebler-Wronski effect, which reduces the performance of the solar cell mainly because of an increase of defects in the intrinsic layer. On the other hand, the cells degraded with current show very different behaviour for each of the parameters which are heavily affected by the choice of p-layer.

Probably the most informative parameter shown in Fig. 6.1 is J_{SC}, since it is observed that it is mainly reduced when the cell is exposed to light, but not when current flows through it. This behaviour suggests that the current injected does not create defects in the intrinsic

layer. Also, the reduction of J_{SC} is less when µc-Si:H(p) is used as a window layer instead of a-Si:H(p), which is attributed to the narrower bandgap and increased crystallinity of µc-Si:H(p) preventing some of the light from reaching the intrinsic region, as explained in the previous chapter. In a similar way, a lesser degradation of *FF* and P_{MAX} results as a consequence of a reduced quantity of defects in the intrinsic layer when µc-Si:H(p) is used in the LID experiment. However, the most noticeable change in all of the parameters is the drastic reduction of *FF* shown by the cell with a-Si:H(p) layer during the CID experiment. This reduction of *FF* however, is not accompanied by a reduction of J_{SC} or V_{OC}, therefore the value of P_{MAX} does not degrade as much as in the LID experiments.

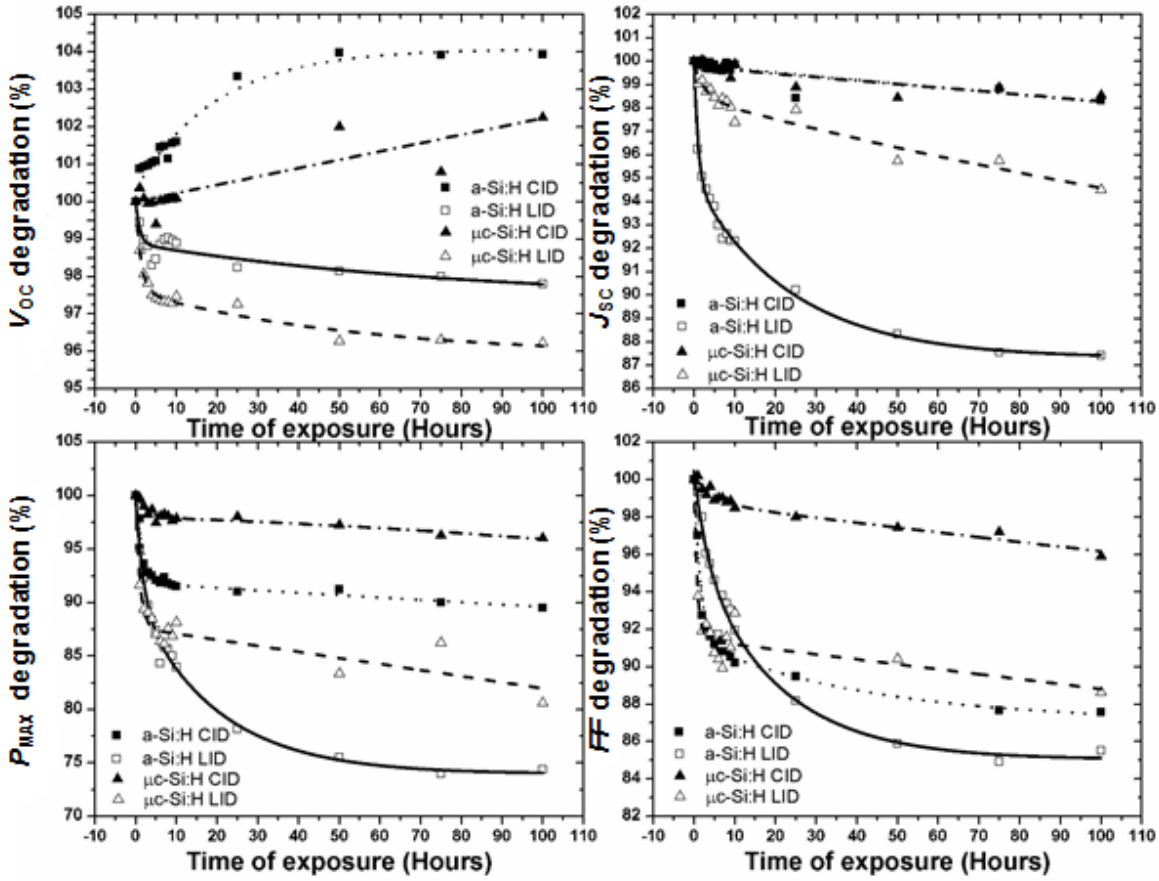

Figure 6.1. LID and CID studies for thin film cells with a-Si:H(p) and µc-Si:H(p) window layers.

The case of an a-Si:H cell is analysed with the equivalent electronic circuit developed in Chapter 5 in order to identify the element suffering the degradation. The parameters are calculated as explained in Chapter 2 and Chapter 5, and the ideality factor *n* of the Schottky

interface is fitted at the end to match the experimental *J-V* curve. There is no need to calculate *n* for the cells using µc-Si:H(p) material, since it produces a Schottky barrier height lower than the critical Φ_{bp}=0.5 eV. Similarly, in [6.7] it was described via computer simulations that an increase of defects from 10^{19} cm^{-3} to 10^{20} cm^{-3} in an a-SiC:H(p) layer can have an increasing effect on the V_{OC} of the cell, whereas the latest degradation study by Wronski shows that an increase of defects in the intrinsic layer observed during LID decreases the V_{OC} [6.8]. This increase of V_{OC} is also evident in our cells however, we identify its origin experimentally by the use of accelerated damage via current injection in this work.

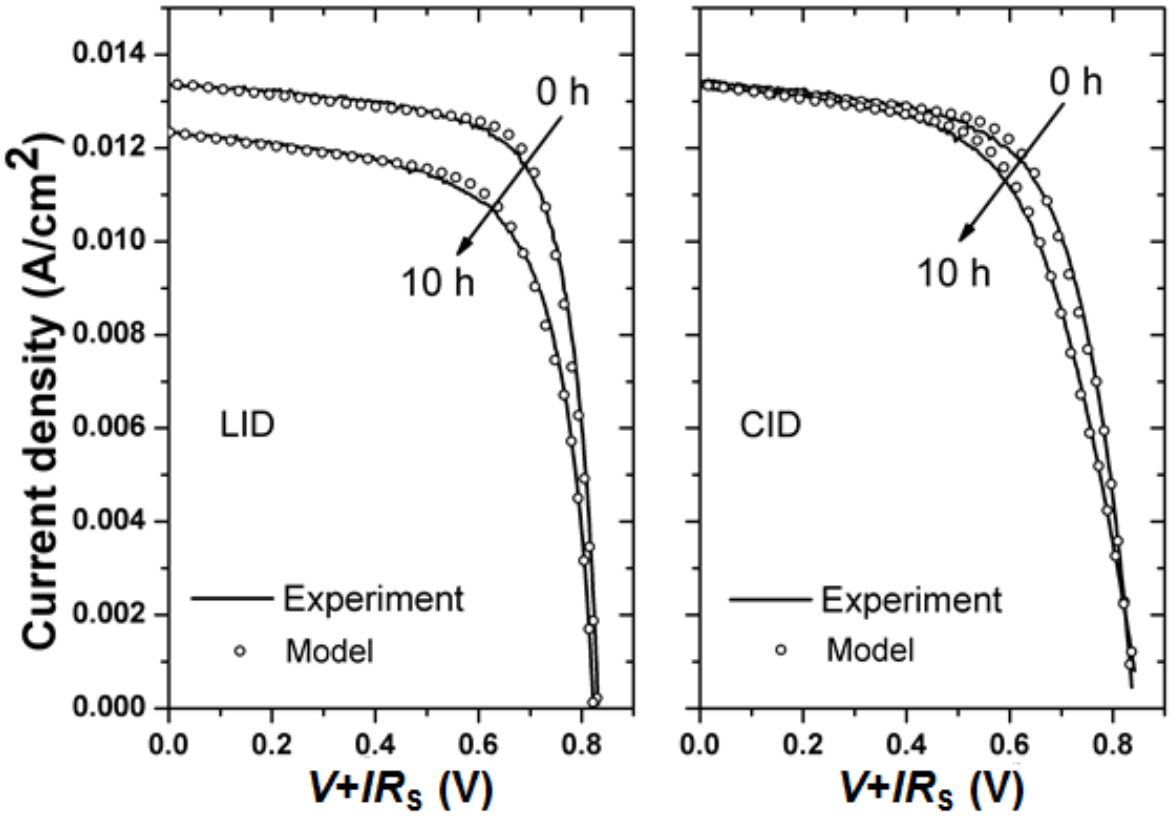

Figure 6.2. Degradation of the *J-V* curve for a-Si:H solar cells under light exposure and current injection.

The degradation of the a-Si:H cell is analyzed next. This requires the use of the complete equivalent electronic circuit described in section 2.3. This evaluation is not shown for the cells with µc-Si:H(p) which do not show a noticeable degradation after current

injection. A possible reason for this behaviour is the greater stability of μc-Si:H(p) and its Ohmic contact with ZnO (Φ_{bp} <0.5 eV), as described in our previous studies [6.9, 6.10]. Fig. 6.2 shows the effects of LID and CID on the *J-V* curves of the cell during the initial 10 hours of degradation. It is clearly observed that the degradation of P_{MAX} during LID results from a combination of *FF* and J_{SC} reduction, whereas the P_{MAX} degradation during CID results from *FF* reduction only. The elements of the equivalent circuit found to cause these changes are plotted in Fig. 6.3. It is observed that *m* increases and *n* decreases when current is injected, whereas *m* increases even more and *n* remains constant with light exposure. This proves that the density of defects in the intrinsic layer are mainly increased during the LID experiment (*m* increases, i-layer recombination increases) without really having a great impact at the Schottky interface (*n* remains constant). On the other hand, the CID experiment causes a small increase of *m*, accompanied by a decrease of *n*. This decrease of *n* means a reduced tunneling transport mechanism at the ZnO/a-Si:H Schottky interface which can be caused by creation of defects near the interface. Expected values of *m* and *n* for a solar cell should be opposite, with *m* as low as possible to avoid recombination in the bulk, and with *n* as high as possible to prevent the creation of a Schottky contact.

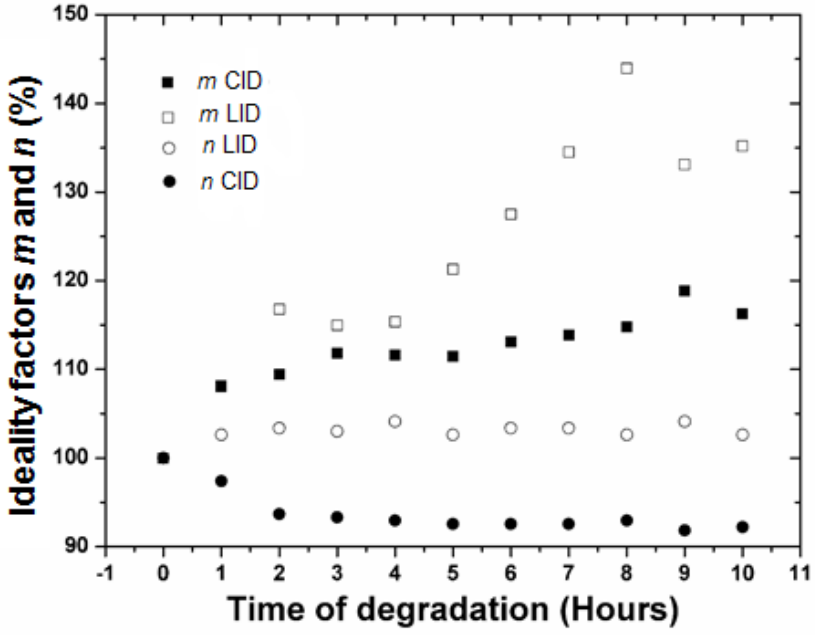

Figure 6.3. Changes on the ideality factors *m* and *n* for a-Si:H solar cells under light exposure and current injection.

The different behaviour of *m* and *n* can also be observed in Fig. 6.4, where both ideality factors are plotted against the change in J_{SC} observed during 100 hours of stress. It is observed that there is a linear dependence of *m*, and no change of *n* as a function of degradation of J_{SC} during LID. In contrast, there is a rapid change of both ideality factors vs degradation of J_{SC} that appears during the first hours of CID and reaches saturation, indicating clearly the differences in the mechanisms. Similarly, Fig. 6.5 compares the external quantum efficiency (EQE) curves for the initial and degraded states after light exposure and current injection. It is observed that a reduction of the EQE curve occurs only with LID, which indicates a reduced generation of electron-hole pairs at the intrinsic region, whereas the EQE curve during CID remains practically constant.

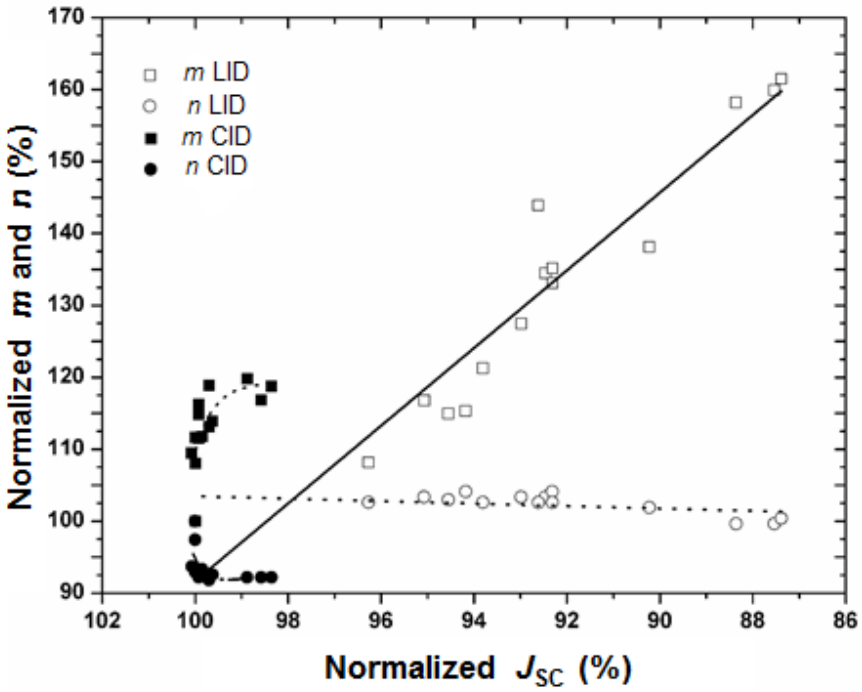

Figure 6.4. Different modes of degradation observed for *m* and *n* as a function of J_{SC} during LID and CID.

Finally, Fig. 6.6 shows the effects of both degradation techniques on the series resistance, R_S evaluated from the dark *I-V* curve. It is observed that a change of R_S occurs during CID for the first 6-10 hours saturating after this time interval. A change of R_S is not

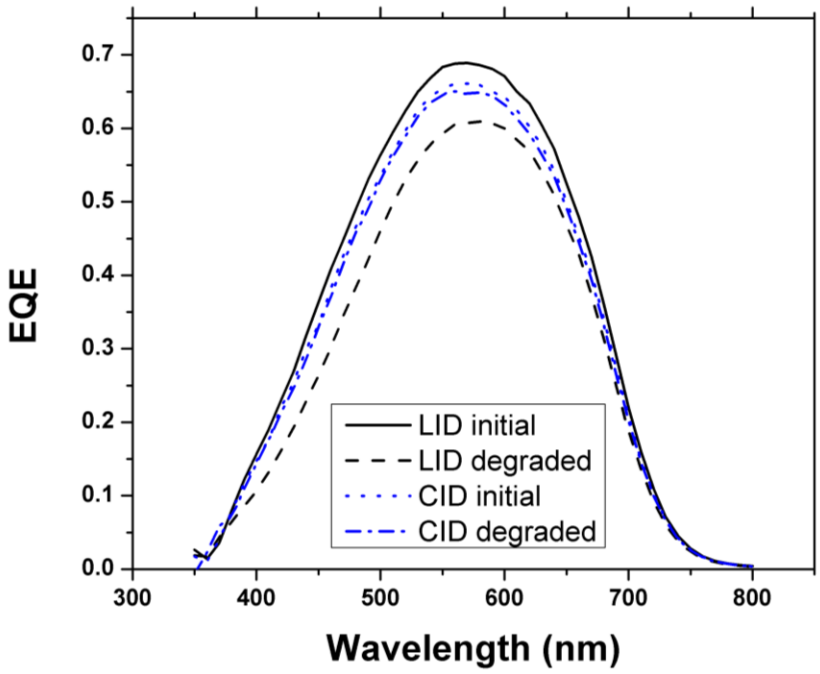

Figure 6.5. EQE at 0V for the fully a-Si:H solar cell. Degradation of the curve is observed after light exposure, whereas no changes are observed after current injection.

observed during LID. This behaviour of R_S, along with the degradation of J_{SC} further confirms the behavior of *m* and *n* during LID and CID respectively. A continuous increase of *m* with no change of *n* during LID in comparison to a reduction of *n* during CID, points to an increase of defects in the intrinsic layer after light exposure, and degradation near the contacts after current injection. These explanations are consistent with the lack of CID shown by the cells with µc-Si:H(p) window layers.

Once the cells with a-Si:H(p) and µc-Si:H(p) layers have been analysed separately, it is possible to continue the analysis of stability for the µc-Si:H(p)/a-Si:H(p) mixed layer cell. Fig. 6.7 shows the LID and CID measurements for this cell. It is observed once again that J_{SC} is mainly degraded under light exposure, whereas the degradation of J_{SC} during current injection is less. This inferior degradation of J_{SC} during the CID experiment helps the solar cell to maintain a higher value of P_{MAX} in comparison to the LID experiment, as it is observed in solar cells with a-Si:H(p) and µc-Si:H(p) layers. Still, the value of *FF* degrades more than

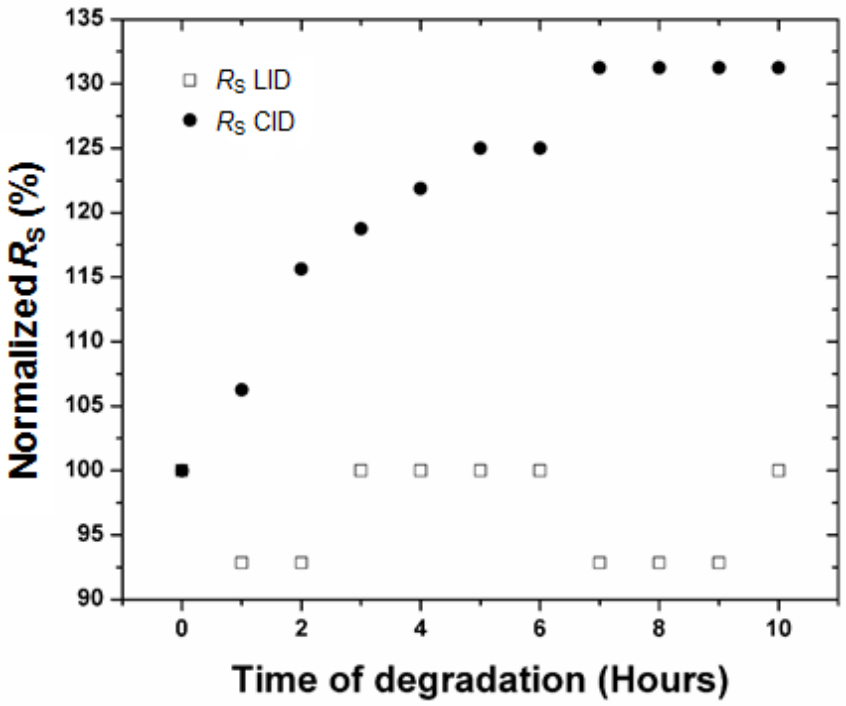

Figure 6.6. The value of R_S=3.8 Ω extracted from the dark *I-V* curve is observed to degrade during CID only, whereas no change on R_S is observed during LID.

in the cell with µc-Si:H(p) layer but less than in the cell with a-Si:H(p) layer. This observation also agrees with the previous assumption that LID has its most important effect on the a-Si:H(i) layer of the cell, whereas CID affects the p-layer and its interfaces, especially the tunnelling mechanism, as it was demonstrated using the full equivalent circuit of the solar cell.

However, a consistent observation during CID experiments is an increase of V_{OC} for the cells with a-Si:H(p) layer, which was not observed for the mixed layer cells, as shown in Fig. 6.7. Here, TCAD simulations were used once again in order to explain this behaviour considering that current injection causes a change in the p-layer that is not fully reversible once the stress is removed. This is demonstrated in Table 3, which shows a comparison of the degraded and annealed values of the solar cell parameters as a proportion of the initial value. The annealed values are averages obtained after annealing the degraded cells at 115 ºC for 48 hours. It is observed that J_{SC} remains low after annealing, which confirms that the damage is not related to LID. Also, the annealed a-Si:H solar cells show a minimal decrease

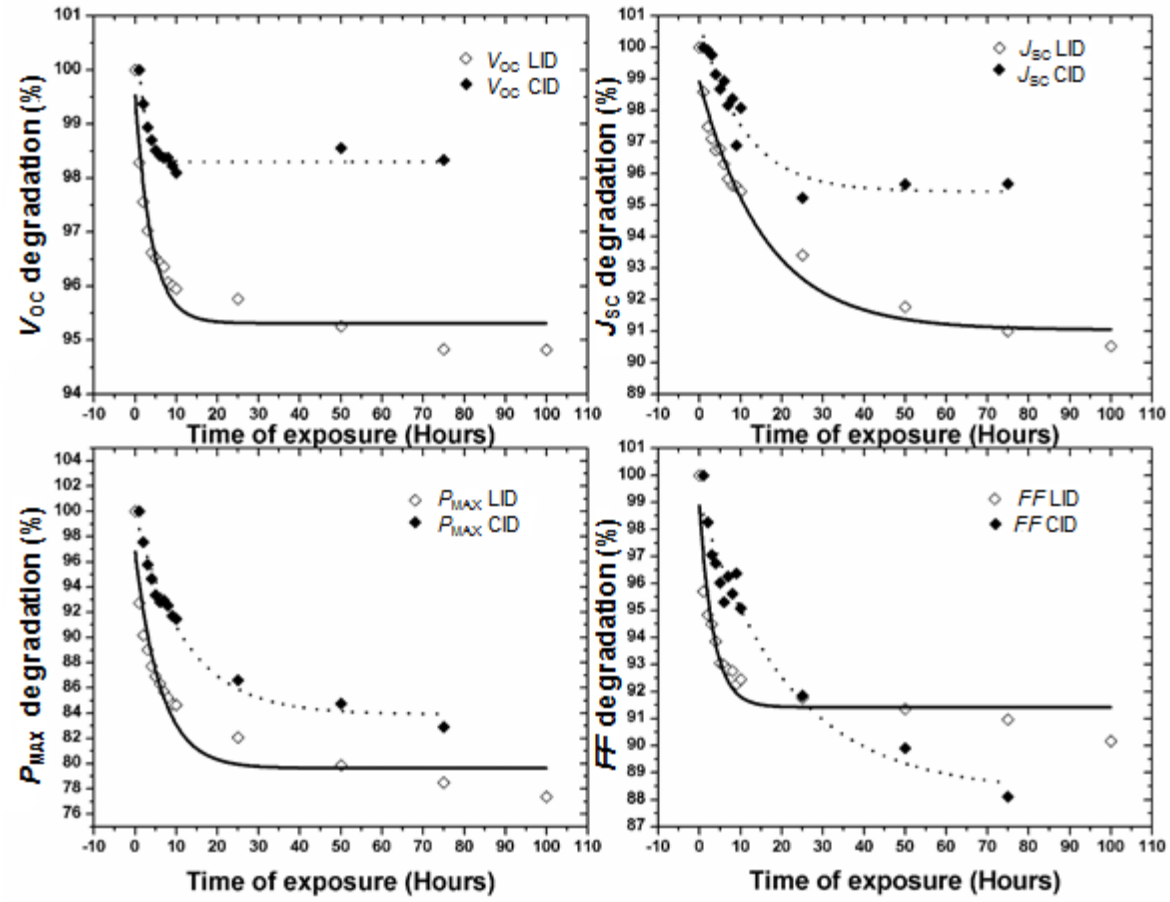

Figure 6.7. LID and CID studies for thin film cells with mixed µc-Si:H(p)/a-Si:H(p) window layers.

of V_{OC} which is not evident for the cells with µc-Si:H(p) layers. This relates CID to an effect of the p-layer rather than the intrinsic region.

Table 3. Performance values of solar cells at the initial, degraded, and annealed stages. Solar cells were degraded with current and annealed at 115 ºC during 48 hours.

Parameter	Initial value. All cells (%)	Degraded a-Si:H cell (%)	Annealed a-Si:H cell (%)	Degraded µ-Si:H cell (%)	Annealed a-Si:H cell (%)
V_{OC}	100.0	103.9	103.6	102.3	103.3
J_{SC}	100.0	98.3	98.4	98.5	96.0
P_{MAX}	100.0	89.8	92.5	96.0	96
FF	100.0	87.6	90.4	95.9	97.2

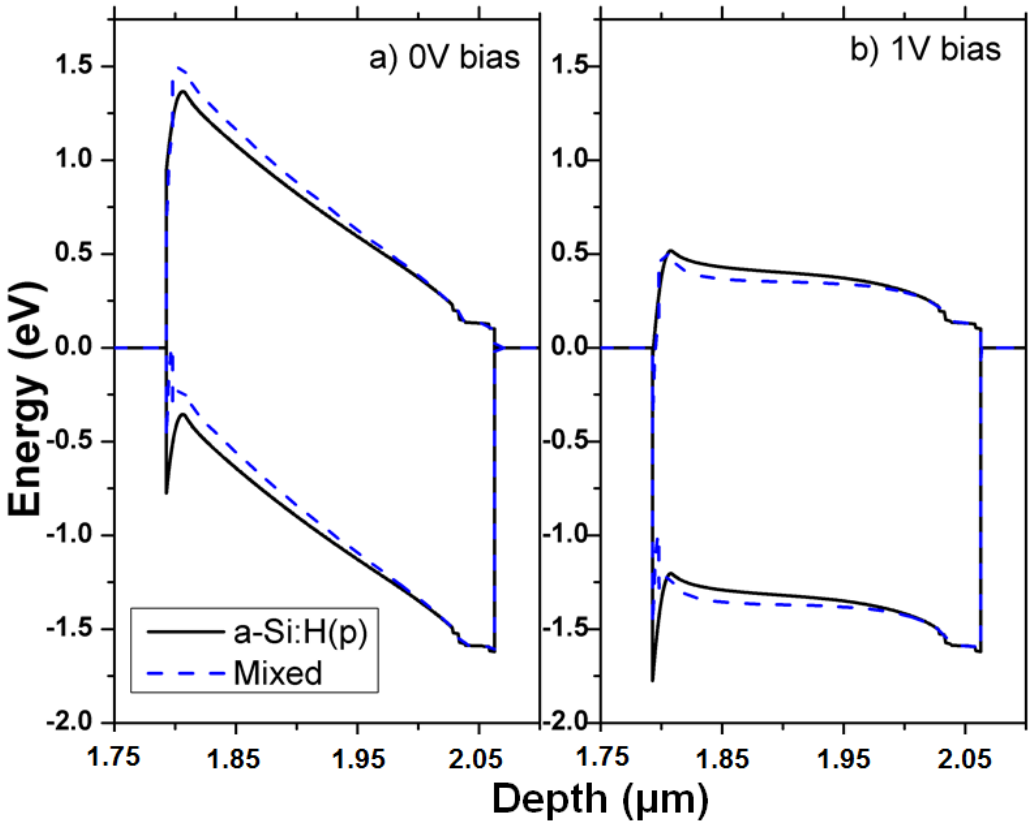

Figure 6.8. Simulated energy band diagrams for the cells with a-Si:H(p) and μc-Si:H(p)/a-Si:H(p) mixed layers at 0 and 1V (approximate current stress condition).

Fig. 6.8 and 6.9 show the energy band diagrams and hole concentrations at 0V and 1V of the a-Si:H and mixed cells respectively. A value of 1V is used in the simulation since it was the approximate voltage applied to keep a constant current density of 10 mA/cm^2 flowing through the measured cells. It can be seen in Fig. 6.8 that the p-layer valence band shifts to lower levels under current injection. This happens because the Schottky junction is in reverse bias during CID. At the same time, the conduction band gets closer to the contact work function, which allows an easier path for electrons to flow across the cell. This excess of electrons causes a reduction in the hole concentration near the ZnO contact in the cell. A reduction in the hole concentration is not evident for the cell with mixed layer, due to its lower Schottky barrier with ZnO.

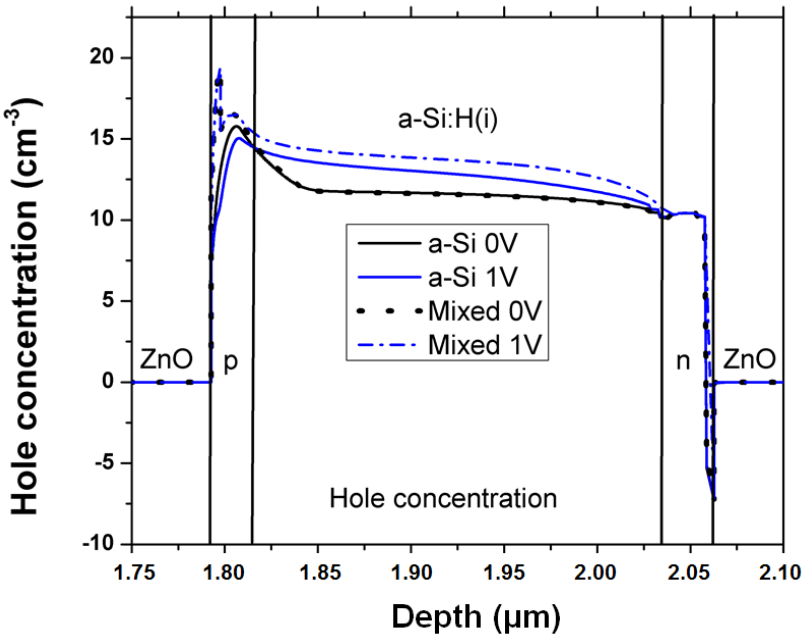

Figure 6.9. Simulated hole concentration for cells with a-Si:H(p) layer and µc-Si:H(p)/a-Si:H(p) mixed layers for 0V and 1V.

This phenomenon is explained if the reduction in hole concentration does not completely return to normal levels once the current stress is removed. This is probably caused by a deactivation of boron dopants caused by the excess of electrons injected therefore, this process of deactivation has been artificially simulated via TCAD by changing the boron doping profile on the a-Si:H(p) layer. This should not be the case for the cell with mixed layer due to the superior stability of doping in µc-Si:H(p) used in contact with ZnO.

The boron doping profile of the initial and degraded states of the a-Si:H(p) layer is shown in Fig. 6.10. Here, a Gaussian doping profile was chosen to represent a practical solar cell, where a high concentration of dopants is introduced near the contact to increase tunnelling transport across the interface and a lower concentration is used near the i-layer to avoid boron contamination of the intrinsic region. It is expected that a reduction of the doping concentration near the ZnO contact should reduce the tunnelling transport across the Schottky interface, as expressed by Eq. 5.1. As a consequence, this would cause a reduction of the *FF* of the cell. On the other hand, only the increase of doping near the i-layer can explain the observed increase of V_{OC}.

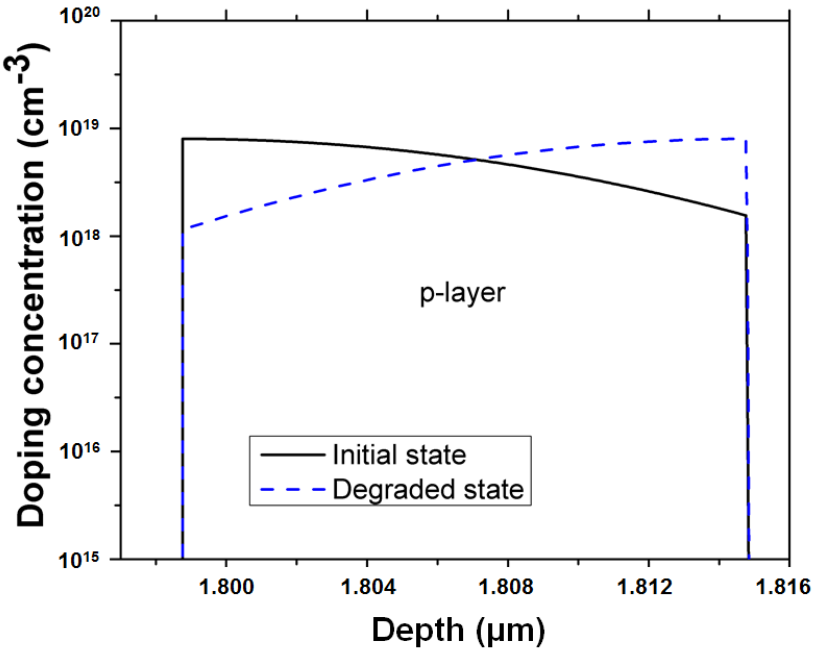

Figure 6.10. Simulated boron doping profile for the initial and degraded states of the fully a-Si:H cell.

Fig. 6.11 shows the effects on the *J-V* curve introduced by a change in the doping profile for different values of Schottky barrier simulated by modifying the contact work function from an Ohmic case (Φ_{bp}<0.5 eV) to bad quality contact with a high Schottky barrier ($\Phi_{bp} \approx 0.85$ eV). A realistic work function can be expected to be $\Phi_{bp} \approx 0.75$ eV, as shown in previous chapters. It can be observed in Fig. 6.11 that a simultaneous decrease and increase of dopants near the contact and intrinsic layer respectively can cause both of the effects observed experimentally which are, a reduction of *FF* and an increase of V_{OC}. However, the change in the *J-V* curve depends on the value of Schottky barrier height simulated. It is clearly observed that the decrease of *FF* is only present when a non-ideal contact is considered, otherwise no change in the *J-V* curve can be seen when the contact is considered to be Ohmic. It can also be observed that the maximum increase of V_{OC} occurs for a Schottky barrier $\Phi_{bp} \approx 0.75$ eV, whereas the detrimental effect on the knee of the curve (cause of an increase of R_S) for greater values of Φ_{bp} overcomes the change of the *J-V* curve and causes a reduction of V_{OC} for the worse quality contacts.

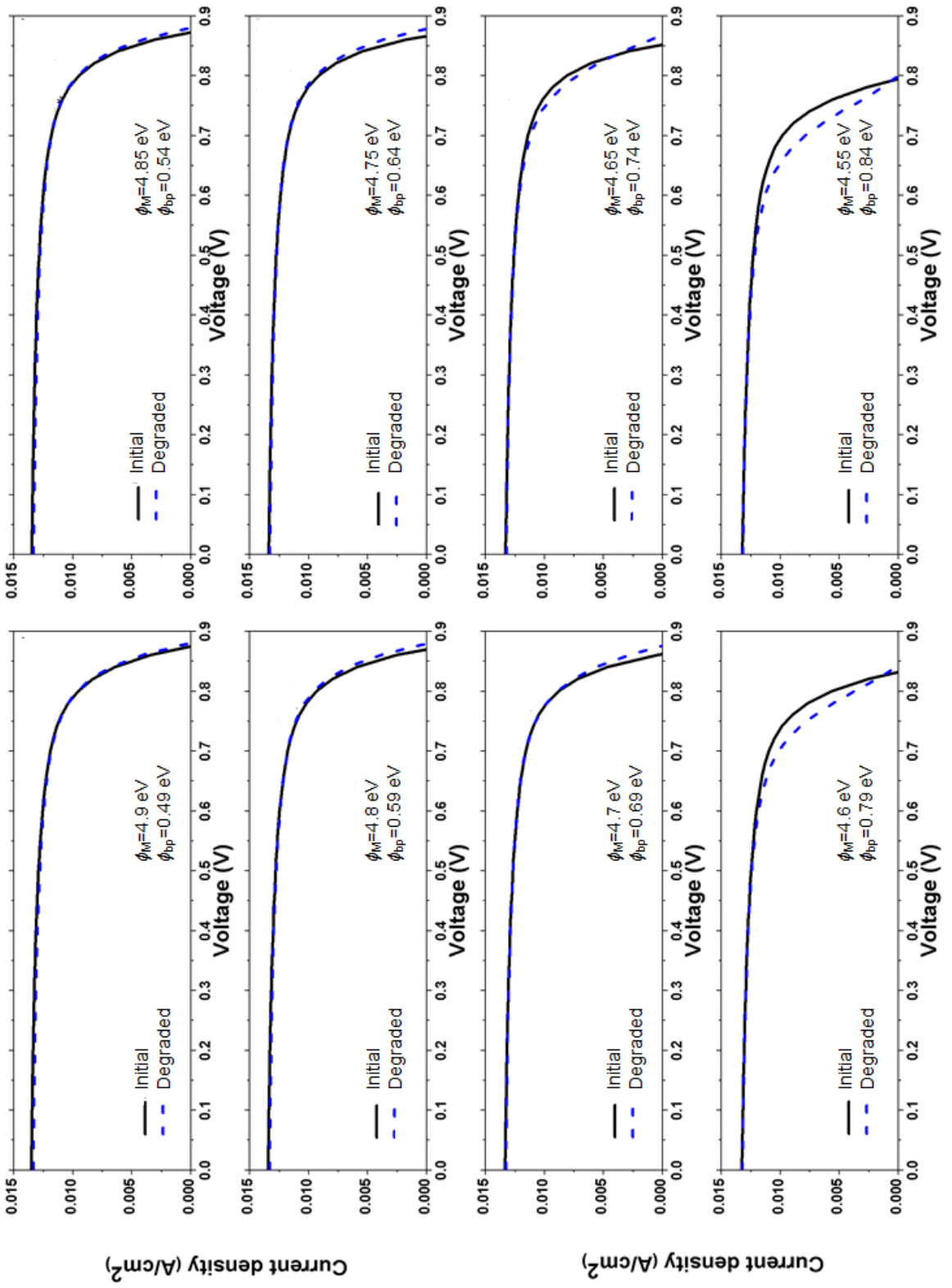

Figure 6.11. Effect of changing the doping profile on the p-layer of the fully a-Si:H cell for different values of Schottky barrier.

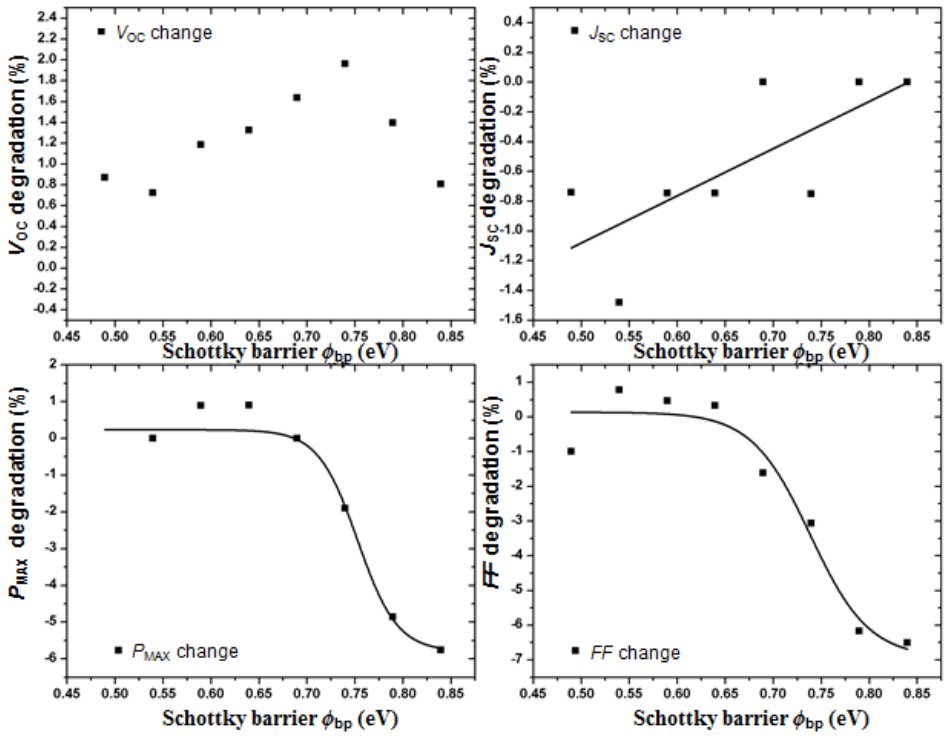

Figure 6.12. Solar cell parameters for the simulated initial and degraded states after current injection showing the influence of the Schottky barrier height at the contact interface.

Finally, the degradation of the solar cell parameters obtained from simulations are plotted in Fig. 6.12 for the cell with a-Si:H(p) layer, where as seen in experiments, the degradation of P_{MAX} is a consequence of a reduction of FF mainly, since J_{SC} remains without any noticeable change. The minimal change of J_{SC} observed for the different values of Φ_{bp} is attributed to the sampling of the model, more than to an actual effect of Φ_{bp}. V_{OC} increases provided that a realistic value of Schottky barrier is used. Fig. 6.11 and Fig. 6.12 demonstrate a trend, without any attempt to a unique change of the doping profile or to match the exact changes in the solar cell parameters observed experimentally.

6.3 Discussion

The explanations presented in this chapter are discussed in context with reported observations of CID and V_{OC} increase found in the literature.

Street [6.2, 6.11] mentioned that recombination of electron-hole pairs is responsible for the increase of defects during light exposure, as mentioned by Stutzmann [6.3] and therefore, the same defect creation process should be expected during current injection of a-Si:H p-i-n devices. He mentions that LID and CID exhibit a sublinear time dependence and saturation of defects in the long term. Details on the structure of the devices used are not clear and the material used as a contact is not mentioned in his publication. Similar conclusions had already been found by Nakamura [6.12].

Dasgupta [6.4] proposed an accelerated degradation technique that combines current injection and light exposure. According to his study, CID reduces the parameters of the solar cells at a faster rate than LID and stabilizes them at a lower value than conventional LID, regardless of the value of current injected. The excess of degradation can then be recovered by exposing the cell to light. A combination of current injection followed by light exposure would be helpful to find the stabilized solar cell parameters under standard test conditions without performing a long term light exposure experiment. Although the results of CID explained in this chapter show CID to be an effective and fast degradation technique, they differ in that, 1) Dasgupta did not observe an increase of the initial V_{OC} and, 2) J_{SC} was heavily reduced even for CID in his experiment. Also, the light induced recovery mentioned by Dasgupta was never observed for the solar cells degraded with current in this work even after annealing. The values observed after 100 hours in Fig. 6.1 were practically not recovered. This suggests that the degradation observed here is permanent.

Caputo [6.5] also observed a decrease on J_{SC} during CID and added the possibility of an increase of defects at the p-i interface and the central region of the absorber layer. Similarly, Dutta [6.6] simulated the evolution of defects during the current injection process and mentions that the initial stages of CID are responsible for an increase of defects at the p-i interface and to a lesser extent at the i-n interface. Dutta also observed an increase of V_{OC} during the first hour of CID which is followed by a further reduction and explains that there is migration of defects from the interfaces to the bulk of the intrinsic layer as the current is applied. No specific reason was given to explain the initial increase of V_{OC}. The rest of the

solar cell parameters however, follow the same trend than previous CID, where J_{SC} is observed to reduce.

An enhancement of V_{OC} for solar cells has also been observed during LID, and although a reason for the increase is not yet clear, it is often related to p-doped layers. Aker and Fritzsche attributed this effect to hole accumulation at an oxide surface layer [6.13]. On the other hand, Jang reported the V_{OC} increase as a consequence of the dopant activation of boron with light soaking [6.14]. The same conclusion was later expanded by Isomura [6.15]. These two explanations are compatible with the results presented here for the CID case, since the V_{OC} increase occurs in presence of an oxide layer, which is the ZnO contact. The activation of dopants at the p-layer is represented as a redistribution of the doping profile of the p-layer, which causes an increase of holes near the p-i interface. Similarly, Johnson reported via device modelling that a redistribution in energy of states at the p-i interface allows a greater band bending across the entire solar cell that enhances the V_{OC} [6.16].

Masini [6.17] used a n-i-p-i-n structure to monitor the current degradation of boron-doped a-Si. He found an increase of measured voltage across the device at different intervals during constant current injection. This represents an increase of R_S on his structure, which agrees with the changes observed here.

Recently, Stuckelberger concluded that an increase of dangling bond density at the p-layer and i-layer cause an increase and reduction of V_{OC} respectively, and that there is a competition between both mechanisms during the degradation interval. This can explain the often observed increase of V_{OC} followed by a decrease of V_{OC} [6.18]. Although an increase of defects in the p-layer did not succeed to explain the results presented here, it is understood that an increase of defects near the ZnO/a-Si:H(p) interface can reduce the tunnelling transport between the layers, and hence affect the *FF* of the cell. Whereas, a reduction of tunnelling transport at the interface is here explained with a reduction in the hole concentration caused by excessive electron injection during CID, and by a reduction of *n*.

A V_{OC} enhancement has also been observed for entire µc-Si:H solar cells, although it has been investigated with less depth. Lord attributed this effect to a decrease in the microcrystalline volume fraction during light soaking [6.19]. As a consequence, there is an increase of the amorphous region, which has a broader bandgap. The same conclusions were obtained by Yang for heterogeneous solar cells with different degrees of crystallinity [6.20]. His observation was consistent for LID and CID, but related to the same principles of Staebler-Wronski effect. However, Lord and Yang model are still compatible with the results presented in this chapter, since a reduction of the microcrystalline size of the µc-Si:H(p) layer or in other words, the material becoming more amorphous, would cause an increase of the semiconductor bandgap that increases the built-in potential of the cell. At the same time this would cause an increase of Φ_{bp} and the observed decrease of *FF*, indicating a trade-off between both properties.

Finally, Deng and Wronski measured the ideality factor of the main junction as a function of the applied voltage [6.21]. They found that the value of *m* at medium bias regime moves towards higher values with light exposure, whereas controlled degradation of the cell outside the bulk of the intrinsic layer, such as at the p/i interface, does not affect the value of *m*. This agrees with the results presented here, where an increase of *m* is only observed along a reduction of J_{SC}, which is the result of increased recombination at the absorbing layer.

6.4 Summary of Chapter 6

Chapter 6 completes the experimental part of this thesis with a stability study of the solar cells. The parameters V_{OC}, J_{SC}, P_{MAX}, and *FF* were used to evaluate the performance of the solar cell as a function of light exposure and current injection for a period of up to 100 hours, whereas the full circuit parameters *m*, I_O, *n* and Φ were used to identify the element of degradation. As expected, it was found that light exposure increases the quantity of defects of the a-Si:H(i) layer, where most of the light is absorbed. This assumption is supported by the reduction of J_{SC}, which was evident for all the cells regardless of the p-type layer used. On the other hand, current injection produced different results which were more evident in the fully a-Si:H cells. An excessive decrease of *FF* with a minimal decrease in J_{SC} was

observed for the cell with a-Si:H(p), whereas the reduction of *FF* was not obvious for the cell with µc-Si:H(p). The study of the ideality factors *m* and *n* for the light induced degradation and current induced degradation of the completely amorphous cell indicated an increase of *m* as a result of the Staebler-Wronski effect after light exposure, whereas a decrease of *n* points to damage of the ZnO/a-Si:H(p) interface during current injection. This represents a reduction in the tunnelling transport occurs, which heavily impacts *FF* as a consequence.

6.5 References in Chapter 6

[6.1] D. L. Staebler and C. R. Wronski, "Reversible conductivity changes in discharge-produced amorphous Si," *Appl. Phys. Lett.*, vol. 31, no. 4, p. 292, 1977.

[6.2] R. A. Street, "Current-induced defect creation and recovery in hydrogenated amorphous silicon," *Appl. Phys. Lett.*, vol. 59, no. 9, p. 1084, 1991.

[6.3] M. Stutzmann, W. B. Jackson, and C. C. Tsai, "Light-induced metastable defects in hydrogenated amorphous silicon: A systematic study," *Physical Review B*, vol. 32, no. 1, 1985.

[6.4] A. Dasgupta, N. Palit, and S. Ray, "Accelerated degradation in amorphous silicon solar cells by a combination of current injection and light insolation," *Sol. Energy Mater*, vol. 55, pp. 395–402, 1998.

[6.5] D. Caputo, "Degradation and annealing of amorphous silicon solar cells by current injection experiment and modeling," *Sol. Energy Mater.*, vol. 59, pp. 289–298, 1999.

[6.6] U. Dutta, P. Chatterjee, S. Tchakarov, M. Uszpolewicz, and P. Roca i Cabarrocas, "Metastable defect migration under high carrier injection in hydrogenated amorphous silicon p-i-n solar cells," *J. Appl. Phys.*, vol. 98, no. 4, p. 044511, 2005.

[6.7] M. Stuckelberger, Y. Riesen, M. Despeisse, J.-W. Schüttauf, F.-J. Haug, and C. Ballif, "Light-induced Voc increase and decrease in high-efficiency amorphous silicon solar cells," *J. Appl. Phys.*, vol. 116, no. 9, p. 094503, Sep. 2014.

[6.8] C. R. Wronski and X. Niu, "The Limited Relevance of SWE Dangling Bonds to Degradation in High-Quality a-Si : H Solar Cells," *IEEE Journal of Photovoltaics*, vol. 4, no. 3, pp. 778–784, 2014.

[6.9] A. N. Corpus-Mendoza, M. M. De Souza, and F. Hamelmann, "Transport mechanisms and effective Schottky barrier height of ZnO/a-Si:H and ZnO/μc-Si:H heterojunction solar cells," *Journal of Applied Physics*, vol. 114, pp. 184505, 2013.

[6.10] A. N. Corpus-Mendoza, M. M. De Souza, and F. U. Hamelmann, "Design of Schottky Contacts for Optimum Performance of Thin-Film Silicon Solar Cells," *IEEE Journal of Photovoltaics*, vol. 5, no. 1, pp. 22–27, 2015.

[6.11] R. A. Street, and M. Hack, "Saturation and recovery kinetics of current-induced defects in a-Si:H," *Journal of Non-Crystalline Solids*, vol. 137 and 138, pp. 263-264, 1991.

[6.12] N. Nakamura, K. Watanabe, M. Nishikumi, and Y. Hishikawa, "Influence of excess earriers on the Staebler and Wronski effect of a-Si solar cells," *Journal of Non-Crystalline Solids*, 59 & 60, pp. 1139–1142, 1983.

[6.13] B. Aker, and H. Fritzsche, "Photoinduced metastable surface effects in boron-doped hydrogenated amorphous silicon films," *Journal of Applied Physics*, vol. 54, no. 11 pp. 6628, 1983.

[6.14] J. Jang, T. M. Kim, J. K. Hyun, J. H. Yoon, and C. Lee, "Temperature dependent light induced changes and annealing of the changes in hydrogen amorphous silicon," Journal of Non-Crystalline Solids, vol. 59 and 60, pp. 429-432, 1983.

[6.15] M. Isomura, "What causes the inverse Staebler-Wronski effect in p-type a-Si:H?," *J. Non. Cryst. Solids*, vol. 198–200, pp. 453–457, 1996.

[6.16] E. V. Johnson, F. Dadouche, M. E. Gueunier-Farret, J. P. Kleider, and P. R. I. Cabarrocas, "Open-circuit voltage increase dynamics in high and low deposition rate polymorphous silicon solar cells," *Phys. Status Solidi*, vol. 207, no. 3, pp. 691–694, 2010.

[6.17] G. Masini, G. De Cesare, and F. Palma, "Current induced degradation in boron-doped hydrogenated amorphous silicon: A novel investigation technique," *J. Appl. Phys.*, vol. 77, no. 3, p. 1133, 1995.

[6.18] M. Stuckelberger, Y. Riesen, M. Despeisse, J.-W. Schüttauf, F.-J. Haug, and C. Ballif, "Light-induced Voc increase and decrease in high-efficiency amorphous silicon solar cells," *J. Appl. Phys.*, vol. 116, no. 9, p. 094503, Sep. 2014.

[6.19] K. Lord, B. Yan, J. Yang, and S. Guha, "Light-induced increase in the open-circuit voltage of thin-film heterogeneous silicon solar cells," *Appl. Phys. Lett.*, vol. 79, no. 23, pp. 3800–3802, 2001.

[6.20] J. Yang, K. Lord, B. Y. B. Yan, a. Baneijee, and S. Guha, "Correlation of the open-circuit voltage enhancement of heterogeneous silicon solar cells and the Staebler-Wronski effect," Conf. Rec. Twenty-Ninth IEEE Photovolt. Spec. Conf. 2002., no. 0, pp. 1094–1097, 2002.

[6.21] J. Deng and C. R. Wronski, "Carrier recombination and differential diode quality factors in the dark forward bias current-voltage characteristics of a-Si:H solar cells," *J. Appl. Phys.*, vol. 98, no. 2, p. 024509, 2005.

CHAPTER 7.

CONCLUSIONS

This final part of the thesis presents the conclusions and the major results achieved during the time of research. Possible ideas to extend and apply the knowledge developed here are suggested.

This thesis describes the role of the p-layer on the performance and stability of thin film silicon solar cells. It is shown that a complete understanding of the current-voltage characteristics of a-Si:H solar cells can only be achieved when a realistic and non-ideal Schottky contact is considered. It is by the use of equivalent electronic circuits and TCAD modelling that the detrimental effects of non-ideal contacts are identified therefore, the models presented here are a helpful feedback tool for further optimization of solar cells.

7.1 Main achievements

7.1.1 Electrical characterization of solar cells

A simple methodology for the modelling of solar cell parameters is applied. The technique successfully demonstrates how to evaluate R_S from an individual *J-V* curve measured in dark conditions. The value obtained can be used to correct the effects of R_S in the *J-V* curves at different levels of illumination. The advantages of this methodology are:

1) The evaluation of R_S from a single *J-V* curve, which reduces the complexity of illumination systems with an adjustable intensity of light or even avoids the need of a lamp.

2) The distinction between parasitic resistive effects and recombination in the main junction. This allows to evaluate the quality of the main diode, which is the most essential element of a solar cell. As a consequence, it is possible to extract the solar cell parameters with more accuracy and precision.

The conventional model of the solar cell is also expanded to account for non-ideal contacts with the inclusion of the Schottky diode that represents the TCO/p-layer interface in thin film silicon solar cells. The expanded model can be used as a valuable feedback tool for the design of contacts for solar cells.

7.1.2 ZnO/a-Si:H(p) and ZnO/μc-Si:H(p) heterojunction structures

The value of the Schottky barrier height for ZnO/a-Si:H(p) and ZnO/μc-Si:H(p) diode structures is extracted from *J-V-T* measurements and TCAD simulations. It is observed that the *J-V* curves of these heterojunctions show an asymmetrical behaviour, which demonstrates the rectifying properties of the heterojunctions. However, the extraction of ideality factors $n>1$ indicates a deviation from thermionic emission over the barrier, and reveal a contribution of tunnelling transport through the barrier. It is also observed that the *J-V* curves for both types of heterojunctions evolve from a rectifying behaviour to an Ohmic behaviour as the doping concentration of the p-layer is increased. The evaluation of the Schottky barrier height from *J-V* measurements becomes more difficult with an increase of doping therefore, the barrier height for the highly doped samples is only extracted from TCAD simulations.

Finally, the greater conductivity and lower Schottky barrier height of the ZnO/μc-Si:H(p) structure in comparison to the ZnO/a-Si:H(p) diode demonstrate that μc-Si:H(p) is more suitable as a p-layer in contact with ZnO in terms of electrical properties.

7.1.3 Electronic circuit and TCAD models of thin film silicon solar cells

The ZnO/a-Si:H(p) and ZnO/μc-Si:H(p) structures are used as window layers for ZnO/p-layer/a-Si:H(i)/a-Si:H(n)/ZnO/Ag solar cells. The solar cells are modelled via TCAD simulations and with the improved equivalent electronic circuit that accounts the effects of non-ideal contacts. The advantages of this equivalent circuit are:

1) The independent evaluation of the main junction of the solar cell, and the detrimental effects of Schottky contacts. The quality of both junctions is analysed by extracting the ideality factors *m* and *n* for the main junction and Schottky contact respectively.

2) The inclusion of the ideality factor *n* allows to identify the impact of tunnelling transport in the performance of the solar cell. This is a contribution to previous equivalent circuits of solar cells that successfully identify the existence of Schottky

contacts but assume thermionic emission as the only transport mechanism at the contact interface.

The model developed here is not limited to the use of thin film silicon solar cells, since it can be applied to characterize any solar cell technology where the contact is not completely Ohmic for example, heterojunction solar cells or CdTe solar cells.

7.1.4 Stability of thin film silicon solar cells

The use of current injection and light exposure is shown to distinguish the impact of degradation in the contact, and intrinsic regions of a-Si:H solar cells respectively. The drop in the maximum power conversion capability of the cell after light exposure is a consequence of an increase of dangling bonds in the intrinsic layer of the cell due to the Staebler-Wronksi effect. On the other hand, injected current increases the open circuit voltage and greatly reduces the fill factor without affecting the short circuit current, which is attributed to an increase of defects in the p-layer. The equivalent circuit model that incorporates a separate diode for the Schottky contact effectively addresses the separation of damage in the two regions via the respective ideality factors. The results are also replicated with TCAD simulations, showing for the first time, the effect of the Schottky barrier height on the degradation of the solar cell and improvement of V_{OC}.

7.2 Future work

The content of this thesis can be furtherly improved on the theoretical side by the developing of equations or sharpening of computer modelling that can quantify the energy levels or layer depth of the regions that are affected in terms of performance and stability. This would help the fabricators of thin film solar cells to reduce or even cancel the detrimental effects of light exposure. Some of the possible actions to be taken include:

7.2.1 Characterization of solar cell

A parameter of significant importance through this thesis is the value of Schottky barrier height. This value is experimentally extracted from *J-V* measurements of heterojunction structures, and then evaluated with TCAD simulations. This complicated process could be improved by extracting the value of the Schottky barrier height directly from *J-V* measurements of solar cells. This is a technical challenge, since the *J-V* curves are affected by multiple parameters whose effects can be difficult to distinguish.

7.2.2 Evolution of defects on TCAD model

The evolution of doping profile identified by means of computer simulations as a result of the excessive electron injection can be correlated to an evolution of energy defects instead. This model could be related to the decrease of *FF* and increase of V_{OC} observed during current injection. Detection of the exact evolution of defects would provide solar cell fabricators with more robust deposition techniques in order to improve the stability of cells.

7.2.3 Contact degradation vs intrinsic region degradation

Although it is demonstrated here that current injection has detrimental effects on the contact properties, and light exposure mainly damages the intrinsic region, the existence of both types of degradation should exist for both degradation techniques. It is important to identify up to what point the contact is damaged during light exposure, especially since the decrease of *FF* accompanied by an increase of V_{OC} has been observed by other groups during light degradation tests.

7.2.4 Extension to different degradation techniqes

In this thesis, current injection and light exposure are used to identify the impact that contact, and intrinsic region degradation have on the *J-V* curve. In the practical case, this makes possible to identify the damaged region by analysing the *J-V* curve. In a similar way, different degradation techniques could be developed under controlled conditions to separate the effects of different parameters such as temperature, humidity or controlled physical

damage on the stability of the solar cell. This would result in a collection of optimization techniques depending on the application where a solar cell is required.

7.3 Future perspectives for thin film silicon solar cells

Thin film silicon solar cells offer multiple advantages over other solar cell technologies, for example, the abundance of non-toxic raw materials for their fabrication, the use of rigid or flexible substrates for their deposition which allows thin film silicon solar cells to be adapted to the requirements of different products (from calculators to large area solar panels), low cost of fabrication, and suitability for building integration. However, despite these advantages, thin film silicon has a share of less than 10% in a market dominated by crystalline silicon. This is due to the lower stabilized efficiencies of thin film silicon solar panels (7-10%) in comparison to crystalline silicon (15-20%), which complicates the future use of thin film silicon as a material for large scale electricity production from solar.

Some strategies to improve the efficiency of thin film silicon solar cells are the development of thinner absorption layers and the investigation of material properties in order to reduce the LID in a-Si:H. This represents the major issue for this technology, and its solution would allow the fabrication of single junction a-Si:H solar cells with a stable efficiency of approximately 13%. Another option is the fabrication of multi-junction devices which is possible with the use of a-Si:H alloys. This allows to adjust the bandgap of multiple absorption layers in a PV device in the range of 0.6-2.2 eV. This concept is demonstrated in double and triple junction devices with stabilized efficiencies over 12% and 13% respectively, whereas initial efficiencies over 16% have been reported for triple junction.

Another issue with a-Si:H solar cells is the existence of a Schottky barrier at the ZnO/a-Si:H(p) interface which affects the performance of the cell. This thesis focuses to the study of this interface. It is found that the conventional equivalent circuit of a solar cell must be modified to include the effects of non-Ohmic contacts when the Schottky barrier height between the contact and doped layer exceeds 0.5 eV in order to achieve an accurate modelling. This contribution is important since it can help to optimize contacts of solar cells

where Schottky barriers have been reported such as a-Si:H, CdTe, and dye sensitized solar cells.

Further development of a-Si:H in terms of stability and contact fabrication can benefit one of the most promising PV technologies nowadays which is, the HIT solar cell. This cell uses the structure TCO/a-Si:H(p)/a-Si:H(i)/c-Si(n)/a-Si:H(i)/a-Si:H(n)/TCO where c-Si acts as the absorber layer in order to reduce LID, a-Si:H(i) is used to passivate dangling bonds at the edges of c-Si, a-Si:H(p) and a-Si:H(n) act as the doped layers, and a TCO is used as a contact. Therefore, despite the current drawbacks of a-Si:H in PV devices, the use of it will continue to be of significant impact in the fabrication of high efficiency devices for large-scale electricity production. Also, a-Si:H solar cells are currently of great interest for indoor energy harvesting in wireless sensors.

Appendix

This section shows the effect of different values of the parameters simulated in chapter 5 on the J-V curve of the solar cell. All of the curves shown here are simulated by scanning a range of values for a particular parameter while the rest of the parameters are kept constant and equal to the values shown in Table 2. The simulations performed here are mainly related to the p-layer, since it is the topic of interest of this thesis. Some limitations of the model are also mentioned.

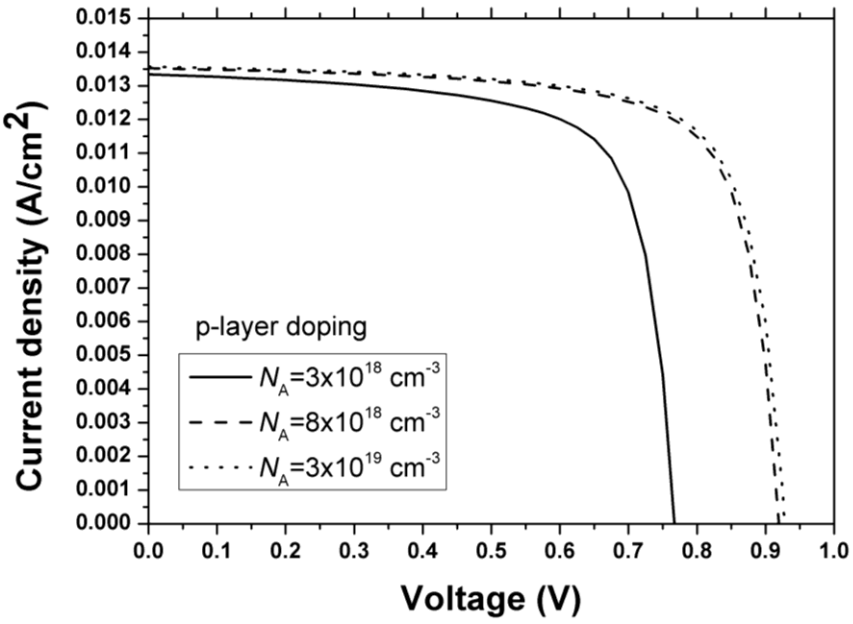

Figure A.1. V_{OC} of the solar cell increases as N_A increases. The model reproduces the electrical properties of the cell as a function of doping however, it is limited in its ability to reproduce the optical properties of the p-layer as a function of doping, since an excess of doping can increase the absorption of light in the p-layer, which decreases the absorption in the intrinsic region.

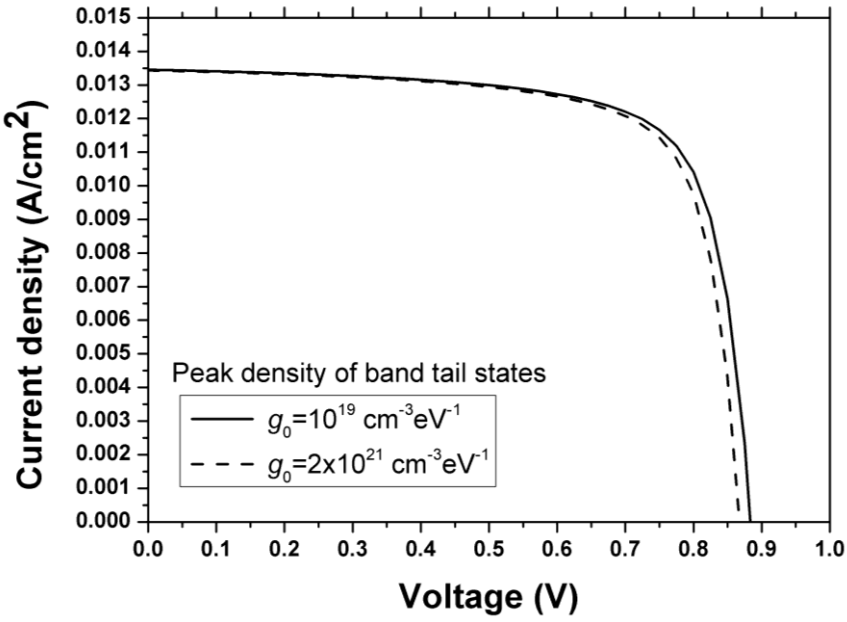

Figure A.2. Influence of density of band tail states. The model shows a low sensitivity to the density of band tail states. Detrimental effects are observed only when g_0>10^{19} $cm^{-3}eV^{-1}$. The value of g_0 >$2x10^{21}$ $cm^{-3}eV^{-1}$ used in this simulation is considered standard for a-Si:H.

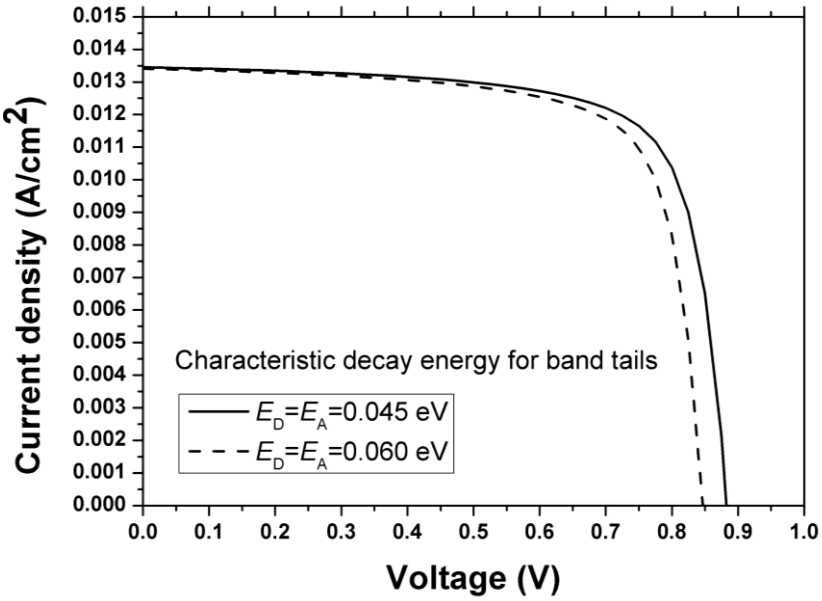

Figure A.3. Influence of the characteristic decay energies E_D and E_A. Tail states deeper in the bandgap increase as E_D and E_A increase, which has detrimental effects on the *J-V* curve. No effect was observed for values lower than 0.045 eV, whereas values higher than 0.060 eV are above the standard simulated commonly.

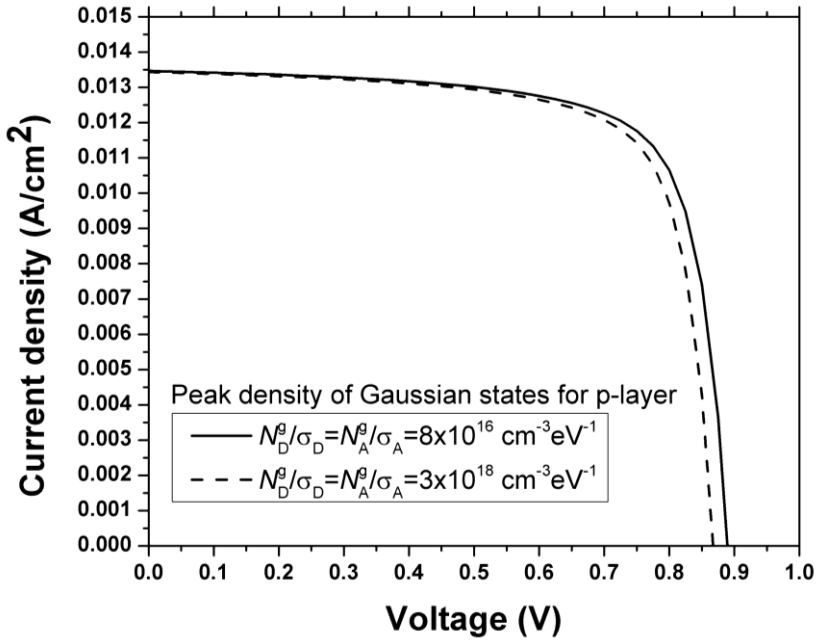

Figure A.4. Influence of the peak density of Gaussian states of the p-layer on the *J-V* curve. The majority of carriers introduced by dopants occupy Gaussian states. This explains the higher values of $N_D^g/\sigma_D=N_A^g/\sigma_A$ in the doped layers than in the intrinsic region.

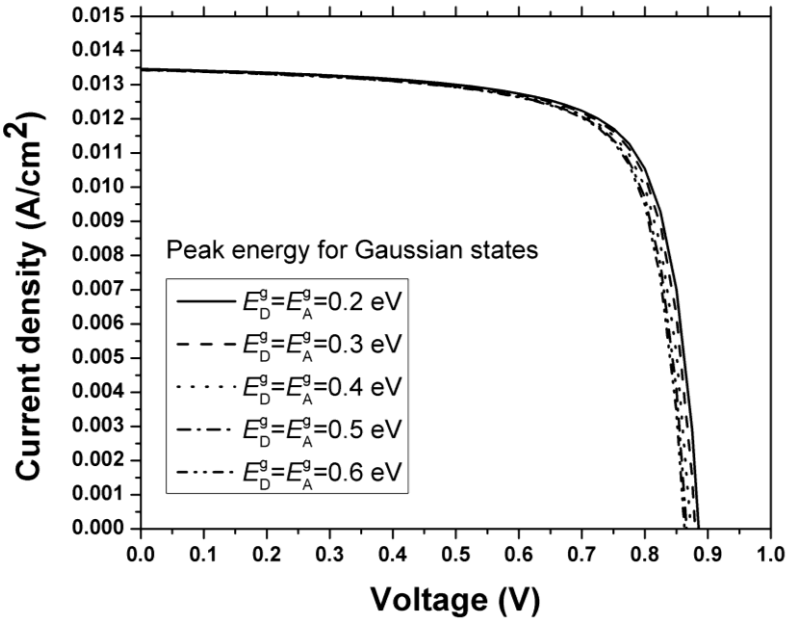

Figure A.5. Influence of the peak energy for Gaussian states in the p-layer. In a similar way to the band tail states, the increase of Gaussian states closer to the middle of the gap show detrimental effects of the *J-V* curve.

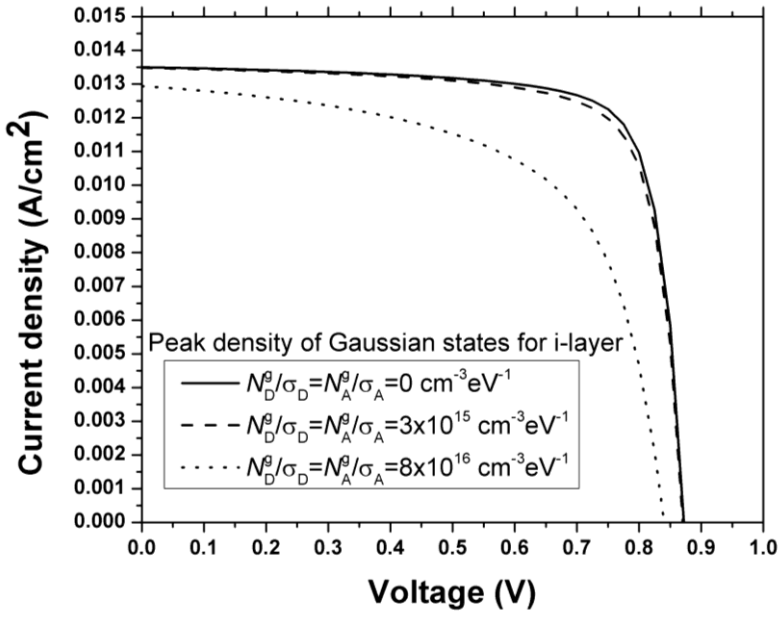

Figure A.6. Influence of peak density of Gaussian states in the intrinsic layer. The model is more sensitive to Gaussian states in the i-layer than in the p-layer. The increase of N_D^g/σ_D and N_A^g/σ_A in the intrinsic layers has detrimental effects in all the parameters of the solar cell, including J_{SC} and V_{OC}. These effects are observed during LID.

Publications and conferences that have arisen

A. N. Corpus-Mendoza, M. M. De Souza, and F. Hamelmann, "Transport mechanisms and effective Schottky barrier height of ZnO/a-Si:H and ZnO/μc-Si:H heterojunction solar cells," *Journal of Applied Physics*, vol. 114, pp. 184505, 2013.

A. N. Corpus-Mendoza, M. M. De Souza, and F. U. Hamelmann, "Design of Schottky contacts for optimum performance of thin-film silicon solar cells," IEEE Journal of Photovoltaics, vol. 5, no. 1, pp. 22–27, 2015.

P. B. Pillai, A. N. Corpus Mendoza, M. M. De Souza, G. Bree, and D. Jeng, "Extraction of Schottky barrier at the F-doped SnO_2/TiO_2 interface in dye sensitized solar cells," *J. Renew. Sustain. Energy*, vol. 6, no. 1, pp. 013142, 2014.

A. N. Corpus-Mendoza, M. M. De Souza, and F. U. Hamelmann, "Separation of bulk and contact interface degradation in thin film silicon solar cells," *J. Renew. Sustain. Energy* vol. 7, pp. 063115, (2015)

A. N. Corpus-Mendoza, and M. M. De Souza, "The Physics and modelling of a Schottky barrier contact in thin film solar cells," *Journal of Energy Challenges and Mechanics*, 2016. (Accepted and waiting for publication details)

A. N. Corpus-Mendoza, M. M. De Souza, and F. U. Hamelmann, "Extraction of the Schottky barrier height in the presence of bias dependent ideality factors in ZnO/μc-Si:H heterojunctions for solar cells," Talk at the *4th International Symposium on Transparent Conductive Materials*, Crete, Greece, 2012.

A. N. Corpus-Mendoza, M. M. De Souza, and F. U. Hamelmann, "The Physics and modelling of a Schottky barrier contact in thin film solar cells," Talk at the *4th International Symposium on Energy Challenges and Mechanics – working on small scales*, Aberdeen, Scotland, 2015.